Effect of the microstructure of nickel alloy 718 Oil Patch on its corrosion behavior

TECHNISCHE UNIVERSITÄT DARMSTADT

Vom Fachbereich Maschinenbau
der Technischen Universität Darmstadt

Zur Erlangung des Grades
Doctor Ingenieur
(Dr.-Ing.)

Dissertation
von Olesya Gosheva

Erstgutachter:	Prof. Dr.-Ing. Matthias Oechsner
Zweitgutachter:	Prof. Dr.-Ing. Clemens Müller
Tag der Einreichung:	10.04.2018
Tag der mündlichen Prüfung:	26.06.2018

Darmstadt 2018

Acknowledgement

Firstly, I would like to express my sincere gratitude to the company VDM Metals, which made this project possible by granting the research work and providing the material for the experiments.

I would also like to thank the head of the Institute for Materials and Technology at Technische Universität Darmstadt, Prof. Matthias Oechsner who provided me the opportunity to join his institute as research associate, and gave me the access to the laboratory and research facilities. Without his insightful comments and encouragement it would not have been possible to conduct this research.

My sincere thanks also goes to my advisor Dr. Georg Andersohn for providing me with the freedom in my scientific work as well as for his helpful comments on the manuscript.

I thank my colleagues and students for the stimulating discussions and for all the fun we have had in the last 6 years. In particular, I am grateful to Dr. Christian Krauß, Mr. Tom Engler, Mr. Marius Siebers, Dr. Udo Depner, Mrs. Jennifer Honselmann, and Mrs. Caroline Yancey. Also I thank Mr. Sven Kania for his precious technical support.

A part of the results presented in this work were obtained in the laboratories of Dr. Sarmiento-Klapper (Baker Hughes Incorporated) and Dr. Berger (Max Planck Institute for Polymer Research). Dr. Sarmiento-Klapper conducted a series of a long-time Open-Circuit-Potential measurements, which are described in the chapter 6.2. He also made a significant contribution to the data interpretation. Dr. Berger performed the Scanning Kelvin Probe Force Microscopy measurements on the intermetallic inclusions and their evaluation.

Last, but not least, I would like to thank my family: my parents, my brother and my dear husband for their continued support and encouragement especially throughout the writing of this work.

Erklärung:

Hiermit erkläre ich, dass ich die vorliegende Dissertation selbständig verfasst und nur die angegebenen Hilfen verwendet habe.

Darmstadt, 24. April 2018

Table of contents

Index of abbreviations

Abbreviation	Unity	Description
%		Percent
°C / K		The unit of temperature 1°C=274,15 K
m		Meter, the unit of length
A		Ampere, the unit of electrical current
V		Volt, the unit of electric potential
J		Joule, the unit of energy
Pa		Pascal, the unit of mechanical tension or pressure
rad		Radian, the unit of angle
s		Second, the unit of time
a		Exponent of Constant Phase Element (CPE)
A	cm^2	Surface area
a	nm	Lattice constant, or lattice parameter – physical dimension of unit cells in a crystal lattice
b	nm	Burgers vector
C	mol/cm^3	Hydrogen concentration
d	nm	Length of the phase precipitation
F		Faraday constant (96485,3399 $C \cdot mol^{-1}$)
I	mA	Electrical current
I_C	mA	Cathodic partial current
i	mA/cm^2	Current density
i_0	mA/cm^2	Exchange current density
i_A	mA/cm^2	Anodic partial current density
i_c	mA/cm^2	Corrosion current density
$i_{c,h}$	mA/cm^2	Free corrosion current density
$i_{c,p}$	mA/cm^2	Corrosion current density of an intact passive film
i_∞	mA/cm^2	Maximum stationary permeation current density
j	$1/cm^2 \cdot s$	Hydrogen flux
k		Boltzmann constant ($1{,}38064852 \cdot 10^{-23}$ $m^2 \cdot kg \cdot s^{-2} \cdot K^{-1}$)
L	m	Middle slip length
N		Number of dislocations within one slip band

E_{OCP}	mV	Open circuit potential
E_p	J	Activation energy for hydrogen diffusion
E_{pit}	mV	Pitting potential
G	GPa	Shear modulus
R		Universal gas constant (8,3144621 J·(mol·K)$^{-1}$)
r	m	Middle radius of shearable particle $\gamma' + \gamma''$
t	s	Time
T	K	Temperature
ΔU_A	mV	Anodic excess voltage
V		Volume fraction of shearable particle $\gamma' + \gamma''$
V_{CPD}	V	Contact potential difference
R_P	Ω·cm²	Polarization resistance
ω	rad/s	Angular frequency
x	m	Space coordinate
z		Number of the exchanged charge carriers
$Z(\omega)$	Ohm	Impedance
α		Factor of inhibited charge transfer
γ	J	APB energy
γ'		Strengthening precipitation phase, gamma prime
γ''		Strengthening precipitation phase, gamma double prime
δ		Precipitation phase, delta
θ		Phase angle
ν		Poisson ratio
ρ	g/cm³	Density
ϕ_{sample}	J	Work function of a sample
ϕ_{tip}	J	Work function of the measurement tip
$\Phi(V)$	V	Electric field strength of the passive film
AFM		Atomic force microscope
AE		Accoustic Emission
ASTM		American Society for Testing and Materials – an international standards organisation
APB		Antiphase Boundary
API		American Petrolium Insitute

bcc	Body centered cubic type of crystal unit cell structure
BSE	Backstatter electron
CE	Counter electrode
CPD	Contact potential difference
DIN	Deutsches Institut für Norm
DSB	Dislocation slip bands
EAC	Environmentally assisted cracking
EDX	Energy Dispersive X-ray Analysis
EIS	Electrochemical Impedance Spectroscopy
EN	European norm
fcc	Face centered cubic type of crystal unit cell structure
ISO	International Organization for Standartization
HE	Hydrogen Embrittlement
HEDE	Hydrogen enhanced decohesion
HELP	Hydrogen enhanced localized plasticity
hcp	Hexagonal close packed unit cell structure
HRC	Rockwell Hardness measured on the C scale
NACE	National Association of Corrosion Engineers – organization of corrosion engineers in United States of America
OCP	Open circuit potential
PWR	Pressurized water reactor
SFE	Stacking fault energy
SKPFM	Scanning Kelvin probe force microscopy
PH	Precipitation hardened
SCC	Stress Corrosion Cracking
SCE	Standard calomel electrode
SEM	Scanning electron microscope
SSC	Sulfide Stress Cracking
SSR	Slow strain rate
RE	Reference electrode
TB	Twin boundaries
TEM	Transmission electron microscope
VAR	Vacuum arc remelting

V2A		Chemical etchant for the metallographic preparation of materials with austenitic microstructure
WE		Working electrode
XRD		X-ray diffraction
H	GPa	Hardness
pH		Decimal logarithm of the reciprocal of the hydrogen ion activity in a solution

Introduction, problem statement and work objectives

1.1 Introduction

In the light of continuously growing energy demand oil and natural gas is estimated to become the primary target fuels for energy generation, [1]. However since the remaining accessible resources are primarily located in deep wells and particularly those in deep-water, oil and gas extraction is going to become increasingly demanding in the coming years, [2]. Compared to shallow wells with approximate depth of 1500 m, deep wells are highly corrosive and contain highly aggressive gases such as hydrogen sulfide and carbon dioxide, as well as halide ions like chlorides and bromides or sometimes even elemental sulphur, [3]. In addition, different levels of corrosive conditions are compounded by temperatures up to 260 °C and pressures up to 170 MPa, [2]. Taking into account the hardly predictable complex mechanical stress conditions, comprised of torque, tension, compression and bending stresses, the potential for catastrophic failures in deep well due to the stress corrosion cracking (SCC) or sulfide stress cracking (SSC) is a serious concern, [2], [4], [5]. According to the failure cases reports, a drill string failure happens, on average, one out of every seven drilling operations, causing more than $100,000 of additional expenses per failure event, [6].

The National Association of Corrosion Engineers (NACE)-specification MR 0175 [7] provides with assistance for the appropriate material selection for a particular set of well conditions according to the following criteria, [2]:

- Mechanical properties,
- General corrosion resistance,
- Pitting and crevice corrosion resistance,
- Chloride stress corrosion cracking resistance,
- Sulfide stress corrosion cracking resistance.

A final material choice for a specific application is usually made in agreement with this standard under consideration of the material price and availability.

Unlike the other corrosion resistant alloys used for the deep-sea wells in the oil and gas industry, the precipitation-hardened (PH) alloy 718 is one of the worldwide most largely produced material, available in a wide range of diameters, [3]. This material combines the good weldability with excellent mechanical and corrosion-resistance properties over a broad range of temperatures, [8]. In addition, its low magnetic permeability enables the application of alloy 718 in measurement-while-drilling applications, where the magnetic

surveying is used for the well orientation measurements, [9].

Large body of the experimental research in the last two decades revealed an undoubtable correlation between the corrosion and embrittlement characteristics of nickel-base alloys and their microstructure, [9], [10], [11], [12]. Therefore, a careful choice of the chemical composition and the suitable heat treatment procedure would result in a significant improvement of the overall material performance.

1.2 Problem statement

Due to the strong correlation between the physical metallurgy of the alloy 718 and its overall performance, the major effort in the material development of the last few decades was undertaken to define the parameter window concerning chemical composition and heat treatment procedures to achieve the optimal material properties under oil and gas applications conditions, [13], [14], [15], [16]. Based on the results of comprehensive experimental research, some limitations regarding the acceptable microstructure appearance were introduced in the API standard 6ACRA, [17]. According to this specification the material microstructure shall be free from continuous grain boundary networks of secondary phase particles, which are considered as brittle. Examples of the materials with acceptable and unacceptable microstructures are given in Figure 2.

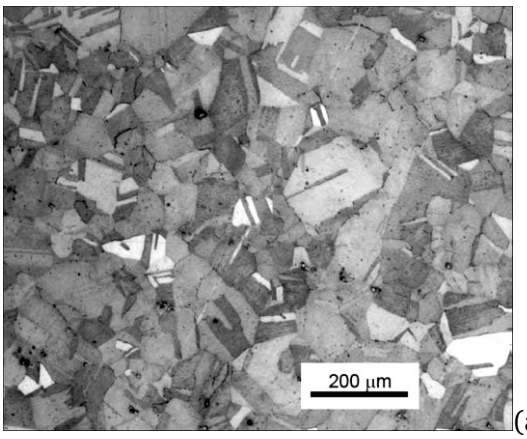

(a)
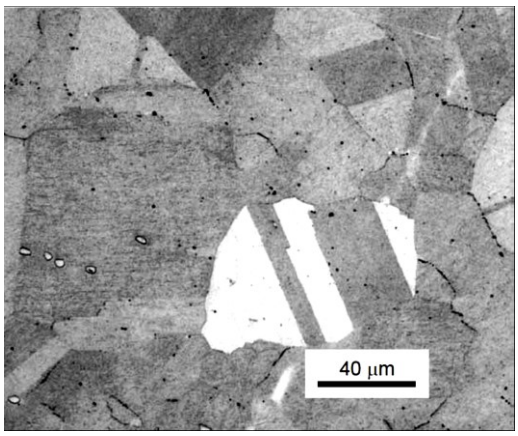

(b)

Figure 1: a), b) light optical micrographs of the acceptable microstructure of alloy 718 with isolated grain boundary delta phase with x100 and x500 magnification respectively

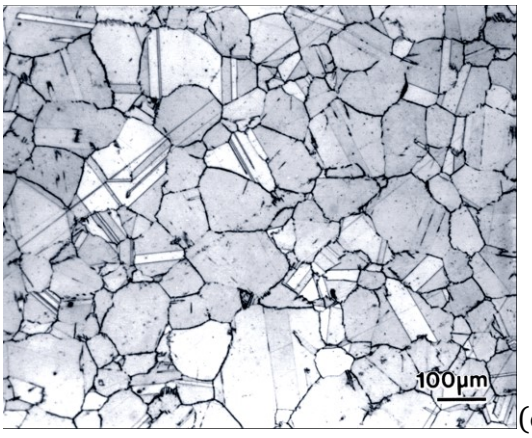

(c)
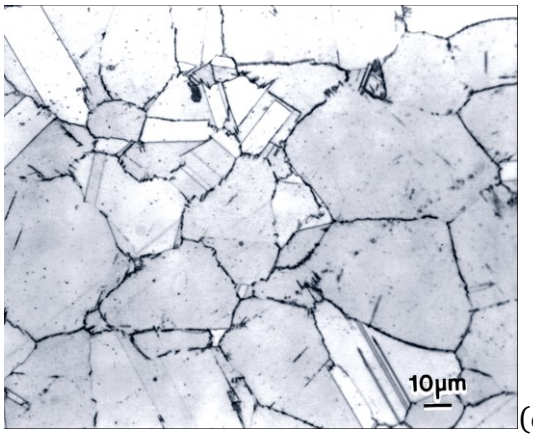

(d)

Figure 2: c), d) light optical micrographs of the unacceptable microstructure of alloy 718 due to the level of acicular delta phase on the grain boundaries with x100 and x500 magnification respectively adopted from [17]

The regulations of the manufacturing process also concerned the hardness of the material, which was considered to indicate the possible hazard potential of the material susceptibility against SCC and SSC or hydrogen embrittlement (HE). Originally, the material hardness was restricted to the maximum of 35 HRC for sour service application. However, later it was found that the same level of yield strength could be obtained at a consistent basis with a hardness of 40 HRC and the specification NACE MR0175 was updated, [9].

Although the testing procedure for the material qualification, defined in NACE MR0175 is seen as rather aggressive and conservative, some failure cases of the materials, approved according to this specification, were reported in the last decades, [3]. This and the fact mentioned above clearly indicate a gap between the current concept of the failure mechanism and the processes occurring during service.

1.3 Objectives

The primary focus of this research work is to define the interactions between the microstructural peculiarities of the material and complex collective of damage mechanisms leading to its degradation.

Due to the complexity of the alloy 718 physical metallurgy, the systematical study is narrowed to the impact of the heat treatment procedure variations on the material properties. Therefore, the influence of the chemical composition and the homogenization during the solution annealing is not taken into account.

Additionally to the characterization of the material microstructure and its alteration due to the differences in the heat treatment regimes, a closer look is given to the evaluation of

the microstructure dependent material properties regarding the resistance to localized corrosion, hydrogen embrittlement and hydrogen permeability. Collected experimental data are employed for the elaboration of a model for reliable description of service relevant damage governing processes and their interactions.

Based on the obtained findings suggestions about future improvements of the processing route are made aiming for beneficial microstructural features for the required mechanical and corrosion performance, and hence longer service life of drilling components manufactured from the alloy 718.

2 State of the art

Alloy UNS N07718 (alloy 718) is a complex nickel base precipitation hardened super alloy, which was developed in the 1960's for gas turbine engine applications, [18]. Addition of alloying elements such as aluminum, titanium, and niobium leads to the formation of strengthening secondary intermetallic phases. Due to the high chromium content, the material found its use in the corrosion challenged environments, such as oil and gas industry. Nowadays it is one of the most demanded nickel base alloys with a production share of 80%.

The material manufacture procedure is regulated by the international standard API 6ACRA (see Chapter 2.1.1), which defines the variation limits for the material chemical composition, temperature range and duration of aging treatment. Slight deviations of these parameters lead to significant differences in the material microstructure, altering the material performance. Thus, understanding of the processes governing the secondary phase precipitation and their impact on the mechanical and electrochemical behavior of the material is obligatory for the material improvement.

2.1 Microstructure of alloy 718

Nickel base alloy 718 with its face-centered cubic (fcc) matrix has an austenitic microstructure. Light microscopic micrograph in Figure 3 represents a typical morphology for this material, including twin boundaries (TB) and carbide groups, which could be observed both decorating the grain boundaries and within the grain.

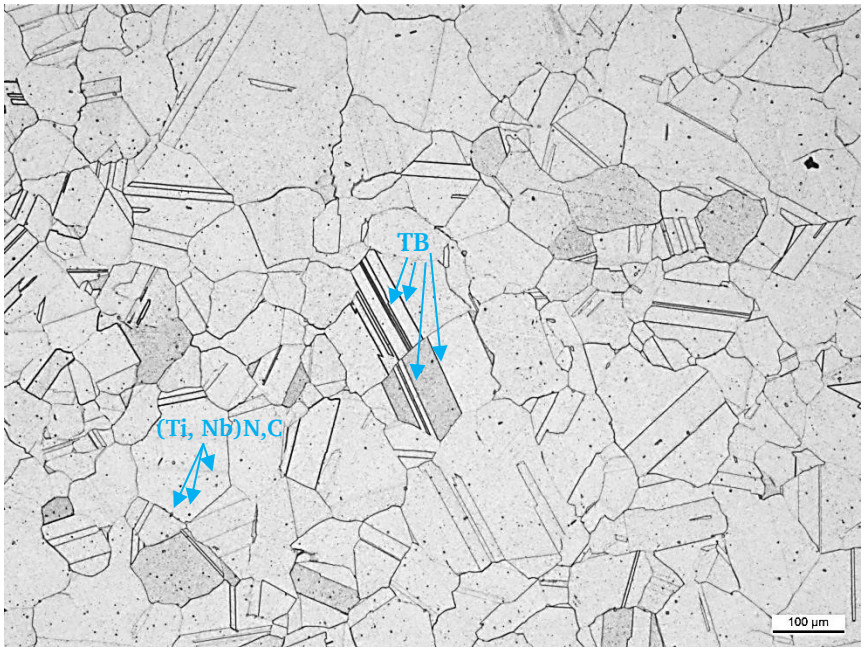

Figure 3: Light optical micrograph of the typical microstructure of alloy 718, adopted from [19]

2.1.1 Standard API 6ACRA

API Standard 6ACRA defines the minimum requirement to the material microstructure according to the existing experience in the material application, [20]. The standard demands the average grain size of ASTM 2 or finer, which should be determined in accordance with ASTM E112 [21]. The acceptance criteria include the absence of the continuous networks of secondary phases along grain boundaries or other unusual microstructural features. No laves phase and no acicular delta phase precipitations are allowed except for the individual cases, which are not representative of the bulk of the microstructure. Material production should include two-step-aging procedure, including the solution annealing and age hardening. Recommended temperature window for the solution annealing is from 1021 °C to 1052 °C for 1-2.5 hours. Prior to the aging step, the material should be cooled in air, water or oil to ambient temperature. Age hardening is performed at a material temperature of 774 to 802 °C for 6-8 hours followed by air cooling to ambient temperature. The standard also requires an implementation of several material tests, such as hardness (32 to 40 HRC are allowed), tensile testing and standard Charpy notch impact toughness measurements. The requirements for the material microstructure are limited to the conformity of the light microscope micrographs, giving an example of the accepted microstructure.

2.1.2 Intermetallic phase precipitations in nickel base alloy 718

Complex chemical composition of the alloy 718 enables the precipitation of following intermetallic phases: gamma prime (γ'), gamma double prime (γ''), delta (δ), carbonitrides M(C,N), and Laves. An overview of their structure, stoichiometry and location is given in Table 1.

Table 1: Intermetallic Nb-containing secondary phase precipitation in alloy 718 according to [22]

Phase	Structure	Stoichiometry	Location
γ'	L12	$Ni_3(Al,Ti,Nb)$	Matrix
γ''	DO22	$Ni_3(Al,Ti,Nb)$	Matrix, grain boundaries
δ	DOa	Ni_3Nb	Grain boundaries
Carbonitrides	Cubic	(Ti,Nb)(C,N)	Matrix, grain boundaries
Laves	C14	$(Fe,Cr)_2(Ti,Nb)$	Grain boundaries

The limitations of temperature for the heat treatment procedures given in API 6ACRA [20] prohibit the precipitation of the Laves phase. Therefore, they will not be taken into account in this work. The typical appearance of the secondary phase precipitations on SEM micrographs can be gained in Figure 4.

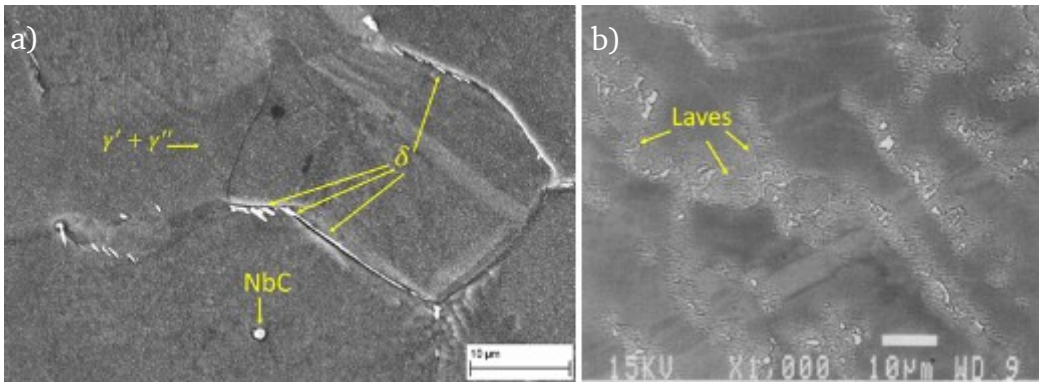

Figure 4: Secondary phase precipitates of nickel alloy 718 b) – adopted from [23]

The formation of carbonitrides occurs during the solidification of the material ingot. Minor amounts of carbon and nitrogen, which are presented in the melting as inevitable impurities, bond with titanium and niobium, well-known for their relatively high affinity to these elements [24]. The solvus temperature of carbonitrides (1218 °C) is significantly higher than the solvus temperature of γ' (908 °C), γ'' (960 °C) and δ (1000 °C). Therefore, no changes in the morphology of carbonitrides is expected during aging in the temperature range recommended in API-Standard API 6ACRA, [20].

Detailed study of the material microstructure variation in regards to the heat treatment conditions showed that γ', γ'' and δ are the only phases precipitating during the age hardening in the range from 500 to 1000 °C for 6 to 8 hours, [20]. Therefore, this work is primarily dedicated to γ', γ'' and δ phase and their impact on the material corrosion performance. The complex thermodynamic process of the secondary phase precipitation is schematically described via time-temperature transformation (TTT) diagrams, Figure 5.

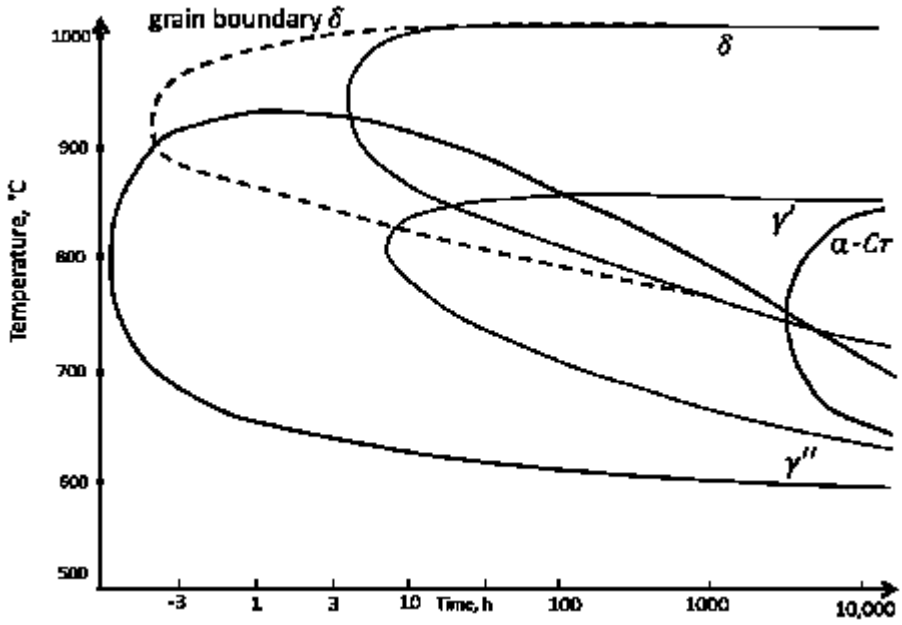

Figure 5: TTT diagram for nickel alloy 718 adopted from [20]

Secondary phase precipitations γ', γ'' and δ are based on the Ni_3X stoichiometry but possess different ordered structures: $L1_2$, DO_{22}, and DO_a, respectively, Figure 6. The body-centered-tetragonal structure of the γ'' phase can be equated to two stacked fcc γ' phases, [24]. Detailed review on each of them will be given in the following chapters.

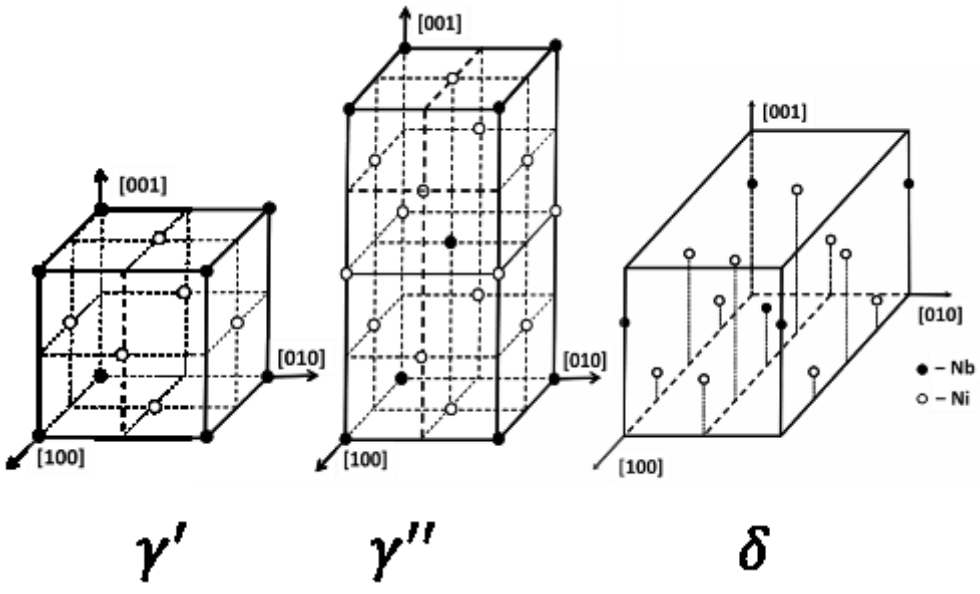

Figure 6: Unit cells of γ', γ'' and δ precipitations adopted from [25]

2.1.3 Gamma prime and gamma double prime precipitations

Gamma prime and gamma double prime ($\gamma' and\ \gamma''$) are the phase precipitations which

contribute to the material strength. Their strengthening effect is mainly achieved due to the coherency strains on the γ/γ' and γ/γ'' interface via its effect on APB energy in dislocation cutting, [24], [26], [27]. In comparison to other precipitation hardened nickel base alloys, the volume fraction of this precipitates are rather small: ca. 4% for fine dispersed spherical or cubical γ' precipitates ($Ni_3(Al, Ti)$) and up to 13% for the γ'' phase, [28]. Being mainly observed in a disc-shaped form, γ'' phases reveal $(001)_\gamma||\{001\}_\gamma$ and $[100]_\gamma||\langle 100\rangle_\gamma$ orientation to the matrix. With the estimated lattice misfit of about 0.407% for γ', [29], and 2,5% and 0,8% normal and parallel to the disc plane for γ'' phase respectively, [30], they are considered to be coherent to the γ matrix. The precipitation character of the γ'' phase is believed to be dependent on the γ' precipitation kinetic [31]. Both aging time and temperature influence the size and volume fraction of the intermetallic precipitations. Another major factor of influence on the precipitation kinetic is the chemical composition of the material. Among all the chemical elements, the concentration of niobium was found to make the greatest impact on the precipitation of the γ'' phase, [24], [32]. However, it was shown that the observed volume fractions exceed the theoretically predicted values. This discrepancy could be explained by the assumption that the γ'' precipitates could be formed with other alloying elements, such as molybdenum and titanium [26]. The nucleation of the γ' precipitates takes place mainly during cooling and/or heating to the isothermal annealing temperature, [33]. The earlier formation of the metastable γ' and γ'' phases in comparison to the δ phase has been attributed to the difference of the lattice mismatches, which are weaker in the case of γ/γ' or γ/γ'' interfaces in comparison to γ/δ interface, [34]. At low aging temperature, γ'' precipitates can nucleate on γ' precipitates, [25]. Several studies on the precipitation kinetics of the γ' and γ'' phases emphasize their co-location, [35], [36], [37], [38], [31]. That means that γ'' phase would precipitate on the γ/γ' interface. Isothermal coarsening of γ'' precipitates is in accordance with the theory of diffusion-controlled growth. The coarsening of the γ'' phases at a given temperature is proportional to the cube root of the aging time, [31], and can be written as follows, (1):

$$d^3 = 1.8 \cdot 10^{-21} t, \qquad if\ t < 1.44 \cdot 10^4 s$$
$$d^3 = 25.49 \cdot 10^{-21} t - 127.44 \cdot 10^{-21}, \qquad if\ t > 1.44 \cdot 10^4 s \quad (1)\ [39]$$

Where d is the particle length and t is the aging time.

At sufficient aging times (1) γ' and γ'' precipitates undergo the encounter process, i.e. coalescence of two or more neighboring particles, [40]. The coarsening of the particles leads to the loss of the coherency for the particles with the mean diameter above 50 nm, [25], [26], [41], [42], Figure 7. Loss of coherency should in turn correlate with the material hardness, [33].

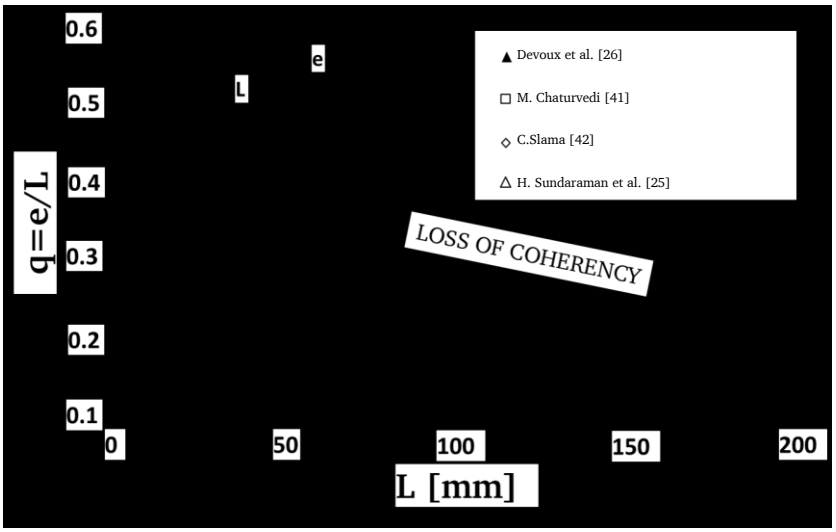

Figure 7: Correlation between the coherency of the γ'' precipitation and its diameter, adopted from [26]

Phase precipitations cause a redistribution of the alloying elements. Energy dispersive X-ray spectroscopy (EDX) line-scans of γ'/γ interface show enrichment in Al, Ti, Nb and Ni inside of the γ', but almost no Cr and Fe, indicating the migration of this alloying elements out from the precipitation zone, [43]. Outside of the precipitation zone, the concentration of Nb, Al, and Ti shows a strong declination. Similarly, γ'' precipitations were characterized by the increasing contents of Nb and Ni, whereas Cr and Fe were found to partition to the γ matrix, [38], [44].

2.1.4 Delta phase precipitates

Thermodynamically stable δ phase is a semi coherent orthorhombic phase ($D0_a$) with Ni_3Nb stoichiometry, Figure 6. It can be observed on the SEM micrographs in a form of plates or cells decorating the grain boundaries. In cases of overaged material, they may also appear within the grain or in form of globular precipitations on the grain boundaries, Figure 4. However, since the macroscopic observation of the δ phase is usually performed by means of two-dimensional SEM micrographs, this might be a result of the δ phases protruding to the grains interiors and being intersected by the cut, [45].

Some authors suggest that this precipitates might be formed due to excessive strains developed by large lattice misfit between the γ and the γ'' phase, [46]. The nucleation of the δ phase precipitation is observed throughout the aging process: fresh δ nucleation keeps up even when the first generation precipitates had grown considerably, [25]. Since nucleation of δ phase must consume a certain amount of niobium, its precipitation decreases the niobium concentration near the grain boundary. As the niobium is also the main formation element of γ'', its depletion around the δ phase would reduce the amount of the γ'' in the areas adjacent to the δ precipitations. Indeed, the presence of γ'' phase denuded areas in the vicinity of the δ precipitations was reported by several authors, [25], [45]. These γ'' phase depleted zones are believed to be more ductile than the surrounding matrix and therefore assumed to make an important contribution to the micromechanisms of intergranular crack propagation, [47], [45]. Atom probe tomography measurements on the δ phase embedded into the γ matrix revealed segregation of boron and phosphorus to the region of matrix/precipitation interface, [44]. Alike γ'' precipitates, niobium was found to partition to the δ phase, resulting in its depletion from the adjacent areas, [30]. When precipitated on grain boundaries the angle of the plates ranges from parallel to orthogonal, while for twin boundaries the precipitates are most frequently found fully or near-parallel with the twin boundary, [45]. Further, δ phase precipitates are also assumed to be responsible for the serration of the grain boundaries, Figure 8-d. The observed curvatures in the grain boundary in the presence of δ phase are attributed to the remaining attachment of the parent grain to one of the sides of the growing δ phase, [48]. Similar effect was observed by Ping et al., [49], for γ'' precipitates at the grain boundary, Figure 8-a, b and c.

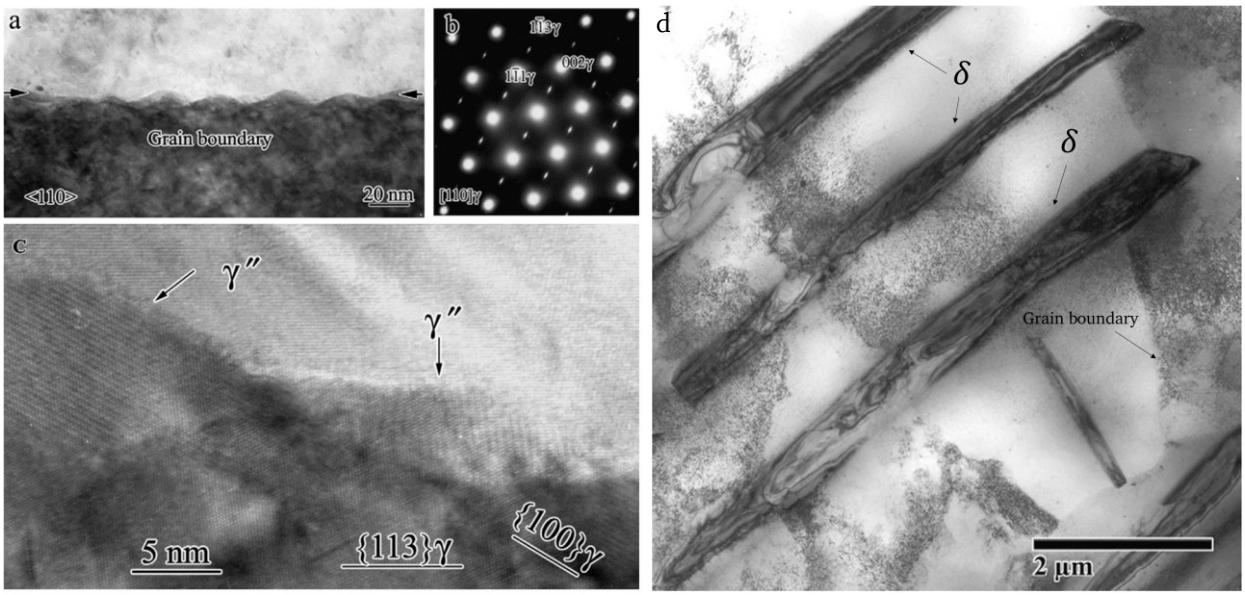

Figure 8: Serration of the grain boundary by the secondary phase precipitations:
(a) TEM bright field micrograph showing a gamma matrix grain boundary, which is free of any large precipitates, with a serrated grain boundary morphology. The image was taken with the electron beam parallel to the $\langle 110 \rangle_\gamma$ direction, adapted from [49]; (b) The selected area electron diffraction pattern from the lower grain with a dark contrast, adapted from [49]; (c) A high resolution TEM image from the boundary region, adapted from [49]; (d) TEM bright field image showing plate-like δ phase precipitates at grain boundary, adapted from [45].

In summary it can be said that since the nucleation of the secondary phase precipitations ($\gamma' + \gamma''$ and δ) is aligned with both material strength and distribution of the alloying elements, interdependency of the precipitation nucleation processes is expected to result in the variation of the mechanical and corrosive behavior of the material, produced according to the API 6ACRA.

2.2 Mechanisms of hydrogen evolution and transport

The offshore oil and gas environments are usually highly corrosive due to the presence of brine electrolytes, hydrogen sulfide (H_2S) and carbon dioxide (CO_2) gases and wide extremes of temperature and pressure, [50]. Both CO_2 and H_2S gases dissolved in aqueous electrolyte can become the source for atomic hydrogen (2), [51].

$$CO_2 + H_2O \leftrightarrow H_2CO_3 \tag{2-1}$$

$$H_2CO_3 \leftrightarrow H^+ + HCO_3^- \tag{2-2}$$

$$HCO_3^- \leftrightarrow H^+ + CO_3^{2-} \tag{2-3}$$

$$H_2S \leftrightarrow H_2S_{ad} \tag{2-4}$$

$$H_2S_{ad} + e^- \rightarrow H_{ad} + HS_{ad}^- \tag{2-5}$$

$$HS_{ad}^- + H^+ \rightarrow H_2S \tag{2-6}$$

$$H_{ad} + H_{ad} \rightarrow H_2 \tag{2-7}$$

At the same time, hydrogen can be produced as a byproduct of the cathodic corrosion reaction occurring on the metal surface, (3) [52].

$$nH^+ + ne^- \rightarrow \frac{1}{2}nH_2, (pH < 5.5) \tag{3-1}$$

$$nH_2O + ne^- \rightarrow nOH^- + \frac{1}{2}nH_2, (pH \geq 5.5) \tag{3-2}$$

Hydrogen evolution reaction is followed by one of the two following processes, [53]: electrochemical desorption reaction also known as Volmer-Heyrovsky reaction (4-1) and chemical desorption reaction or Tafel reaction (4-2).

$$H_{ads} + H_2O + e^- \rightleftarrows H_2 + OH^-, (electrochemical\ desorption) \tag{4-1}$$

$$H_{ads} + H_{ads} \rightleftarrows H_2, (chemical\ desorption) \tag{4-2}$$

In acidic electrolyte solutions hydrogen adsorption mechanism can occur in a single step according to the direct hydrogen entry model, [54], [55].

Adsorbed hydrogen can be solved in metallic structures by the interstitial solution mechanism, [56]. Dependent on the lattice type atomic hydrogen occupies either octahedral or tetrahedral sites, Figure 9.

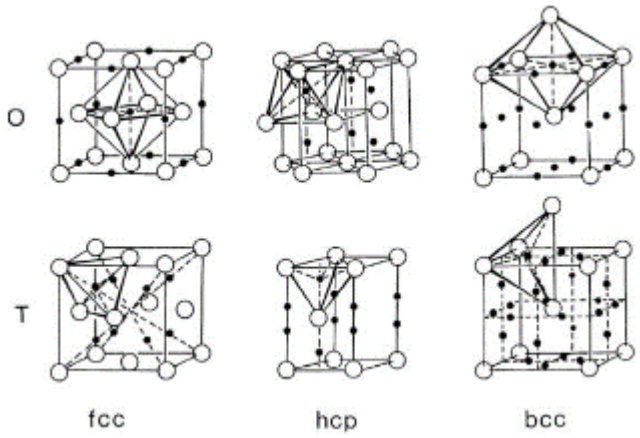

Figure 9: Interstitial sites (octahedral (O) sites and tetrahedral (T) sites) in fcc, hcp and bcc lattice adapted from [56]

Hydrogen tends to occupy octahedral sites in case of fcc lattice, whereupon tetrahedral sites are more attractive for hydrogen in materials with hcp and bcc lattice types. In the metal crystal structure hydrogen diffusion takes place by hopping of hydrogen atoms from one unoccupied interstitial site to another, [56]. Analytically this process is described by 1st and 2nd Fick's laws (5) and (6), [57].

$$j(x,t) = -D\frac{\partial C(x,t)}{\partial x} \tag{5}$$

$$\frac{\partial C}{\partial t} = D\frac{\partial^2 C}{\partial x^2} \tag{6}$$

Here j is hydrogen flux, x and t – coordinate and time, respectively, C – hydrogen concentration and D is the diffusion coefficient, given in m^2/s. The diffusion of hydrogen is a thermodynamic process which means that a certain activation energy value needs to be exceeded for the transition of hydrogen between the two interstitial sites, [56] and follows an Arrhenius law (7), [11]:

$$J = J_0 \exp\left(-E_p/kT\right), \tag{7}$$

Where J is permeability, J_0 is the preexponential factor, Ep is the activation energy necessary for the diffusion process, k is the Boltzmann constant and T is the temperature. Crystal defects, such as grain boundaries, dislocations, pores, vacancies or lattice distortions due to the intermetallic inclusions lead to the increase of the activation energy value. Thus, an increase of hydrogen concentration is expected in the vicinity of this defects (also called trapping sites). These trapping sites can be categorized into two main groups regarding

their binding energy (activation energy which is necessary for hydrogen to escape the trapping site): strong (irreversible) and weak (reversible) traps, [58]. The amount and type of hydrogen trapping sites is observed to have a certain impact on the hydrogen embrittlement susceptibility [59], [60]. Additionally to the lattice hydrogen diffusion, a large experimental evidence supports the theory of hydrogen transport by moving dislocations, [61], which was proposed by Tien et al in 1976, [62]. According to this theory hydrogen would surround a moving dislocation in the form of a so-called Cottrell atmosphere, [63]. Similarly to the lattice diffusion, hydrogen transport by dislocations is also a temperature-dependent process. It was experimentally observed that hydrogen cannot follow the dislocations at temperatures lower than 150 K, [64]. On the other hand, at higher temperatures, hydrogen diffusion rate would exceed the dislocation velocity. It is probably caused by this temperature dependency that the highest HE susceptibility is observed at room temperatures, [65], [66].

2.3 Mechanisms of stress corrosion cracking

Stress corrosion cracking (SCC) is the initiation and propagation of cracks in high strength metals which is caused by the combined action of a corrosive environment and a tensile stress, [67]. This definition implies that normally ductile materials would fail in an essentially brittle manner at relatively low stresses when exposed to certain environments, [68]. The kinetics of SCC depends on the chemical and metallurgical state of the material, such as its chemical composition, thermal condition, grain size, presence of secondary phases precipitates etc., [69]. Of the same importance however are the environmental factors (environment chemical composition, temperature, pressure, pH etc.) and the stress state (uniaxial, triaxial etc.), [69]. Depending on the chemical composition of the alloy and environment, SCC may appear in intergranular (IG) or transgranular (TG) form, [69]. The diversity of the SCC related failures impedes the elaboration of a unique model, which would describe the mechanism of this phenomenon. It is assumed that the material degradation occurs according to one of the following models [68]:

- Oxide film-induced cleavage
- Preferential dissolution model
- Hydrogen embrittlement
- Localized surface plasticity

In the models for SCC based on ***oxide film-induced cleavage***, the passive film is considered to be intact along the crack surface and to rupture only in a relatively small region of

sufficiently large strains. The passive film is regarded as a dimensionless brittle scale covering the metal surface. The fracture process is accounted from the fracture mechanical perspective and any synergy between the surface deformation and the corrosion processes is not concerned, [70].

The model of ***preferential dissolution*** assumes the onset of the local corrosion processes, such as pitting, to be the nucleation stage of the crack initiation, [71]. According to this model, the corrosion defects produced as a result of the interaction of a sliding band with a passive layer, expand sideways under mechanical stress and lead to the formation of a feathery fracture structure.

Hydrogen embrittlement (HE) is vastly considered to be one of the possible failure mechanisms causing environmental stress corrosion cracking, [7], [72], [73], [74]. It is usually manifested by a permanent loss of ductility in a metal or alloy, caused by absorption of hydrogen in combination with stress, either an externally applied or an internal residual stress, [75]. Since its discovery at the end of the 19th century, this phenomenon was a subject of an intensive research work. Numerous mechanisms, which were elaborated to explain the detrimental effect of hydrogen include: pressure theory, HEDE (hydrogen-enhanced decohesion), adsorption theory, HELP (hydrogen-enhanced localized plasticity), hydrogen and deformation assisted vacancy production, hydrogen-triggered ductile to brittle transition, hydrogen formation and cleavage, hydrogen- and strain induced phase transformation, and reactants with hydrogen. Detailed review of the mechanisms is given by Robertson and coworkers, [76]. Extensive experimental investigations on superalloy 718 account the HEDE, HELP and the vacancy production to be the main competing mechanisms of material degradation, [77], [78], [79], [80]. Therefore, this work mainly focuses on these mechanisms.

The HEDE mechanism assumes the accumulation of hydrogen at various trapping sites such as metal atoms in lattice (Figure 10-1), its accumulation at dislocations in front of the crack tip (Figure 10-2), carbides (Figure 10-3), and other lattice defects such as grain boundaries, intermetallic precipitates etc., and resulting reduction of interatomic bonds. This then leads to decohesion rather than dislocation slip, resulting in rather brittle material behavior on the macroscopic scale.

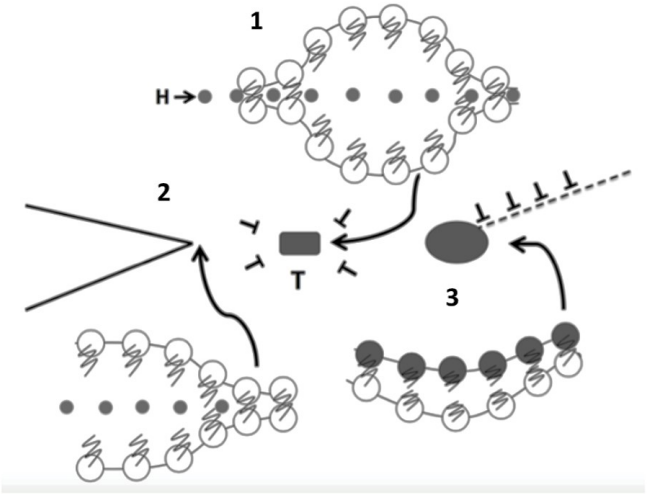

Figure 10: Schematic diagram, explaining HEDE mechanism of hydrogen embrittlement due to the weakening of the atomic bonds by (1) hydrogen in the crystal lattice, (2) hydrogen absorbed at the crack tip, and (3) hydrogen trapped at the inclusion-matrix interface adopted from [81]

The main experimental support of the reliability of this model is provided by the observed correlation between the hydrogen concentration and the notch stress reduction of the hydrogenated samples, [82].

In the HELP mechanism, hydrogen is envisioned to form Cottrell atmospheres ([63]) around dislocation cores which may accelerate dislocation motion or decrease dislocation-dislocation interactions, leading to an increase in local plasticity and subsequent failure by exhaustion of the material plastic strain capacity, Figure 11.

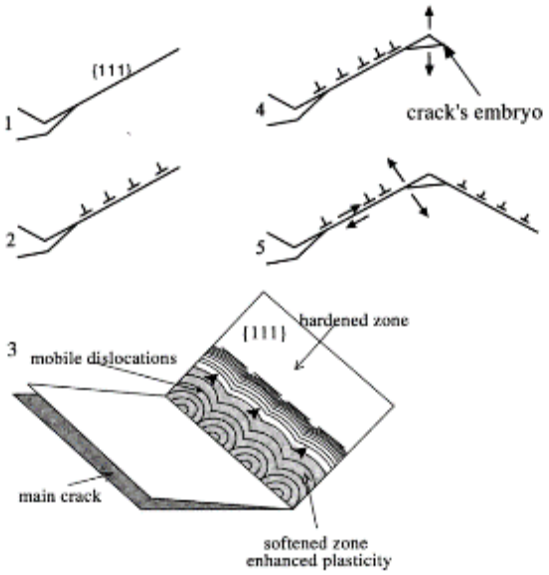

Figure 11: Schematic diagram, explaining HELP mechanism of hydrogen embrittlement, adopted from [83]

The model implies the formation of a critical defect as a necessary step for the enhanced hydrogen adsorption – stage 1. In corrosive environments this could be a result of local anodic dissolution on {111} slip planes. The absorbed hydrogen promotes the shear stress localization along the {111} slip planes and enhances the dislocation movement – stage two. During stage 3 two different zones are formed in the vicinity of the main crack tip: the zone of the enhanced plasticity caused by the hydrogen interaction with the emitted dislocations and a previously hardened zone. This configuration leads to the formation of the dislocation pile-ups on the interface between this two zones and the resulting generation of a new crack embryo – stage four. During stage five a crack opening along the {111} plane occurs due to the normal stress and the process goes on. As a result the typical zig-zag crack path is formed, which can be observed on the fracture surfaces of the hydrogenated specimens. The main support for this mechanism is provided by experimental observation of the enhanced dislocation motion in hydrogenated samples, [84], and localized slip bands in the vicinity of the crack tip in the presence of hydrogen, [85], [86]. Another indirect support for the HELP theory is given by the temperature dependency of the HE phenomenon. The maximum of the HE susceptibility observed near the room temperature implies the correlation between the hydrogen diffusion and the mobility of dislocations at a given strain rate, [66].

The theory of the vacancy formation was recently suggested by Martin and co-workers, [78], who were inspired by the fracture mechanics and microscale physical fracture investigations. It is proposed that nanovoids nucleate at the intersection between the dislocation slip bands (DSB) (Figure 11-2) and propagate along them (Figure 11-3). Hydrogen is assumed to assist in the development of the intense slip bands, lower the stress required for the nano-void formation and expansion, leading to a crack that will propagate along the slip bands (Figure 11-4) in the presence of hydrogen.

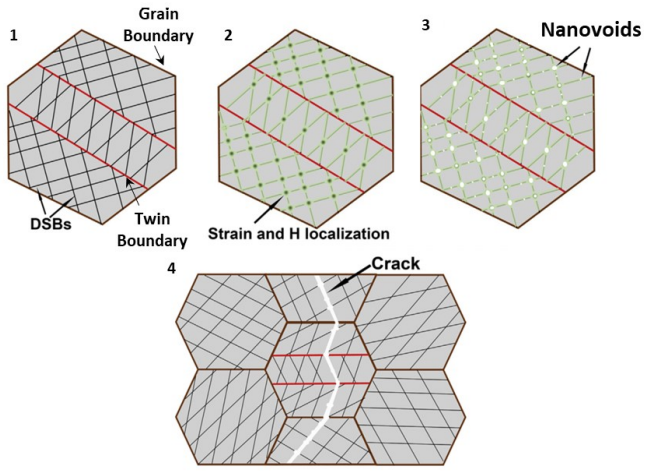

Figure 12: Schematic diagram, explaining void-formation mechanism of hydrogen embrittlement, adopted from [87]

The 4th model of SCC fracture mechanism – ***localized surface plasticity*** – is based on corrosion-deformation interactions at the crack tip. For a detailed description of the process sequence should be referred to [66]. The model presupposes an existence of the crack tip, where the rupture of the oxide film becomes inevitable. Oxide film damage leads to a localized corrosion attack along the slip planes, combined with enhanced local hydrogen absorption. Further, the degradation occurs due to the HELP mechanism.

Common for all of the proposed mechanisms is the degradation of the protective passive film (thin – tens of nanometer – amorphous semiconducting oxide layer [88]). It can occur either due to the change of environmental conditions or because of mechanical damage or due to its local dissolution on the most weak sites (such as precipitations, grain boundaries etc.). As a result of the passive film damage, an increased anodic dissolution (1st, 2nd and 4th models) or increased hydrogen adsorption (3rd model) would occur and thus enhance the material susceptibility [66].

In summary, it can be said that the existence of an incubation time of failure, necessary for the crack nucleation during SCC testing, indicates that the damage process is probably caused by the localized corrosion, followed by crack propagation under the influence of hydrogen, [68]. In contrast to that, during HE damage, hydrogen is believed to be involved in both crack initiation and crack growth processes, [83]. Further, it should be emphasized that for corrosion-resistant alloys oxide film remains the main factor influencing the material performance since it reduces the effective hydrogen solubility, [89]. Therefore, local damage of an oxide film would lead to the locally enhanced hydrogen uptake and thus to the risk of the hydrogen supported crack nucleation or propagation. Stress corrosion cracking of a duplex stainless steel in H_2S containing brine is the best example, illustrating this statement, [90].

2.4 Mechanisms of localized corrosion

As it was stated in chapter 2.3, localized corrosion form (pitting, crevice, Stress Corrosion Cracking (SCC)) is considered to be a very likely degradation mode in case of the failure mechanism of alloy 718 for oil and gas applications. Material resistance to localized form of corrosion is determined by the stability of the passive layers. These layers are amorphous semiconducting films, which can retard the corrosion process and change its character from active (anodic dissolution rate increases with time) to passive (decrease or invariability of the anodic dissolution rate with time) dependent on their homogeneity, solubility and reactivity in the given environment. In reality the thickness of the passive films reveals lateral gradients dd/dy, which may reach from 10^{-6} to 10^{3}, [88]. Although the observation of the passive film growth is rather difficult, it is assumed that it begins on the energetically weak sites, such as dislocations, voids or other surface defects, [91]. The

presence of some defects in the passive layer such as heterogeneities in the chemical composition (metallic and/or non-metallic inclusions) or structural defects (grain boundaries or dislocations) represent potential sites for the local corrosion attack. Although there are some distinct differences between the pitting and crevice corrosion, regarding the processes of mass transfer of species during the corrosion reaction, the possible mechanisms by which the film breaks down are those of pit initiation with the difference being that for crevice corrosion the environment becomes more aggressive with time, [92]. Complex processes leading to the localized corrosion usually occur in two steps: passive film breakdown and following *pit growth or re-passivation*, [93].

All mechanisms of the passive film breakdown given in the literature could be summarized into 3 groups of models, [94]:

1) ***Adsorbed ion displacement models*** assume that anionic species, such as Cl^- ions are adsorbed on the energetically favorable sites. The adsorbed chlorides contribute to the thinning of the passive film. The reduced thickness of the passive layer leads to the increase of electric field strength within the passive film $\Phi(V)$ and related corrosion current density i_c, which in turn results in the enhanced metal ion migration. Under certain circumstances, this can cause a local elimination of the passive layer with the localized corrosion rate and final free corrosion current density $i_{c,h}$ several orders of magnitude larger than that of the intact passive film ($i_{c,p}$), Figure 13-a.

2) ***Ion migration or penetration models*** suggest the migration of Cl^- ions through the defects in the passive layer (pores, local paths with increased conductivity). Metallic ions can work their way out of the metal easier through this defects. Therefore, the protective ability of the passive film can be significantly reduced, Figure 13-b.

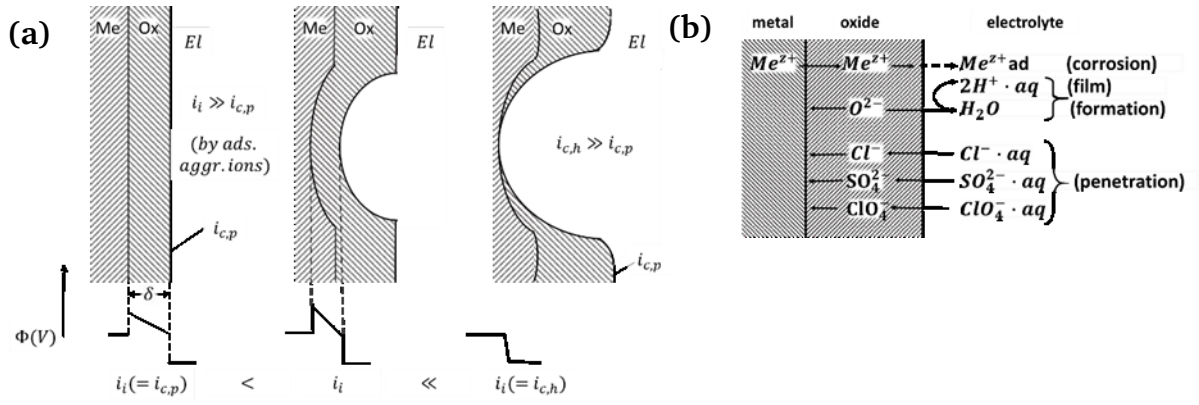

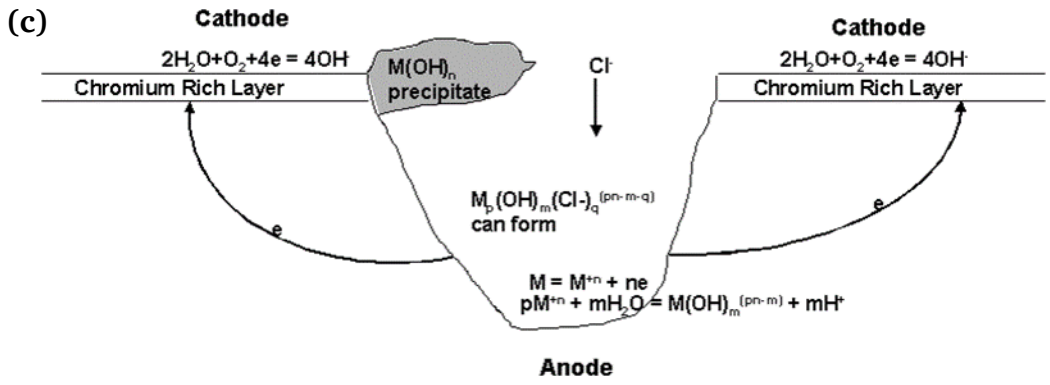

Figure 13: Mechanisms of passive film breakdown (a) adsorbed ion displacement model, adopted from [23]; (b) Ion migration or penetration model, adopted from [95]; (c) breakdown-repair model, adopted from [31]

3) ***Breakdown-repair models*** presume chemical or mechanical disruption of the passive film followed by increased anodic dissolution of the unprotected metal exposed to the corrosive environment, Figure 13-c.

Once the passive layer has been damaged, the active site can either undergo the repassivation according to the ***salt-film building mechanism*** or the pit growth process upon the so-called ***acid-theory***.

The theory of the salt-film building assumes the ohmic voltage drop in the pit bottom as a result of the generation of a highly resistive, dense and poreless salt film, [93]. The electrochemical potential of the pit nucleation site is in the active range, whereas the potential of the residual passive area is rather passive. The potential difference between the active and passive areas can reach up to several hundreds of mV.

The main factor of impact in the acid theory is the drop of the pH on the pit bottom, which is caused by the hydrolysis reaction of the released metal ions, (8-2).

$$Me \rightarrow Me^{z+} + ze^{-} \qquad (8\text{-}1)\,[91]$$

$$\downarrow$$

$$Me^{z+} + nH_2O + nCl^{-} \rightarrow Me(OH)_n^{(z-n)+} + nH^{+} \qquad (8\text{-}2)\,[91]$$

$$\downarrow$$

$$Me^{z+} + nH_2O + nCl^{-} \rightarrow Me(OH)_n^{(z-n)+} + n\boldsymbol{HCl} \qquad (8\text{-}3)\,[91]$$

The increased concentration of H^+ cations promotes the accelerated migration of the Cl^-

ions to the pit bottom, where hydrochloric acid can be generated (8-3).

Considering those aspects, the general tendency of the material towards localized form of corrosion depends both on the density and stability of the present passive layers and the ability of the material to rebuild these layers in case of a damage. Another significant factor of influence is the chemical composition of the corrosive environment and in particular the presence of halide ions such as sulphur or chlor and its acidity, which is determined by the amount of the dissolved hydronium ions.

2.5 Synergistic effects of hydrogen and corrosion processes

Hydrogen solved in the bulk reveals a detrimental effect not only on the mechanical properties of the material, but also on its corrosion resistance. Several authors reported a negative impact of hydrogen on the properties of oxide films, formed on the metal surface, [96], [97], [98], [99], [72], [100], [101], etc. Smith and coworkers [102] imply that hydrogen presence in the material leads to reduction of the oxide film, creating a porous structure, which permits both rapid inward and outward diffusion. Ejaz et al. [100] pointed out that hydrogen retards the passive film formation and therefore decreases its stability in the range of passive potential with or without chlorides present in the corrosive environment. They suggested that interstitial hydrogen would initiate the charge transfer along the metal surface and extend the metal atomic bonds, thus making the metal surface more chemically active. Young and Scully [103] stated that hydrogen uptake introduces vacancies into the oxide, which in turn leads to an increased metal dissolution rate. On the other hand, the release of adsorbed hydrogen from the metal would generate H^+ ions thereby reducing the local pH value on the electrode surface. At the same time hydrogen adsorption kinetic strongly depends on the stability of the oxide film [104], [105], [90]. An increase in hydrogen uptake rate was experimentally observed in case of various metallic materials, when oxide layer was either removed from the surface [104] or damaged by the ongoing corrosion processes [90].

Taking into account that SCC damage mechanism include local damage of the protective passive layers and hydrogen adsorption as a preliminary stage of the following material degradation due to HE, the synergistic effects between hydrogen and corrosion processes should be taken into account in context of the material microstructure as they might make a significant impact on both of the mentioned processes.

2.6 Methods of material examination

2.6.1 Characterisation of material microstructure

Phase precipitations impact on both mechanical and corrosion performance of the material raises the question about precise and reliable methods for the quantification of the precipitations content. The approaches reported in the literature can be classified into two groups: quantitative stereological methods [106] and X-ray diffraction [107], [108]. The quantitative stereological approach was elaborated by Underwood et al. [106] and is based on the statistical evaluation of the samples light microscope or SEM micrographs. Although this method can be highly time-consuming, it is easy in the implementation, and does not require any special equipment except for the devices necessary for the microscopic analysis. The principles of this approach are adopted in the well-known method for the grain size determination – ASTM E112, [21].

There are several reports in the literature about successful application of the X-ray diffraction method for the determination of the precipitations with different crystallographic structures, [47], [34]. The working principle is drawn upon a constructive interference of monochromatic X-rays and a crystalline sample. The interaction of the incident rays with the sample produces constructive interference (and a diffracted ray) when conditions satisfy Bragg's Law, [109]. Dependent on the type of the crystals in a sample, their amount and the lattice constants each sample could exhibit a unique scattering pattern. In the case of over-aged material in the absence of γ' and γ'' the δ phase content may be determined non-destructively and within a relatively short time by direct comparison of the integrated intensities of X-ray scattering patterns, [110]. Yet similar crystallographic structures of γ' and γ'' may result in overlapping XRD-peaks. Therefore, the knowledge of the relative fraction between γ' and γ'' is necessary for the accurate data interpretation, [111]. Since the distinction between γ' and γ'' is everything but a trivial task, the XRD method has a serious application limitation for the given purpose.

2.6.2 Examination of localized corrosion susceptibility

Immersion test is a relatively simple approach for testing of the localized corrosion susceptibility of the material, [112], [113], [96], [114]. The detailed description on the test purpose, performance and evaluation is given in the standard ASTM G31 [113]. During the test, samples are immersed into a corrosive electrolyte at a requested temperature for a certain period of time. After the test the extent of corrosion attack is evaluated by means of light microscopy. In some cases the information, provided by the immersion tests is not enough for the adequate material evaluation. Monitoring of the Open Circuit Potential (OCP) during the sample immersion could be performed to complement the obtained data, [115]. OCP is the electric electrode potential of a metal surface, which is formed in contact

with an electrolyte solution. The value of the OCP is measured in relation to the reference electrodes, such as calomel or silver/silver chloride and can be used as a qualitative characteristic of the corrosion process of a metallic surface. Alteration of the OCP over the testing time can either indicate a passivation process (potential increase) or metastable or stable pitting growth (potential transients or potential decrease), [115].

Potentiodynamic polarization tests is one of the most popular tools for study of the localized corrosion. The details according this testing approach are given in the standard ASTM [116]. Polarization curves are measured using controlled potential at a constant rate by recording the system response in form of the corrosion current density. The material resistance against localized corrosion is evaluated by means of the critical pitting potential E_{pit} (also called breakdown potential), at which the anodic current density experiences rapid increase (>100 $\mu A/cm^2$), [117], [118]. The value of the pitting potential is strongly dependent on the experimental conditions as well as the scan rate.

Electrochemical Impedance Spectroscopy

Electrochemical impedance spectroscopy (EIS) is a powerful technique for the investigation of electrochemical and corrosion systems. The working principle of this approach is based on the measurement of the time-dependent current response I(t) of sample surface to sinusoidal polarization V(t) at a variable angular frequency ω. With the knowledge of these two functions, it is possible to derive the frequency dependent impedance value $Z(\omega)$, which is used for the analysis of electrical properties of the oxide layer, (9).

$$Z(\omega) = V(t)/I(t) \tag{9-1}$$

$$V(t) = V_0 sin\omega t \tag{9-2}$$

$$I(t) = I_0 \sin(\omega t + \theta), \tag{9-3}$$

where t=time and θ = phase angle between V(t) and I(t).

The impedance behavior of an electrode may be expressed in Nyquist plots of $Z''(\omega)$ as a function of $Z'(\omega)$ or in Bode plots of $log|Z|$ *and* $log\theta$ versus frequency f in cycles per second (Hz), where $\omega = 2\pi f$.

It is a very sensitive, rapid and nondestructive quasi-stationary electrochemical approach to study electrochemical reactions at the electrode/electrolyte interface. The advantage of EIS is that the electrochemical system is only slightly deflected from the stationary state (10 mV), without changing the system irreversibly. However, data interpretation may be

ambiguous and difficult. Details on this approach can be gained for example in the standard ASTM G61-86 [116].

Electrochemical noise technique is another non-destructive electrochemical approach for the investigation of localized corrosion, which has gained popularity in the recent years, [119], [120], [121]. With the use of this method, it is possible to detect the low-level spontaneous fluctuations of potential and current that occurs during an electrochemical process. These spontaneous fluctuations are the consequences of the small transients in the electrical charges occurring on the sample surface during the electrochemical corrosion as a sequence of individual random events. The measurements are generally performed in a four-electrode system. Recorded in form of electrochemical noise, they could be analyzed statistically to derive some kind of a "fingerprint" of the amount of dissolved metal, depending on the combination of metal and the environment. There are several methods for the analysis of the noise data specifically suitable for the investigation of localized forms of corrosion. Most popular among them are the statistical methods as the pitting index and power spectral density analysis, or spectral analysis. These fluctuations are generally measured by a three-electrode system.

Kelvin probe force microscopy (KPFM) is a measurement technique that allows measurement of the surface potential in the nanometer-scale resolution. During the measurement, a contact potential difference (V_{CPD}) between the sample surface and the tip is determined as a difference of the work functions (minimum work, required for extracting an electron from the surface of some material) of the sample and the tip divided by the electronic charge, (10).

$$V_{CPD} = \frac{\phi_{tip} - \phi_{sample}}{-e} \qquad (10)\ [122]$$

KPFM measurements can be performed in air and do not necessarily require an inert atmosphere. A great review on the measurement principles can be found elsewhere [122], [123]. This measurement technique got its widespread use after the publication of Schmutz [124], who demonstrated the correlation between the Volta potential differences measured on aluminum alloy surfaces via Scanning Kelvin Probe Force Microscopy (SKPFM) with the observed localized corrosion behavior of the samples.

2.6.3 Examination of hydrogen embrittlement susceptibility

Slow strain rate (SSR) testing of alloys under cathodic polarization is the most common testing method to determine a material's susceptibility to HE in highly corrosive, hydrogen

containing environments, [125]. Loss of strength [126], ductility [83] or reduction of area [127] of hydrogenated samples, compared to material performance in inert media, can be expressed in terms of ratios for the evaluation of the general material susceptibility to HE, (11):

$$HE = \frac{X_H}{X_{inert}} \tag{11-1}$$

or

$$HE(\%) = \frac{X_{inert} - X_H}{X_{inert}} * 100\% \tag{11-2}$$

with X standing for any of the mentioned physical values. Indexes “H” and “inert” imply that the values were measured on the samples in hydrogen containing or inert environments, respectively. Ratios in the range 0.8-1.0, measured according to (11-1) normally represent high resistance to environmental assisted cracking (EAC), whereas low values below 0.5 show high susceptibility to EAC, [128]. Plastic deformation during cathodic hydrogen charging was found to increase the permeation rate and effective diffusivity of hydrogen in nickel by 10^5 times, [129]. Therefore, simultaneous introduction of hydrogen during the SSR testing is expected to increase the sensitivity of the testing method. Thus, HE appears as a surface phenomenon related only with the accumulation of hydrogen in the near surface region, [130]. Comparative study of the HE sensitivity in regards to the temperature and strain rates reveal that the most severe HE susceptibility is observed at room temperatures and is found to be inversely proportional to the strain rate [66]. At slow rates, dislocation sweeping of hydrogen takes place and HE is more pronounced, [83]. On the other hand, Chène and Brass reported a direct proportionality between HE and the strain rate of nickel alloy 600 at elevated temperatures (423-473 K), [97].

Another approach for the evaluation of the HE susceptibility is based on the determination of the total work of local fracture, emanating from the notch which can be determined

according to

Figure 14, [131].

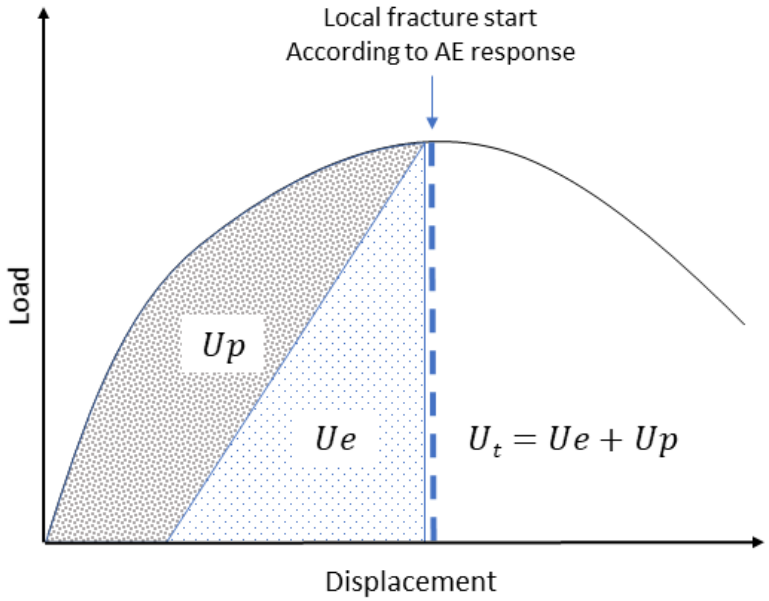

Figure 14: Total work of local fracture, emanating from the notch (U_t); definition of its plastic U_p and elastic U_e parts, adopted from [131]

The degree of the susceptibility of metal material to hydrogen embrittlement can be defined as a ratio of the work of fracture corresponding to the plastic deformation, U_p, to the total work of fracture, U_t, given in percent, which will decline with increasing material susceptibility.

The crucial moment of this approach is the determination of the local fracture start, which is performed by means of acoustic emission (AE) signal analysis, [131].

2.6.4 Hydrogen permeation measurements

There are several experimental approaches for studying hydrogen diffusion processes. They are based on measuring of the change in a physical quantity in the presence of hydrogen, such as mass, volume, strain [132] or even electrical resistance, [133]. One of the most commonly used techniques for the measurement of hydrogen permeation was introduced in 1962 by Devanathan and Stachurski, [134], and is a basis of the current standard procedures for hydrogen permeation measurements, such as ASTM G148-97 [135] and

DIN EN ISO 17081 [136]. The principal experimental setup consists of two electrochemical cells (oxidation and reduction cells), which are separated from each other by the flat material sample, Figure 15.

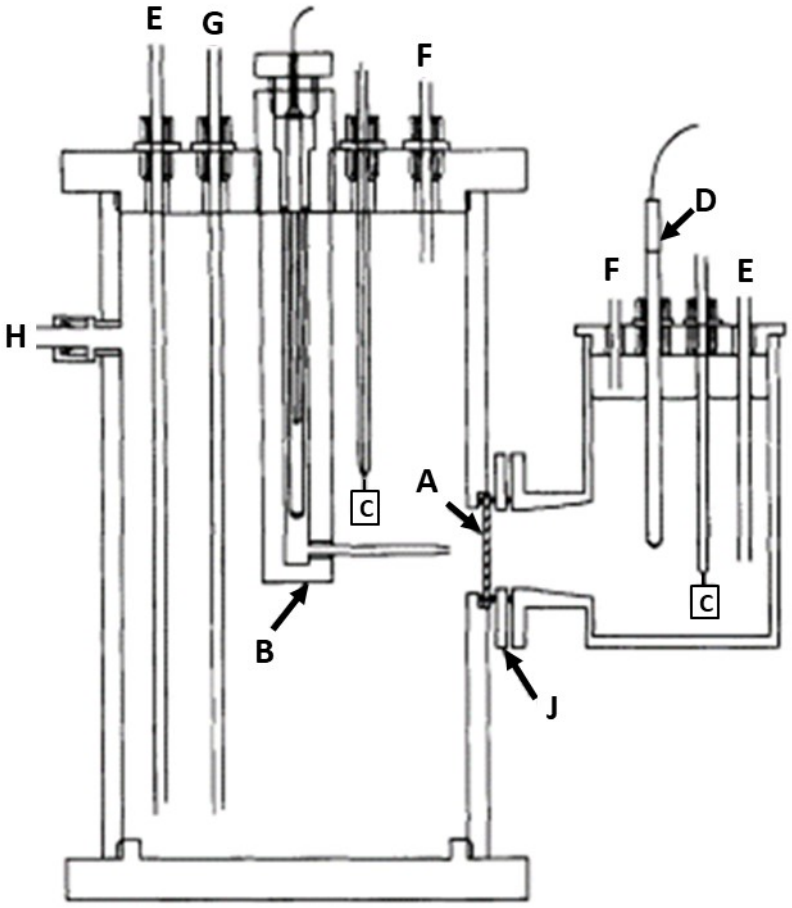

Figure 15: Hydrogen permeation cell, proposed by Devanathan and Stachursky, adopted from [137]: a) Specimen; b) Double junction reference electrode in PTFE Luggin capillary; c) Platinum counter electrodes; d) Double junction reference electrode; e) Gas inlet; f) Gas exhaust; g) Solution inlet; h) Solution out; j) Specimen clamp

During the measurement hydrogen, introduced into the sample in the reduction cell (on the left side of the sample), permeate the tested sample and exit on the right side to be detected by the three-electrode arrangement system, connected to the potentiostat. The reduction cell of the permeation setup is filled with conductive medium, which would not participate in a chemical reaction with the sample surface, such as 0.1 M NaOH solution. The cell is polarized to a constant potential at which each of the hydrogen atoms escaping the exit side would be oxidized ($+300\ \mathrm{mV_{SCE}}$) and measured in form of the permeation transient current density $i_p(t)$. Under this condition hydrogen concentration on the exit side is assumed to be zero throughout the test duration. Thus, introduction of hydrogen on the reduction side would create a hydrogen concentration gradient, favorable for the

diffusion process in a given direction. If the concentration of hydrogen, offered on the entry side of the sample remains constant, a raise in the permeation current density up to the maximum stationary value i_∞would be observed over the testing time. Hydrogen diffusion coefficient can then be derived from the slope of the permeation current density versus time according to the time-lag method, (12):

$$D_{eff} = \frac{L^2}{6t_{lag}} \tag{12}$$

Where the t_{lag} is the moment of time at which the permeation current density equals 63% of the stationary permeation current density i_∞, Figure 16, and L is the sample thickness.

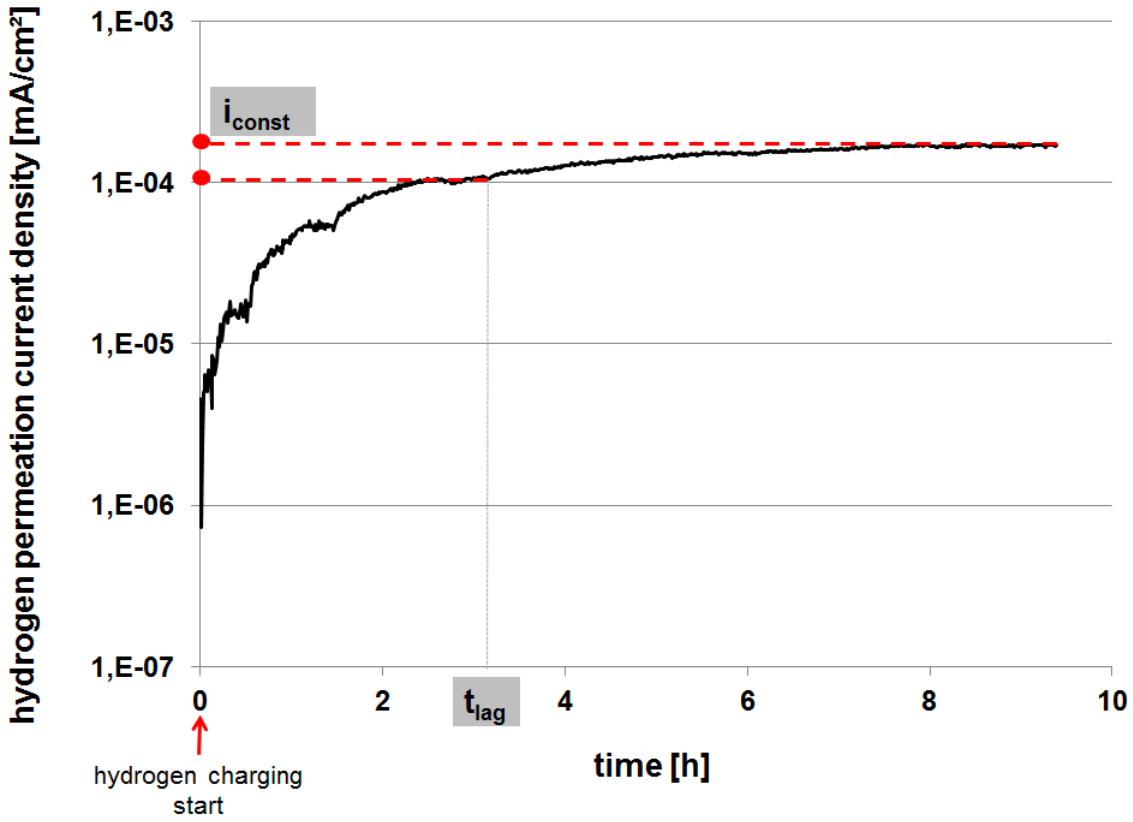

Figure 16: Time lag method for determination of effective diffusion coefficient

It is obvious that the precision of the hydrogen diffusion coefficient determination is directly associated with the accuracy in the measurement of the permeation current. Thus, reliability of the hydrogen oxidation reaction is of a crucial importance. Application of a thin palladium layer on the exit side of the specimen significantly increases the oxidation reaction of hydrogen and minimizes the fraction of hydrogen recombination, [138]. On the other hand, presence of an oxide layers of the sample surface might act like a barrier

to hydrogen permeation, hindering hydrogen from the emission from the sample. Application of a thin palladium coating prevent the undesired oxidation and therefore assures an accurate measurement implementation, [139], [140].

2.6.5 Hydrogen solubility measurements

Measurements of the total amount of hydrogen, introduced into the samples due to the cathodic charging or cathodic corrosion reaction, are usually performed by extracting hydrogen at temperatures above the melting point, [61]. Small material specimens containing hydrogen are entirely melt down in a graphite crucible surrounded by pure inert carrier gas, such as nitrogen or argon. The released hydrogen is carried with the gas flow to the mass spectrometer or thermal conductivity sensor, which is set up for H_2 detection. The amount of the desorbed hydrogen is equal to the integral of the measured curve (m(t)) over the time and can be expressed in weight ppm.

2.6.6 Approval test by ISO 15156-3 / NACE MR 0175

The standard ISO 15156-3 / NACE MR 0175 specifically concerns testing approaches and experimental data interpretation for the selection of Cracking-Resistant Alloys (CRAs) in oil and gas application field, [7]. The standard includes a list of the pre-qualified materials organized in regards to the severity of the application conditions. CRAs can be qualified based either on field experience or on laboratory testing. For the material approval based on field experience, documentation of the service conditions and material performance should be executed for a minimum period of two years. Laboratory testing could be performed to qualify new materials, which are not on the NACE MR 0175/ISO 15156 prequalified lists. The main aim of the standard procedure is to ensure the correct material selection for the intended environment, [141]. Annex E of the standard specifies the corrosion exposure conditions, which are subdivided into 7 different groups. The variation of temperature, partial pressure of H_2S and CO_2 gases, sodium chloride concentration, pH level of the electrolyte, and in some cases content of elemental sulfur is used to find the best match for the expected aggressiveness of area of application. Requirements on the superimposed mechanical testing are based on the standard NACE TM0177, which should be used for detailed definition of the test procedures. The experiments can be performed on smooth samples in form of a constant load test, a sustained load test or a constant elongation (constant displacement). Tension can be applied in uniaxial (simple tensile tests), 4-point bending or C-ring-test manner. An average experiment can take up to 720 hours per tested sample.

Summarizing this brief review of the possible approaches for the assessing the performance of the nickel alloy 718 in regards to its susceptibility to SSC, SCC or HE, it can be said that the testing approach by ISO 15156-3 / NACE MR 0175 is probably the most

challenging in the implementation and also time consuming. Despite the severely aggressive electrolytes, its applicability to the service conditions can still be argued. On the other hand, information gained from the experiments performed according to the alternative testing methods such as electrochemical potentiodynamic scan or SSR tests under cathodic hydrogen charging may help gaining information necessary to link the material microstructure with its performance.

2.7 Properties of nickel alloy 718

2.7.1 Corrosion resistance of the nickel alloy 718

The reports regarding the susceptibility of alloy 718 to environmental assisted cracking are rather controversial, [128]. According to the standards ISO 15156-3 and NACE MR 0175, nickel alloy 718 is acceptable in the solution heat-treated and precipitation hardened condition to HRC maximum (40 HRC), [7]. At the same time Hibner and Puckert reported the results of the NACE MR 0175 testing in which nickel alloy 718 was only qualified to NACE Test Level V performed on the C-ring corrosion cracking test, [142]. Some of the laboratory data found in the literature indicate the resistance of nickel alloy 718 to stress corrosion crack initiation, [9], [128], [143], [144]. However, relatively small defects could lead to rapid crack growth. On the other hand, the corrosion resistance of the material can be insufficient in the most severe corrosion environments, [114], [9]. It is agreed that the SCC behavior as well as the pitting susceptibility of alloy 718 is strongly correlated to its microstructure, [9], [13], [143]. Comparative study of the SCC performance of two different heats of alloy 718 clearly demonstrated negative effect of large secondary inclusions, such as δ, Laves or coarse MC-type carbonitrides, [13]. In contrast, material microstructure with homogeneous distribution of fine transgranular $\gamma' + \gamma''$ phases revealed nearly immune behavior. At the same time, materials with δ-free grain boundaries revealed SCC susceptibility (IGSCC) even at low applied stress in a pressurized-water (PWR)-like testing conditions, [145]. The results of other investigations on SCC performance of alloy 718 performed by Kimberly et al. imply a negative impact of δ phases on the material corrosion behavior, [146]. The authors suggest that segregation of alloying elements, such as chromium or niobium, occurring during the δ phase precipitation, might lead to the change of the local potential distribution on the surface. As a result, δ phase would act as a local cathode, forcing the neighboring matrix to anodic dissolution. Same conclusion about the cause for SCC degradation was made by Groh et al., [117], who proposed a local passive film interruption at secondary phase particles (such as carbides, nitrides, carbonitrides and possibly δ phase) as a possible failure mechanism. The link between the SCC and pitting susceptibility of alloy 718 is also supported by the strong temperature dependency of these two forms of the material degradation, which was observed and reported by several authors, [147], [51], [114], [148], [149].

2.7.2 Hydrogen diffusivity and solubility in nickel base alloy 718

As it was stated in chapter 2.2, hydrogen transport in metals occurs by the hopping of hydrogen atom from one interstitial site to another. Due to the high hydrogen solubility, hydrogen diffusion is known to be rather slow in the materials with fcc lattice. For example, hydrogen diffusion in nickel (fcc) is about 5.4 x 10^{-10} cm^2/s, [150], in comparison to iron (bcc) with 7.2 x 10^{-7} cm^2/s, [151]. Several researchers have studied the process of hydrogen propagation in alloy 718. For example, Jebaray et al. estimated the hydrogen diffusion coefficient of nickel alloy 718 to be of the order of 10^{-11} m^2/s, [50]. By varying the sample microstructure, it was also demonstrated that both dislocations and the secondary phase precipitations act as reversible hydrogen trapping sites in this material. Binding energy of about 30 kJ/mol was associated with δ precipitates in the study of hydrogen permeation by Turnbull et al, [137]. At the same time, binding energies of γ' and γ'' were estimated to be between 31 – 37, and 23 – 27 kJ/mol respectively. Having in mind that sites with energies more than 58 kJ/mol are regarded as irreversible, [152], hydrogen trapped at the secondary precipitation phases can be considered as diffusible. In contrast to that, hydrogen will be irreversibly trapped at carbide particles with activation energy of 77-87 kJ/mol, [137], and standard mixed or screw dislocation cores (60 kJ/mol), [153]. At low temperatures (room temperature) hydrogen dissolved in the lattice can be dragged with the moving dislocations at a relatively slow strain rate, [154].

Grain boundaries in polycrystalline nickel with binding energies of 12 to 20 kJ/mol can be considered as reversible hydrogen traps, [155]. Therefore, under exposure to hydrogen they are likely to become saturated with hydrogen and provide a path for accelerated hydrogen diffusion. Enhanced hydrogen transport by short-circuit diffusion, associated with crystalline defects in nickel, has been intensively studied in the past decades, [156], [157], [158], [159]. Studies on nanocrystalline nickel revealed a strong segregation of hydrogen at grain boundaries and an increased diffusion coefficient along the boundaries above a certain H-coverage of grain boundaries, [160]. In addition, the diffusion coefficient increases proportionally to the hydrogen concentration. However, a decrease of the grain size might lead to an increase in trapping sites, and trapping effects become more dominant in the mechanism of hydrogen transport, [158]. Although no detailed investigation of the grain boundary impact on hydrogen diffusion rate was found in literature for alloy 718, similarities in the materials crystallography implies analogical diffusion behavior.

There are very few literature reports on the hydrogen solubility in alloy 718. Measurements of the hydrogen solubility, performed on the material samples, cathodically charged in a melted salt, demonstrated a wide scatter of the obtained results depending on the microstructure, [80]. In this study solution annealed samples revealed the highest hydrogen content (900 wt. ppm), whereas aged material exhibited significantly lower values:

about 70 wt. ppm for the specimens with high amount of fine $\gamma' + \gamma''$ and nearly 200 wt. ppm for the overaged material with high content of acicular δ phase precipitations. The increase of the hydrogen solubility due to the δ phase precipitations might correlate with the very high hydrogen solubility in niobium, which can get up to 730 ppm, [161]. Indeed, Robertson has noted that for a given chemical composition, the solubility of H atoms in a nickel-based solid solution enriched with niobium strongly depends on the location of the niobium, i.e. a substitutional position or an intermetallic phase, [162]. At the same time, study of the hydrogen solubility in γ'' and δ phase precipitations revealed that hydrogen atoms do not segregate into precipitates and would rather occupy the matrix/precipitation boundary, [163]. Experimental observations on the impact of Ni_3Nb phase on the spatial distribution of hydrogen confirm this suggestion. SEM micrographs of the Ni-Nb model alloy charged with hydrogen and immersed into the $KAg[K(CN)_2]$ aqueous solution for hydrogen visualization, clearly demonstrated agglomeration of the reduced silver in the regions of δ/matrix interface and therefore indicating enhanced hydrogen solubility in this regions, [164].

2.7.3 Hydrogen embrittlement resistance of nickel base alloy 718

Nickel alloy 718 is generally known for its excellent resistance to environmentally assisted cracking EAC in sea water with cathodic protection in the potential range from -1000 to -100 mV, [128]. Nevertheless, solution treated and single aged material with the hardness values exceeding 40 HRC revealed a certain HE susceptibility, based on evidence of laboratory SSR testing and field experience, [128]. A number of fractographic analysis reports on samples, failed due to the HE, state visual evidence for the hydrogen promotion of the planar slip of dislocations in the nickel alloy 718, [48], [125], [165]. Mechanical properties of the material in hydrogen are believed to be strongly linked to the deformation modes, [129]. Hicks and Alstetter suggested that the observed preferential crack propagation on the {111} planes might be an indicator for a further fracture mechanisms rather than solely the plasticity phenomenon, [166]. The formation of the dislocation slip bands in nickel alloy 718 could be attributed to the low stacking fault energy [167], resulting in inhomogeneous deformation in contrast to the deformation of loosely shaped dislocation segments, [48]. Considering the large impact of the secondary phase precipitations (such as $\gamma' + \gamma''$ and δ) on the mechanical properties of the material, some of the research work was dedicated to the possible correlation between their morphology and HE susceptibility, [28], [80], [87], [168], [169]. The material performance in the presence of hydrogen demonstrated a strong correlation to the choice of the aging procedure. However, the drown conclusions are controversial. The majority of the experimental studies stated the detrimental effect of δ precipitations on the HE resistance of 718 (manifested by the enlargement of the notch tensile strength loss [83] and significant loss of ductility [28]). In

contrast, Kagay et al. [125] did not observe any significant deleterious effect of the orthorhombic phases. Some literature reports also suggest $\gamma' + \gamma''$ precipitations to reduce the HE resistance of 718, [170], [171]. The disagreement of the experimental observations might result from the differences of both material microstructures and applied testing approaches. In addition interdependent processes of the $\gamma' + \gamma''$ and δ nucleation could handicap the accurate interpretation of the obtained results. Taking into account the incoherency of the carbide precipitations, the carbide/matrix interface is believed to be preferential site for the crack nucleation as a result of decohesion mechanism. Indeed, fractographic analysis on the cross sections of the hydrogenated specimens of alloy 718 aged at 780 °C, revealed debonding along the carbide/matrix interface, [167]. However, this hypothesis was not confirmed by Moody et al. who did not evidenced any correlation of the carbides with the crack propagation path in the hydrogenated specimens, [166].

As shown above, despite the overall good corrosion and HE resistance of nickel alloy 718, some of the authors report the observed material susceptibility to SSC and SCC which might be traced back to the possible negative impact of secondary phase precipitates (such as Laves, δ-phases or carbides) as they are believed to represent the sites of local passive film interruption. At the same time, the published results on the HE susceptibility of alloy 718 reveal a certain correlation between the material performance and its microstructure.

2.8 Summary

Steadily growing energy demand combined with the nearly full exploitation of the relatively shallow wells pushes the oil and gas industry into drilling deep and ultra deep wells. As a result, drilling equipment has to maintain an excellent performance under complex mechanical loads in extremely severe service conditions, such as high pressure and temperature combined with highly corrosive environments containing sour gases and/or elementary sulfur. Due to the combination of excellent mechanical properties, outstanding corrosion resistance and good welding characteristics, nickel base superalloy 718 has been one of the most frequent choices for oil and gas applications.

Although excellent performance of superalloy 718 has been confirmed by a great number of laboratory studies, [51], [172], several field failures of this material has been reported, [48], [173]. Large body of research on the susceptibility of nickel alloy 718 has been conducted during the last twenty years indicates hydrogen embrittlement as a main damage mechanism supporting the material degradation, [83], [167], [174]. Nevertheless, the wide scattering in the material chemical composition used in the study and discrepancies in testing conditions handicap the interpretation of the experimental results.

Both mechanical and corrosion properties of the superalloy 718 are believed to be strongly linked to the material microstructure. Intermetallic inclusions, such as secondary phase

precipitates δ, γ' and γ'' are known for their contribution to the alteration of the deformation mode. Thus, it is evident that the variation of their size and volume fraction would make a significant impact on the material resistance to hydrogen embrittlement. However, the mechanism of the stress corrosion cracking requires the corrosion damage of the protective oxide layer. For understanding the failure mechanism of nickel alloy 718 due to the stress corrosion cracking it is therefore necessary to address the complex system of the damage processes occurring during the material degradation.

3 Research objectives

Stress corrosion cracking resistance of a material depends strongly on the quality of the present oxide layer (material susceptibility to localized corrosion) as well as material resistance to hydrogen induced cracking. In case of alloy 718, both of these characteristics seem to be dependent on the precipitation of the intermetallic phases, such as $\gamma' + \gamma''$, δ, and carbonitrides Ti,Nb(C,N) and hence on the choice of the aging procedure. However, the reports on the correlation between the secondary phase precipitation and material susceptibility to localized corrosion, HE and SCC available in the literature provide with the experimental data, gained on samples with significant differences in material chemical composition, by means of different measurement approaches and under large variation in the testing conditions. The resulting discrepancies in the evaluation statements impede the adequate data interpretation and thus hinder the optimization of the material performance.

The main goal of this work is a systematical study of the correlation between the microstructural peculiarities of alloy 718 and its resistance to localized corrosion and hydrogen embrittlement. To meet this goal, it is necessary to characterize the material microstructure and further on investigate coherences between microstructural peculiarities and material corrosion behavior. In the interest of clarity and simplicity, the overall goal is subdivided into two main scientific issues, which represent two main work packages executed in the course of this thesis, Table 2.

Table 2: Research objectives and related questions

Research objective 1: Characterization of the material microstructure and its properties in regards to the aging procedure
1) Quantification of the δ and $\gamma' + \gamma''$ phase content in regards to the chosen aging procedure
2) Characterization of the local potential distribution in the vicinity of the grain boundary secondary phase precipitations (δ and Ti,Nb(C,N))
3) Characterization of the oxide layers of the different material heats in regards to the chosen age hardening procedure
4) Characterization of the mechanical properties in regards to the chosen aging procedure

Research objective 2: Evaluation of the microstructural impact on the HE and localized corrosion susceptibility of alloy 718
1) Evaluation of the microstructural impact on the localized corrosion resistance of alloy 718
2) Evaluation of the hydrogen diffusivity and solubility in regards to the chosen age hardening procedure
3) Evaluation of the synergistic interactions between the hydrogen dissolved in the microstructure of alloy 718 and the material corrosion resistance in regards to the chosen age hardening procedure
4) Evaluation of the HE susceptibility of alloy 718 in regards to the chosen age hardening procedure

The implementation of the first work package includes the quantitative characterization of the material microstructure in consideration of the given heat treatment procedure. As no alteration of the carbonitrides structure is expected in the targeted temperature window, the quantification is performed solely in regards to $\gamma' + \gamma''$ and δ phase precipitates. Further analysis is devoted to the particular impact of the microstructural alterations on the mechanical properties of the material and on the quality of the protective oxide layers as well. Complementary surface potential distribution measurements are performed in the vicinity of δ precipitates and carbonitrides to clarify their possible contribution to the localized corrosion inducing SCC or HE.

The primary focus of the second work package is on the evaluation of the microstructural impact of alloy 718 on its susceptibility to SCC and HE. Of the particular importance is the knowledge about the processes of hydrogen solubility and diffusivity, mechanisms of hydrogen induced material degradation, electrochemical dissolution of the protective oxide layers and possible synergies between them.

4 Applied techniques and methods of examinations

4.1 Examination of the corrosion behavior

4.1.1 Potentiodynamic scan measurements

The impact of δ phase content on the material pitting susceptibility was investigated by means of electrochemical potentiodynamic approach. Conventional three-electrode-system connected to the potentiostat PGU-10V-1A-IMP-S was used for the measurements, Figure 17. Platinum (wire net with the area size of 30x30 mm) and hydrogen electrodes were applied as a counter and reference electrodes respectively.

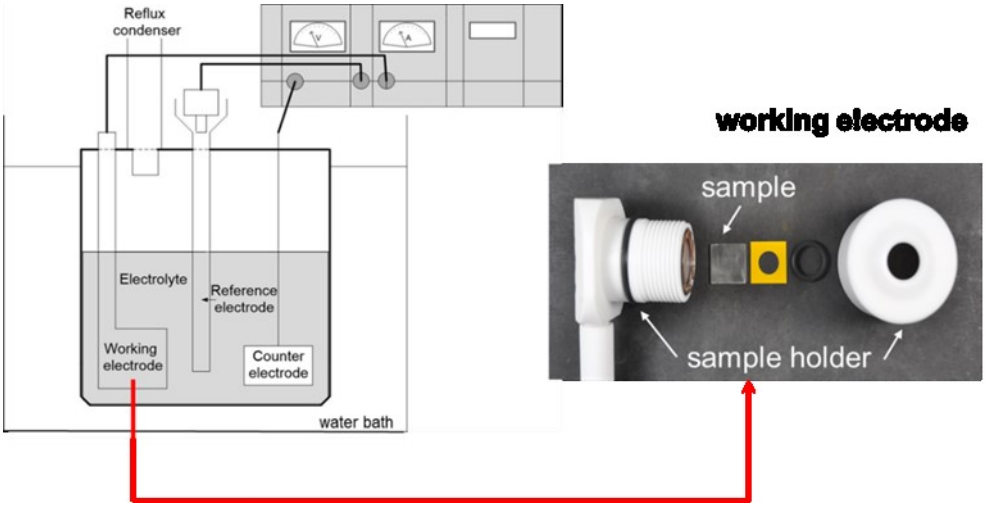

Figure 17: Experimental setup for the electrochemical potentiodynamic measurements, adopted from [175]

Flat square coupons (18.0 x 18.0 x 3.5 mm) were used for the experiments in this work package. All of them were wet grinded with 600 grit SiC paper prior to the experiments and then cleaned in ultrasonic bath with ethanol for 10 minutes and dried via airflow. Nitrogen flushing of the testing electrolyte was carried out for 30 minutes before the beginning of the test to remove oxygen from the testing chamber. The influence of crevice corrosion on the measurement results was prevented by a thin adhesive masking tape with a circle opening ($\varnothing$=10 mm) applied on the sample surface, Figure 17. Electrolyte temperature was controlled by immersing the glass electrochemical cell into the water bath. During the experiment, the measurement cell was covered with a lid equipped with a reflux condenser.

During the measurement samples were polarized with the given scan rate in the potential range from -100 mV_{OCP} (versus open circuit potential) to 1200 mV_H forth resulting in the change of the current density response which was recorded. The initial potential value was

taken in reference to the open circuit potential of the sample measured prior to the experiment for 30 minutes. The evaluation of the material pitting susceptibility was performed by comparison of pitting potential values (measured potential at anodic current density of 100 μA/cm^2) which were determined from three repeatedly conducted experiments.

4.1.2 Open circuit potential measurements

Long time measurements of open circuit potential were performed in order to identify the initiation sites for the local corrosion attack. The experiments were conducted in sodium chloride solution (21 wt.-%) acidified to the pH=2.3 with hydrochloric acid at 90°C to obtain the most differentiable material behavior. The choice of the testing electrolyte was made based on the results obtained from the potentiodynamic scan tests described in the previous chapter (4.1.1). Samples geometry, preparation procedure and experimental setup were kept the same as described in chapter 4.1.1. The evaluation of the material performance was done via analysis of the time dependent open circuit potential curves recorded for each material.

4.1.3 Electrochemical Impedance Spectroscopy

Synergistic effects of hydrogen on the protective characteristics of passive layer were investigated via electrochemical impedance spectroscopy (EIS) measurements. Flat square coupons (18.0 x 18.0 x 1.0 mm) were used in this study. The reduction of the sample thickness (compared to those used in chapter 4.1.1) was necessary for the efficient hydrogen charging. Prior to the experiments all the samples were cleaned in ethanol in ultrasonic bath for 10 minutes and then built it into the same experimental setup as described in chapter 4.1.1. Workstation IM6/6ex by Zahner-Electric was used for the collection of the experimental data. The sample incitation was carried out with the sinusoidal excitation amplitude of 10 mV at open circuit potential, which was recorded for 30 minutes prior to the EIS measurements. Impedance values were obtained at room temperature (25 °C) for the frequency range of 10 mHz to 100 kHz. Sample's ability to passivation was evaluated by means of the polarization resistance (Z at 10^{-2} Hz) measured in three repeated experiments. Series of 7 spectra were recorded for each tested sample for the observation of time-dependent changes in the sample behavior. Sample preparation procedure was the same as the one specified in chapter 4.1.1, except for the SiC paper grid (1200 in this study). The reduction of the sample roughness was aimed to address the question about the hydrogen impact on the material corrosion performance, as the smooth surfaces allow easy monitoring of the nucleation and growth of the small corrosion sites on the sample's surface.

Electrochemical hydrogen charging of the EIS-samples

Hydrogen was introduced into the sample by means of electrochemical cathodic galvanostatic charging (i=30 mA/cm²) for 24 hours at room temperature (25 °C). The choice of ammonium sulfate (1.0 M) acidified to pH=3 (H_2SO_4) with the addition of hydrogen poison (0.01 g/l sodium sulfate) for the charging electrolyte, provided a sufficient hydrogen entry during charging procedure. Continuous circulation of the electrolyte in the charging chamber ensured the removal of the hydrogen bubbles from the sample surface and ensured constant conditions throughout the charging procedure. Only one side of the sample was subjected to the hydrogen development (side A), whereas the opposite side (B) remained exposed to the air, Figure 18.

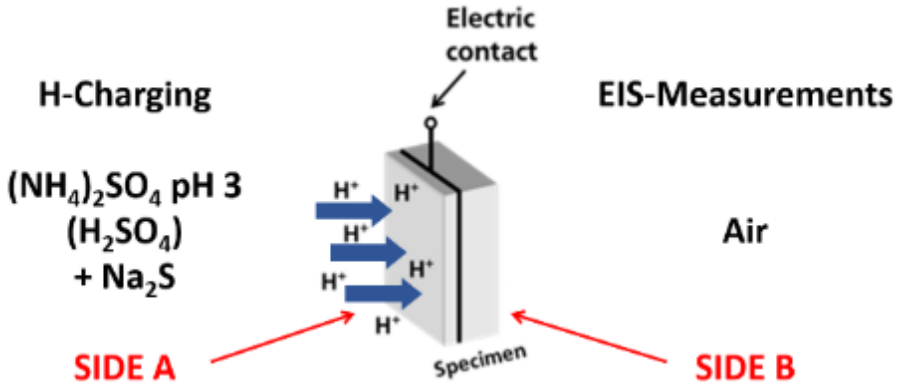

Figure 18: Schematic illustration of the process of hydrogen introduction into the sample

EIS measurement of the hydrogen charged specimens were performed on the side “B” of the specimen. Right after the charging process, this side was shortly grinded with 1200 SiC paper, cleaned with ethanol in ultrasonic bath for 30 seconds and immediately built into the experimental setup for the investigation. In so doing it could be ensured that the obtained measurements would demonstrate the passivation performance of the material and its potential alteration due to the presence of hydrogen.

4.1.4 Scanning Kelvin Probe Force Microscopy (KPFM) measurements

Local contact potential distribution in the vicinity of the carbonitrides Ti,Nb(C,N) and δ phase was investigated by means of scanning kelvin probe force microscopy (SKPFM). The measurements were conducted via Dimension Icon FS measuring device equipped with ScanAsyst software. The cantilever type SCM-PITW and 240 TS coated with platinum-irridium coating (PtIr) on the front and back sides was applied at resonance frequency range of 50 to 100 kHz at a constant force of 1 to 5 N/m. Preliminary to the experiments, samples were wet grinded to obtain a smooth surface finish (arithmetic average surface roughness

of R_a=0.01±0.001 μm) and cleaned in ultrasonic bath in acetone for 10 minutes.

4.2 Examination of the hydrogen diffusivity and solubility

4.2.1 Hydrogen permeation measurements

Electrochemical permeation measurements were conducted to obtain the effective hydrogen diffusion coefficients of the chosen material heats. Samples with different microstructures were tested at the identical conditions to investigate the microstructural impact, such as grain boundaries and secondary phase precipitations on hydrogen diffusion coefficients.

Experimental setup used for this purpose is similar to the one introduced by Devanathan and Stachursky, [176]. A sketch of the experimental setup is presented in Figure 19.

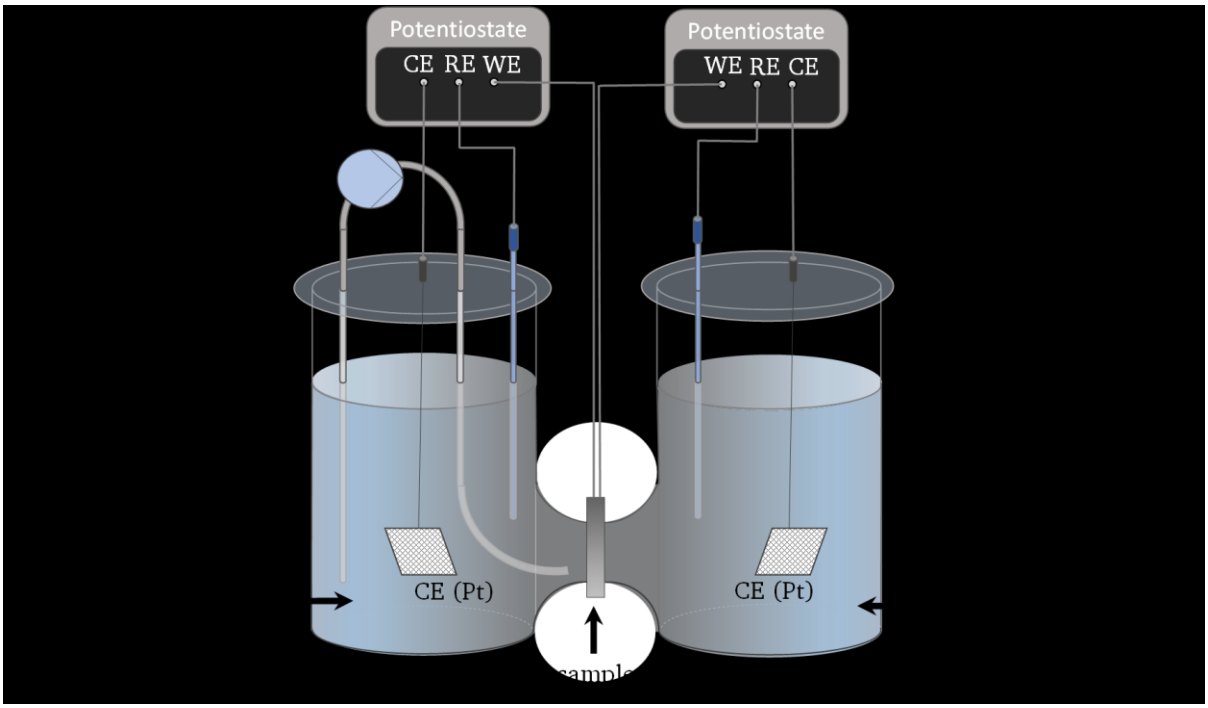

Figure 19: Electrochemical permeation cell, adopted from [177]

Two glass chambers filled with 0.1 M sodium hydroxide (NaOH) solution were separated from each other by the thin flat material coupon (18 x 18 x 01 mm). Electrochemical permeation experiments were conducted at room temperature (25 °C), enabling the correlation to the tensile tests under simultaneous hydrogen charging, see chapter 4.3. Thin palladium coating (10 μm) was deposited on the exit side of the sample (oxidation cell) to enable a stable detection signal, [139], [140]. Prior to that preparation step both sides of the sample were polished to obtain the surface roughness values of R_a=0.01±0.001 μm. After that the one-side coated samples were ultrasonically cleaned in ethanol for 10

minutes, dried in air and built into the experimental equipment presented in Figure 19. Constant cathodic charging current density (100 mA/cm²) was applied to the entry side of the sample (reduction cell) via the potentiostat PGU-10V-1A-IMP-S for the hydrogen evolution. The chosen charging current density appears to be higher than the ones reported in the literature, [178], [179] to compensate for the absence of the hydrogen promoting substances in the testing electrolyte, as it was not possible to use it under the testing conditions due to its harmful poisonous effect. Continuous medium flow generated by the pump (500 ml/min) allowed removing the hydrogen bubbles from the sample surface for the homogeneous charging conditions over the whole experiment duration. Hydrogen outgassing from the exit side of the sample was detected by means of permeation transient current density, measured via grounded potentiostat IM6/6ex Zahner-Electric. For this purpose, sample was polarized to the constant anodic potential (+300 mV_{SCE}) throughout the experiment. The evaluation of the microstructural impact on the hydrogen permeability was done by means of the effective diffusion coefficients values, which were derived from the measured permeation transients via time lag method from five different measurements for each material heat according to (12).

4.2.2 Hydrogen solubility measurements

Microstructural impact on the hydrogen solubility was measured via gas fusion analysis principle. For the analysis hydrogen was introduced into the samples by means of galvanostatic cathodic charging (i=30 mA/cm²) for the constant duration of 24 hours, which is comparable to the charging procedure applied by other researchers, [57]. Due to the spatial limitations of the measurement device, 6mm cubes were used as a sample geometry in this experiment. Ammonium sulfate solution (500 ml 1.0 M $(NH_4)_2SO_4$) acidified to pH=3 (0.5 H_2SO_4) was poisoned by addition of sodium sulfide (0.01 M Na_2S) for the sufficient hydrogen entry. A set of five samples could be charged in one charging procedure, using the developed unit demonstrated in Figure 20. Similar to the previously described approach (see chapter 4.2.1) hydrogen bubbles were removed from the sample surfaces by the circulating electrolyte (500 ml/min).

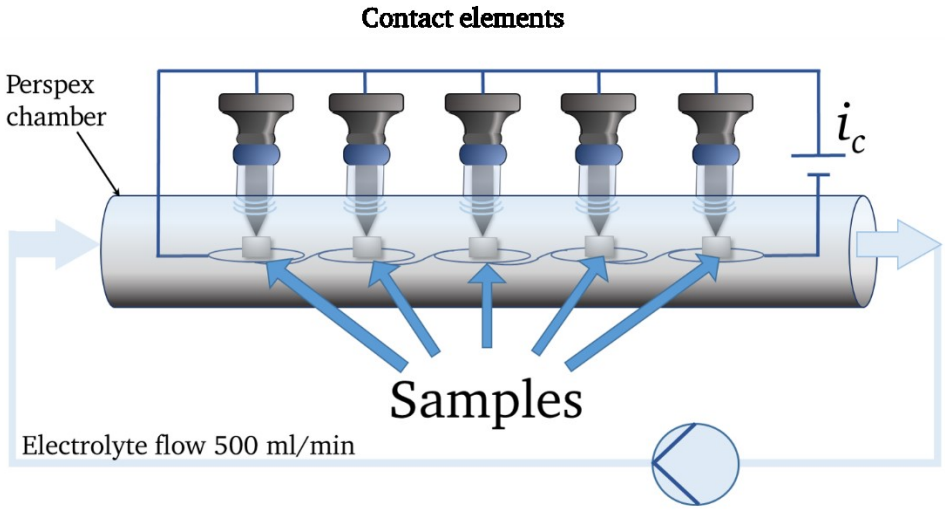

Figure 20: Schematic experimental setup for the cathodic hydrogen charging of samples

After the charging, samples were immediately removed from the unit, rinsed with deionized water, and immersed into the liquid nitrogen (-200 °C) for storage to prevent any hydrogen emission. This allowed performing the hydrogen content measurements at the exact same testing conditions for all samples.

The total amount of hydrogen, absorbed by the samples during 24 hours of charging at 30 mA/cm² current density, was released from the samples, as they were melted at 1500 °C for 150 seconds, and then carried to the quadrupole mass spectrometer type ESD 100 manufactured by InProcess Instruments (IPI) with the nitrogen flow for quantification. The obtained values of hydrogen content are referred to the sample mass, measured by weighting immediately before the experiment. A total number of ten samples were melted for each material variant to gain the statistically secured data for the analysis.

4.2.3 Hydrogen visualization via silver-decoration technique

Spatial hydrogen distribution in the exemplary tensile samples tensioned under displacement control and in-situ cathodic hydrogen charging was investigated via silver (Ag)-decoration technique, [180]. The intention for this experimental study was to complement the results of the slow tensile test under simultaneous cathodic charging which are described in chapter 4.3. For this purpose the tensile test under simultaneous cathodic hydrogen charging was interrupted before the sample fraction without any relieve. The testing electrolyte was then removed from the chamber and replaced by 4.3 mM potassium silver cyanide solution. After that the sample was tensioned to failure at the same displacement rate and the fracture surfaces were exposed to the solution for the further 20 minutes. The silver ions presented in the electrolyte solution take part on the oxidation

reaction with hydrogen emitting the sample-solution interface according to (13).

$$Ag^{+} + H \rightarrow Ag \downarrow + H^{+} \tag{13}$$

As a result of this reaction, silver ions are reduced by absorbed hydrogen and will precipitate on the metal surface.

The samples were then removed from the chamber, rinsed with deionized water and dried in air for the subsequent SEM and EDX examination. Areas of silver deposition evidenced via EDX were used to make conclusions about the hydrogen presence in the sample's cross section.

4.3 Examination of hydrogen embrittlement via slow tensile tests under simultaneous cathodic hydrogen charging

For the investigation of the effect of the size and amount of precipitates in alloy 718, slow tensile tests under displacement control (0.2 and 0.02 mm·h^{-1}) were performed under continuous cathodic charging conditions. The chosen displacement rates are supposed to approximately match the strain rates of 10^{-4} and 10^{-6} s^{-1}, recommended for the testing of HE under corrosive environments in NACE TM 0177 specification, [181]. The tests were performed in 1.0 M $(NH_4)_2SO_4$ solution having pH 3 (H_2SO_4) at room temperature (25 °C) under a constant cathodic current density of 30 mA/cm^2. For this purpose, round tensile sample with the circular notch in the shaft area (notch factor $\alpha_K = 4.2$) presented in Figure 21 was installed into a chamber equipped with the three-electrode system and connected to potentiostat Gamry (Ref600), Figure 22.

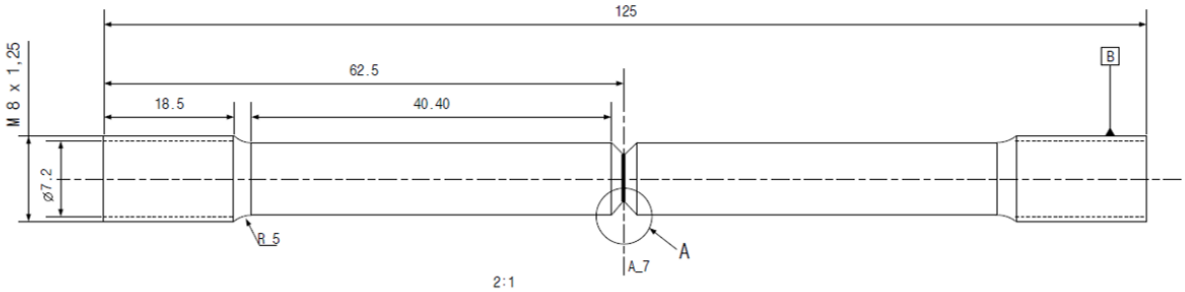

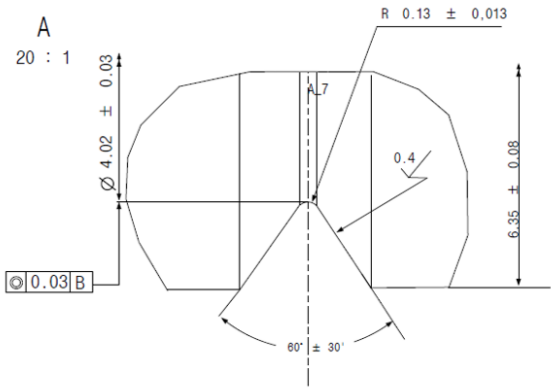

Figure 21: Sample geometry for the slow tensile tests under simultaneous hydrogen charging

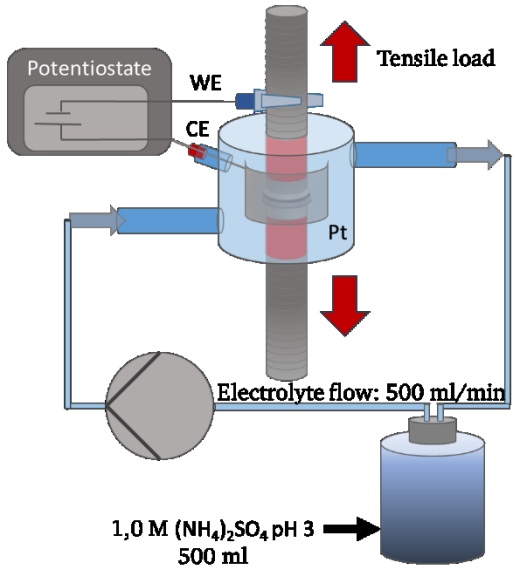

Figure 22: Experimental setup for the slow tensile tests under simultaneous cathodic hydrogen charging

Hydrogen bubbles, formed at the sample surface due to recombination, were removed from the surface via electrolyte flow (500 ml/min). The tests under simultaneous hydrogen charging in acidified ammonium sulphate solution were performed for each material variant by triplicate. Ratios of elongation at fracture (l) obtained from these experiments were taken to the reference values for the samples tested on air to determine the material susceptibility to HE.

HE susceptibility of superalloy 718 was evaluated in regards to the aging condition by comparing the value of HE coefficient (**HE**) calculated according to (14), [182]:

$$\boldsymbol{HE}\ (\%) = \left(1 - \frac{l_H}{l_A}\right) \cdot 100\% \qquad (14)$$

With l_H – elongation of the hydrogenated sample, and l_A – elongation of the sample tested on air, determined as an average value of three tests.

4.4 Complementary examinations

To reveal the correlation between the aging-dependent microstructural peculiarities and material performance in corrosion and hydrogen embrittlement experiments, the measurements described in chapters 4.1 - 4.3 were complemented with pre- and follow-up examinations of the tested samples. Documentation of the sample roughness before and after the corrosion tests (EIS-measurements) allowed to quantify the extent of the corrosion attack and establish its correlation to the chosen aging procedure. EDX-measurements performed on exemplary corrosion sites enabled the identification of the preferential sites of corrosion attack enabled the identification of the preferential sites for corrosion attack. Measurements of the oxide layers composition performed via X-Ray photoelectron spectroscopy (XPS) also contributed to the understanding of the conjunctions between the aging procedure and corrosion damage mechanism.

Scanning electron microscopy (SEM) observations of the fracture surfaces of the tensile samples tested in air and under simultaneous cathodic hydrogen charging provided support for the interpretation of the results of slow tensile tests aimed for hydrogen embrittlement susceptibility examination.

5 Sample preparation and characterisation

To address the questions stated in chapter 3, several material heats with differences in the microstructure were produced and thoroughly characterized. Following chapter gives an overview of the chosen approaches for the sample elaboration as well as the results of the material examinations.

5.1 Chemical composition, aging procedures and sample elaboration

All samples were elaborated from the same heat, produced by vacuum induction melting (VIM) and subsequently remelted by vacuum arc remelting (VAR). The produced ingot was forged to 25.4 cm bars (forging ration ≥4). The material was delivered in the solution annealing (SA) stage, which was performed for 1 hour at 1032 °C with subsequent water quenching.

5.1.1 Chemical composition

Chemical composition of the material was thoroughly controlled according to the limits of API 6CRA - 2016. Analysis of the chemical elements was performed by means of glow-discharge spectrometer (GD-OES), Table 3.

Table 3: Alloy composition

	Chemical composition (mass %)							
	Ni	**Cr**	**Fe**	**Nb+Ta**	**Mo**	**Ti**	**Al**	**C**
API 6ACRA	50.00-55.00	17.00-21.00	bal.	4.87-5.20	2.8-3.0	0.80-1.15	0.4-0.6	max. 0.045
Investigated material	53.68	18.61	17.03	5.14	3.1	0.99	0.59	0.024

5.1.2 Aging procedure

After the solution annealing, the samples were age hardened to obtain microstructures with various amounts and sizes of γ'/γ'' and δ-phase precipitations. An overview of the heat treatment variations investigated within the framework of this research is given in Table 4.

Table 4: Variation of heat treatment and typical hardness of the alloy 718

Material variant	Solution annealing	Age hardening	Measured hardness HRC
720+620	1032 + WQ	720 °C / 8h / air & 620 °C / 8h / air	42-44
760	1032 + WQ	760 °C / 8h / air	40-42
775	1032 + WQ	775 °C / 8h / air	36-38
800	1032 + WQ	800 °C / 8h / air	34-36
870	1032 + WQ	870 °C / 8h / air	21-22
720-4	1032 + WQ	720 °C / 4h / air	32-35
720-8	1032 + WQ	720 °C / 8h / air	39-42
750-8	1032 + WQ	750 °C / 8h / air	40-41
800-24	1032 + WQ	800 °C / 2h / air	35-38
1032	1032 + WQ	-	Not measured
1050	1050 + WQ	-	Not measured
1090	1090 + WQ	-	Not measured

5.1.3 Samples preparation

All specimens were eroded from the transitional zone of the material bar (about 20 mm from the edge). This allowed to avoid any undesirable effects of segregation of the alloying elements. The elaboration was carried out in two steps. First material blocks of a suitable size were eroded from the transitional zone of the annealed material rod for the subsequent aging. After the heat treatment, the samples of the desired geometries were elaborated. By doing so, the scale layers, formed on the material surface during the aging could be mechanically removed. Moreover, all the samples featured the same surface roughness of Rz=1.3 μm.

5.2 Metallographic examination

Metallographic examination of the material heats was performed to document the changes in the material microstructure, caused by differences in age hardening procedures.

5.2.1 Light microscopy

Light microscopy observations of the etched samples revealed an austenitic structure for all the tested heats. Standard etching procedure for nickel base alloy 718 (V2A at 30 °C for ca. 30 sec) was used to prepare the metallographic sections. The variation of the temperature for the solution annealing procedure resulted in the grain coarsening, which was ascertained via the grain size measurements performed according to ASTM E112, [21]. As was expected, the grain size of the aged samples remained constant (ASTM 4 to 5) which is the same as the grain size of the solution annealed material prior to the heat treatment procedure, Figure 63 (annex). It is noteworthy to mention that no significant differences regarding the morphology of the γ'/γ'' and δ phase precipitations could be recognized from these micrographs. Similarly to that, the spatial ratio of carbonitrides was not influenced by the aging treatment, as it was established on comparative measurements performed via thresholding image processing approach [183] on samples 760 and 870, Figure 23. The large difference in the aging temperature between these two heats allows to assume them to be representative for addressing the abovementioned question. The corresponding light micrographs can be found in annex in Figure 61 and Figure 62.

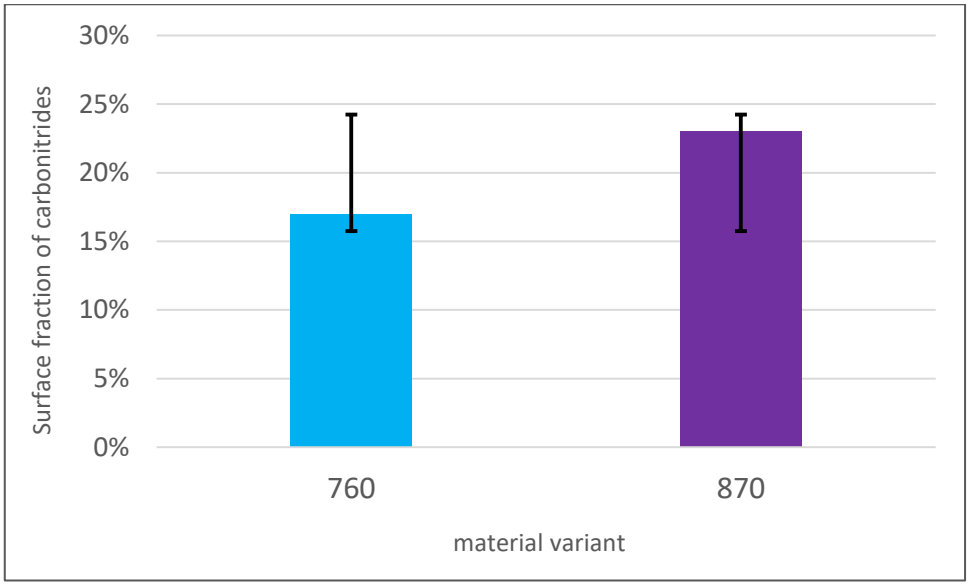

Figure 23: Influence of aging procedure on the surface fraction of carbonitrides

In contrast, an increase in the annealing temperature led to the grain growth as it can be

seen in Table 5.

Table 5 Grain size variation of the alloy 718

Material variant	Grain size according to ASTM E112 [21]	Average grain size in μm
1032 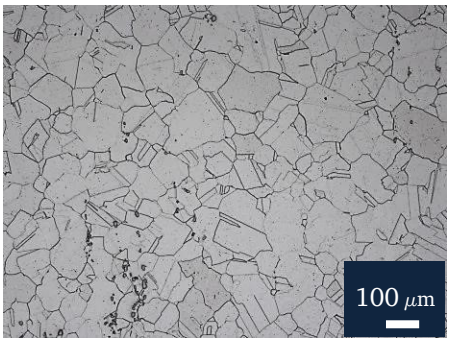	4-5	50-80
1050 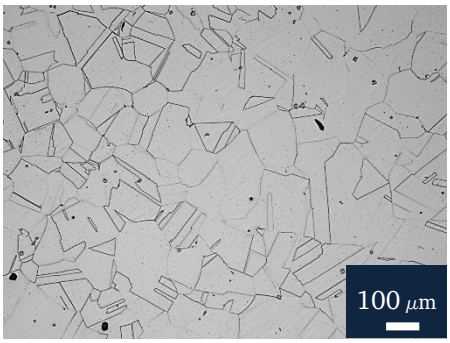	3	110
1090 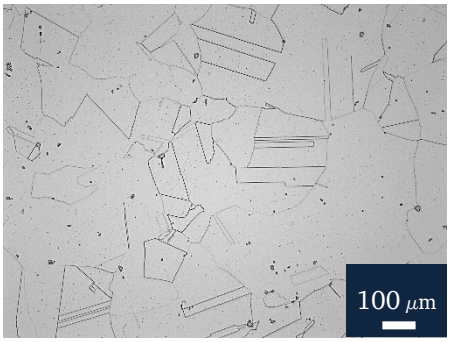	0-1	220-320

5.2.2 SEM examination

As expected, the variation of the temperature for the age hardening resulted in significant differences in the samples microstructure, which were documented by means of scanning electron microscopy (SEM) and transmission electron microscopy (TEM). In addition to

the microstructure documentation, analysis of some microstructural peculiarities were performed by means of energy dispersive X-Ray (EDX). The results of the EDX-examination can be found in the annex, (Figure 64, Figure 65, Table 11, and Table 12). Based on this examination, it was possible to identify some of the precipitations with typical appearance as titanium- and niobium carbonitrides, γ'/γ'' and δ phase precipitations as well. Both γ'/γ'' and δ phase precipitates were observed in all the age hardened samples, Figure 24.

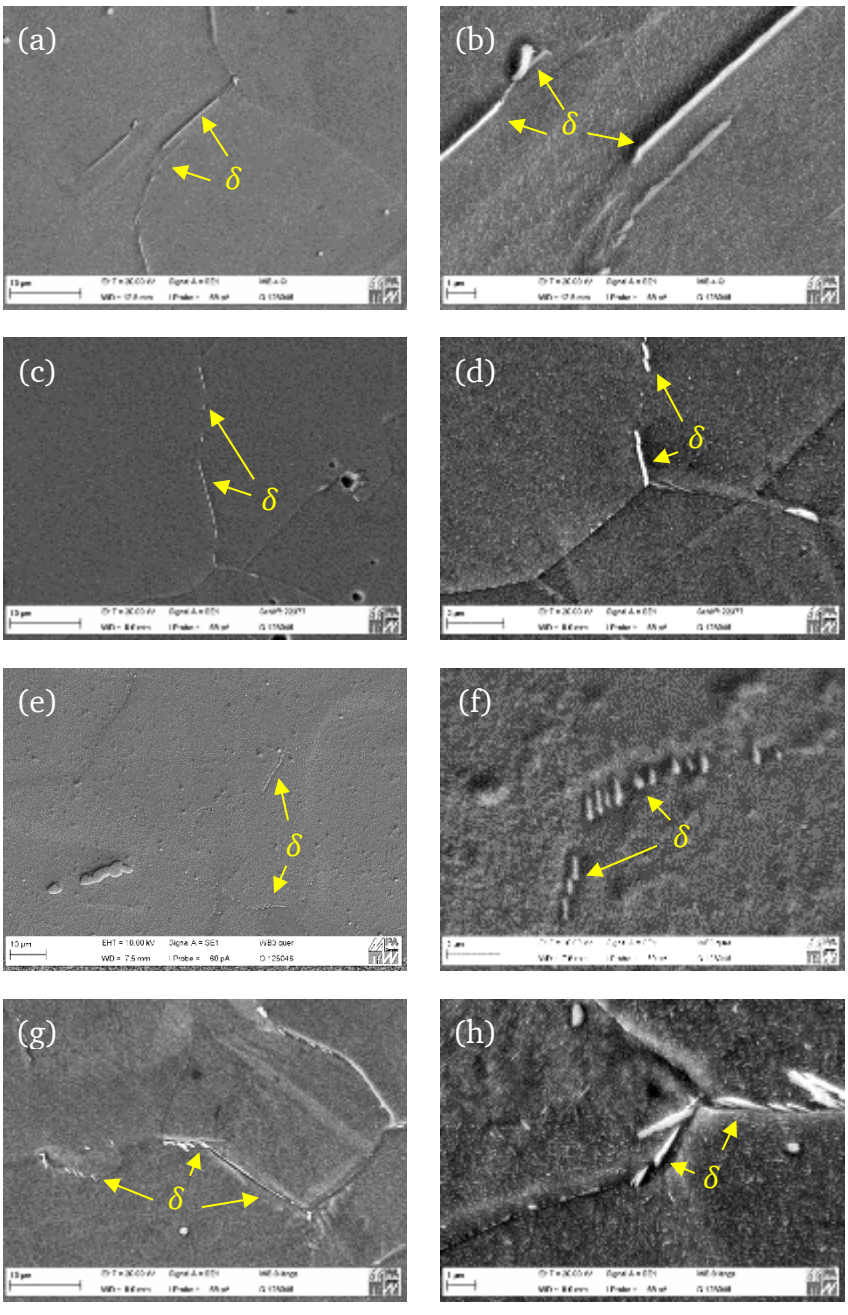

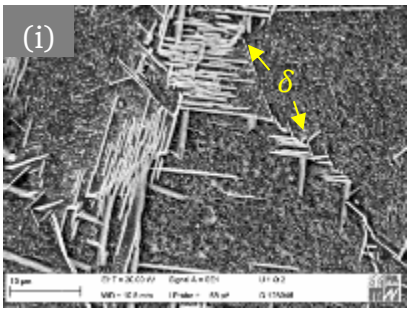

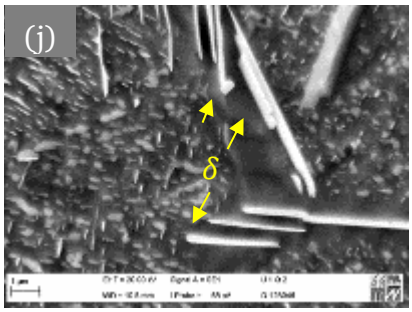

870

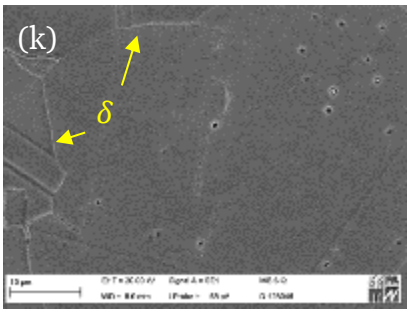

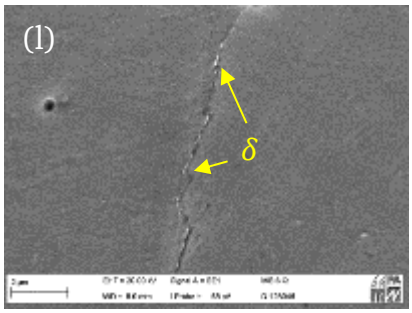

720-4

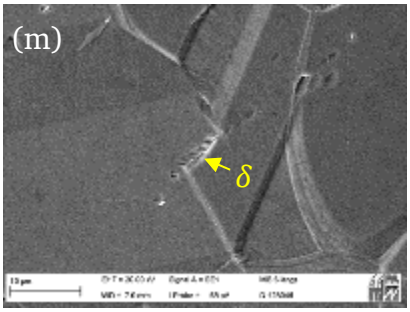

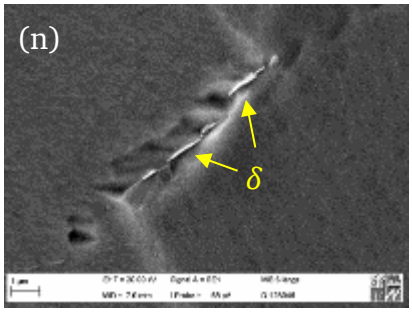

720-8

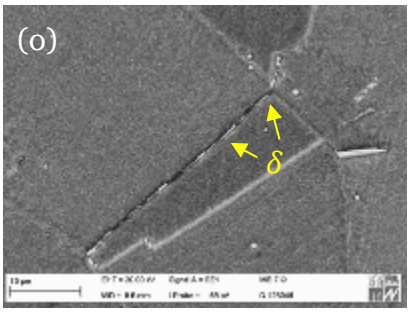

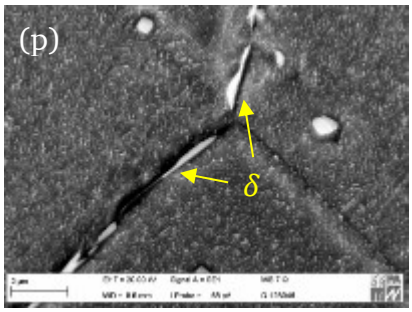

750-8

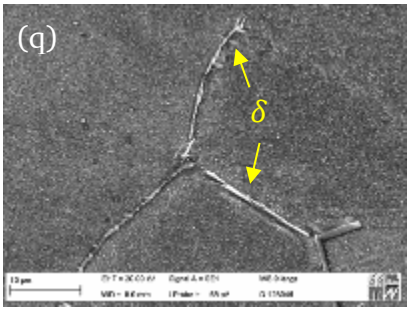

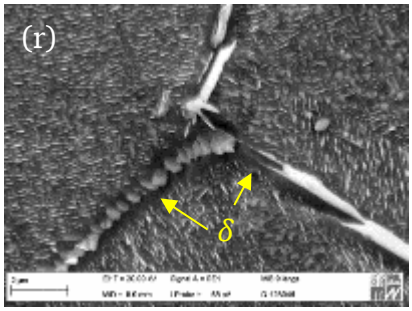

800-24

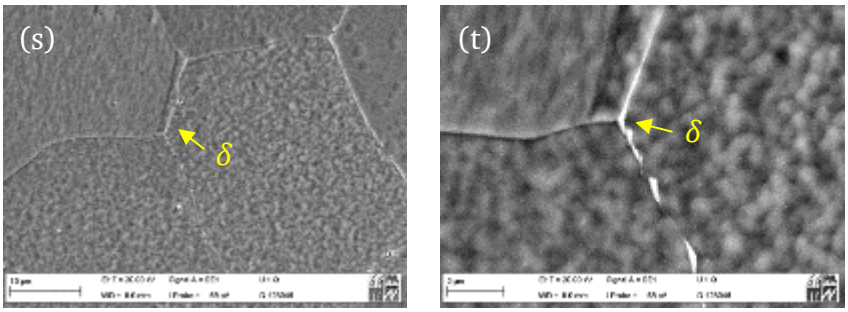

Figure 24: SEM micrographs of age hardened alloy 718

As expected, no globular δ phases were observed in any of the samples. On the other hand, acicular δ precipitates were evidenced on the occasional grain boundaries of all the material heats. The increase of the age hardening temperature resulted in the higher amount of δ precipitates at the grain boundaries. In the case of the overaged material (870) they were identified within the grains. Micrographs of the δ precipitations made with higher magnification revealed zones free from γ'/γ'' phases, occurring as a result of the niobium depletion from the matrix due to the δ formation, Figure 24-f, h, j, p, and r. Although the solution annealing temperature (1032°C) is above the solvus temperature of the δ precipitates, few of them were spotted on occasional grain boundaries of the solution annealed material 1032, Figure 24-s and Figure 24-t. This can be explained by the inhomogeneous cooling of the material ingot during water quenching. As a result, the cooling rate in the transitional zone is slower than on the surface of ingot and the precipitation of the δ can take place. Accordingly, few grain boundary δ phases were also observed in material variants 720-4, 720-8, and 720+620, even though the aging temperature is far below its nucleation temperature.

5.2.3 TEM examination

SEM micrographs discussed in the previous chapter reveal the evolution of γ'/γ'' precipitations regarding the chosen temperature for the age hardening. Prior to the examination samples were mechanically thinned down to the thickness of 100 μm and then punched to obtain slices with 3 mm in diameter. To complete the sample preparation, the middle of each slice was electrolytically thinned down to provide for electron-transparent thickness on the edge of the hole, formed during the last procedure. As was expected, TEM observations revealed the coarsening of the precipitates along with the increasing temperature, Figure 25.

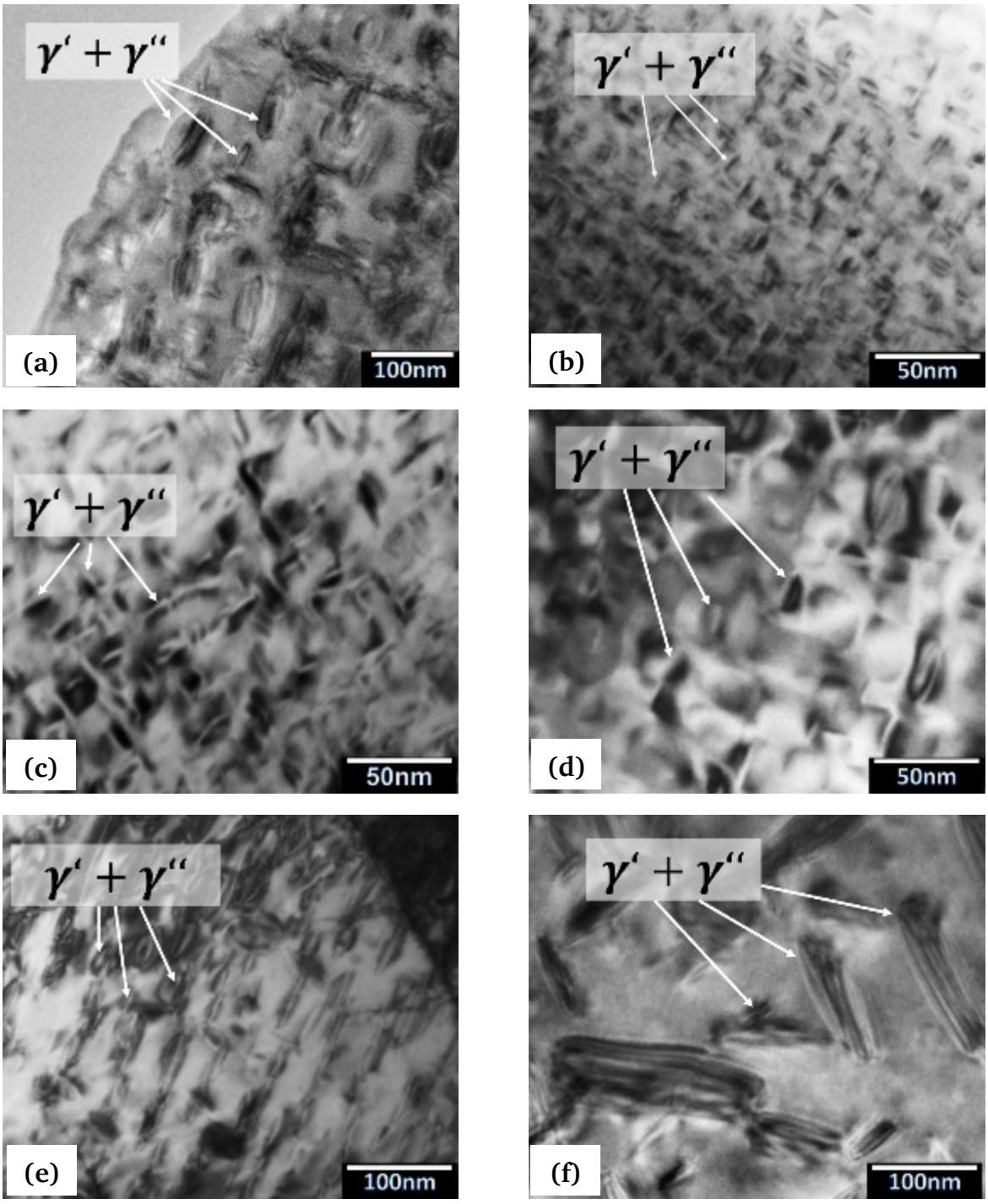

Figure 25: TEM micrographs of the transformation of $\gamma' + \gamma''$ phases in regards to the aging temperature in material variants (a) 720+620; (b) 720-4; (c) 720-8; (d) 750-8; (e) 800-8; (f) 800-24

In order to quantify the microstructure evolution, the size and fraction of the $\gamma' + \gamma''$ particles was determined for several material variants by means of image analysis via the Datinf Measure software. For that purpose the mean length and width was measured on a minimum of 50 particles. The results of this analysis are given in Table 6.

Table 6: Qualitative characterisation of the $\gamma' + \gamma''$ precipitates transformation regarding the age hardening temperature

Material variant	Average length, [nm]	Average width, [nm]	Quantity per nm^2
720+620	43.7±13.9	21.3±5.9	$5.7 \cdot 10^{-4} \pm 0.6 \cdot 10^{-4}$
720-4	8.9±3.6	3.6±0.7	$2.4 \cdot 10^{-3} \pm 0.6 \cdot 10^{-3}$
720-8	13.8±5.6	5.6±1.4	$6.7 \cdot 10^{-3} \pm 0.1 \cdot 10^{-3}$
750-8	22.7±5.7	9.9±2.1	$1.74 \cdot 10^{-3} \pm 0.3 \cdot 10^{-3}$
800-8	56.1±9.7	20.4±3.6	$3.54 \cdot 10^{-4} \pm 0.7 \cdot 10^{-4}$
800-24	95.4±50.8	31.2±10.9	$8.94 \cdot 10^{-5} \pm 0.8 \cdot 10^{-5}$

Both size and fraction are observed to be dependent on the age hardening procedure. Aging at 720 °C for 4 hours resulted in the occurrence of small, very finely dispersed precipitates. An increase in the heat treatment duration (8h at 720 °C) leads to the precipitation coarsening at lower volume fraction, which could be attributed to the precipitation coalescence. Same phenomenon is also observed for the heats aged at 800 °C for 8 and 24 hours respectively. Double step aging (720 °C for 8 hours followed by 620 °C for 8 hours) results in a mixture of very fine and coarse $\gamma' + \gamma''$ precipitates closely packed to each other. The obtained results are in agreement with the data available in literature.

The values presented in Table 6 contain certain inaccuracies, which are caused by one or more of the following reasons:

- Due to the possible co-location of γ' and γ'' precipitates [35], [37], [38] the amount of the precipitates per square unit might be underestimated.
- The distinction between the γ' and γ'' cannot be performed on the basis of optical observations by means of TEM micrographs, since both of them appear very similar to each other, [30].
- The length and width of precipitates were measured on the TEM micrographs under assumption that all the observed particles reside in the plane, which is orthogonal to the detector. However, as it was pointed out by Hattestrand and Andren, a geometrical correction should be carried out, to compensate the proportion of the precipitates, which would intersect the surface and therefore appear less than their actual size, [43]. Yet, since the sample thickness remained unknown, this was not

possible.

Thus, the values from Table 6 may be considered only for the terms of approximate material ranking and shall not be understood as absolute values.

5.2.4 Determination of the δ phase content

To enable a systematic study of the possible influence of the δ phase precipitations on the material performance, δ phase content should be determined in regards to the chosen aging procedure. The chosen experimental approaches and the findings obtained during this examinations are described below.

XRD-Examination

Examination of the aged samples by means of XRD-measurements was carried out to quantify the volume fracture of δ phase precipitates in regards to the choice of the aging temperature. The measurements were performed on Bruker D8 ADVANCE via Cu-radiation with the wavelength of 0.154 nm. Summarized presentation of the obtained spectra is given in Figure 26-a.

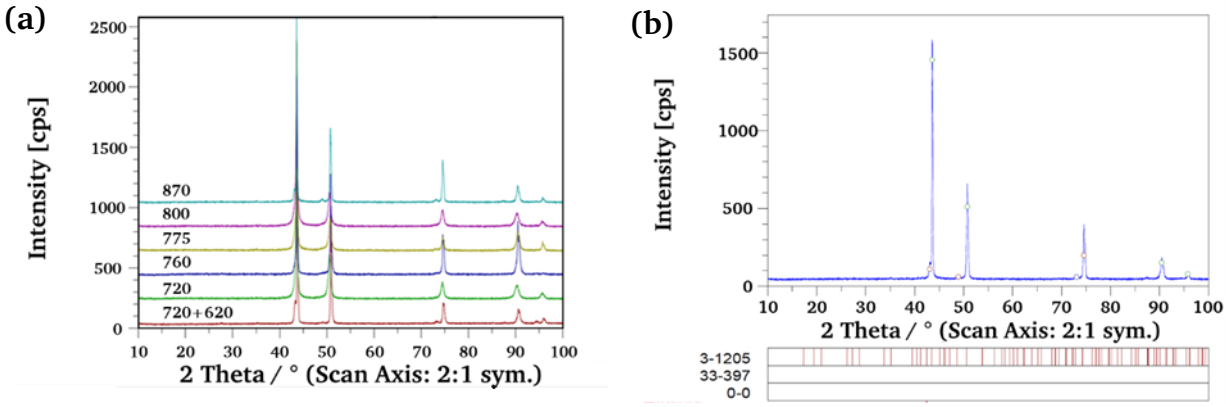

Figure 26: (a) XRD spectra of aged alloy 718; (b) XRD spectrum of material variant 870

The obtained spectra indicated strong peaks corresponding to the face cubic centered (fcc)

lattice structure with differences in the lattice constants, Table 7.

Table 7: Lattice constant of γ matrix in regards to the heat treatment

Material variant	720+620	720	760	775	800	870
a (nm)	0.36241	0.35998	0.35928	0.35971	0.35974	0.36336

Figure 26-b represents the XRD spectrum recorded for the overaged material variant 870. The red lines below the graph indicate the position of the expected peaks corresponding to the orthorhombic crystal structure. Since no consistency between the theoretically calculated and recorded spectra is observed in Figure 26-b, the volume fraction of δ precipitates in the material variant 870 should be less than 1% (the resolution limit of the measurement approach). Considering that the material variant 870 contains the highest amount of δ phase, any possibility to quantify the δ phase content of the rest of the material variants using XRD-measurements can be ruled out.

Quantification of the delta phase content by means of stereological method

To quantify the content of δ phase, aged samples of alloy 718 were analyzed by means of BackScatter Electron (BSE) microscopy, [177]. For this purpose, images of the sample surface were taken with 2000-x magnification, Figure 66. Total length of the grain boundaries within the micrograph was estimated using the photo-processing program "Datinf Measure". The content of δ precipitates DELTA was then estimated as an average ratio of the number of the precipitates per unit of grain boundary length, measured on three different sites according to the equation (14). Because the measurement only involved counting, it was not sensitive to image resolution.

$$\mathrm{DELTA} = \frac{1}{3}\sum_{i=1}^{3}\frac{(total\ number\ of\ \delta\ precipitates)_i}{(total\ grain\ boundary\ length)_i} \tag{14}$$

Since no correlation between the size of the observed δ precipitations and the temperature for the age hardening was observed during SEM analysis of the sample surfaces, the obtained ratio appears to be a plausible value to rank material heats in terms of the extent of the grain boundary decoration with δ phases. The obtained values for the estimated δ

phase content are presented in the diagram in Figure 27. When compared to the SEM-micrographs of the samples presented in Figure 24, it can be found that these data are in a good agreement with the empirical impression about the variation of the δ phase amount with the aging temperature.

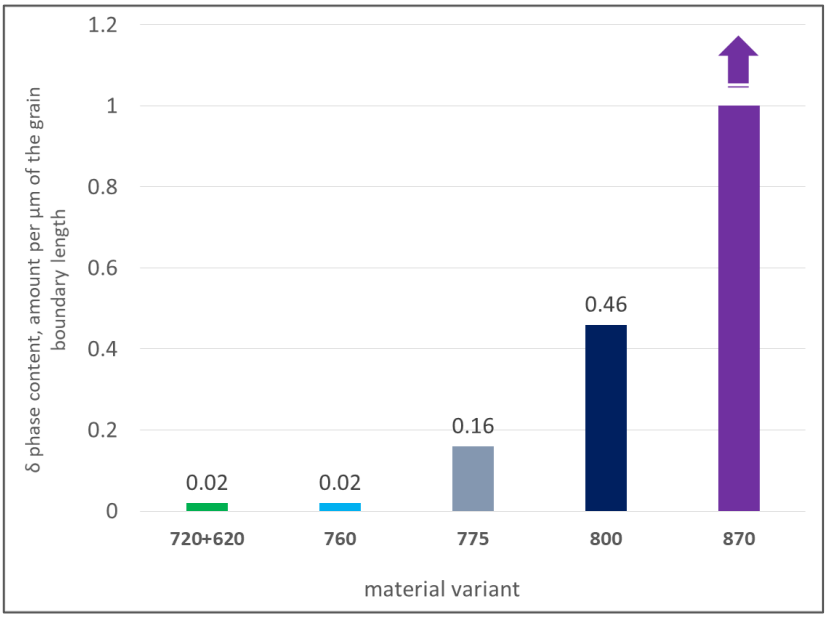

Figure 27: Estimated content of the δ phase precipitations in alloy 718 with regards to the aging temperature

5.3 Oxide layer examination by means of X-Ray photoelectron spectroscopy

Excellent corrosion resistance performance of the superalloy 718 is closely related to the quality of the protective oxide layers built on the material surface. To find out, whether or not the variation of the aging temperature would influence the oxide layer structure samples were investigated by means of X-ray photoelectron spectroscopy (XPS). The measurements were performed on the surface analysis system Physical Electronics PHI 6700 with monochromatized AlK_α-radiation ($h\nu = 1486.6eV$). Prior to the experiments samples were grinded with abrasive SiC paper to the surface finish of 0.5 μm and thoroughly cleaned with acetone in ultrasonic bath (10 min) followed by argon plasma etching (5 min). Two different heats (760 and 870) with presumably the largest difference in the oxide composition were examined. The obtained spectra are presented in the annex, Figure 71. The presence of nickel (Ni), iron (Fe), chromium (Cr), and molybdenum (Mo) in both metallic and oxidized form was verified for each of the material conditions. In contrast, niobium (Nb) was found merely as an oxide. Minor differences in the composition of the oxide layers of the two heats concern the oxidation form of Mo and Nb. Niobium

oxide of the material variant 760 was predominantly measured in its most stable form (Nb(V)) with a little fraction of Nb(II). Whereas material 870 demonstrated the most stable form of molybdenum oxide – Mo(V), but higher fraction in niobium oxide Nb(II). The observed deviations could be attributed to the differences in the distribution of alloying elements, caused by the extent of the secondary phase precipitates (mainly δ phases). The observed differences in the oxide layer composition will be considered during the interpretation of the results of corrosion and hydrogen permeation experiments, since both processes are known to be affected by the presence of the oxide layers on the sample's surface.

5.4 Scanning Kelvin Probe Force Microscopy (SKPFM) measurements

Comparative measurements of the surface potentials were performed on titan- und niobcarbonitride precipitates as well as on the δ phases in order to estimate their hypothetical corrosion activity in regards to the surrounding matrix. The identification of the inclusions was executed by means of EDX-analysis prior to the measurements, Figure 67. The results of the SKPFM measurements (samples height and potential topography) are presented in Figure 27, Figure 29, and Figure 30.

As it was stated in chapter 4.1.4, the measurement principle of the SKPFM technique is based on applying a DC-voltage to compensate the contact potential difference (CPD) between the AFM tip and the sample. In turn, the CPD between the AFM tip and the sample can be defined as the difference in work function Φ between the sample and the tip:

$$V_{CPD} = \frac{\Phi_{sample} - \Phi_{tip}}{e} \tag{14}$$

It is evident from the equation (14) that depending on whether the compensation voltage is applied at the AFM tip or the sample, the contact potential image of the same objects would appear with an inverse contrast. This effect is demonstrated in Figure 28, where the SKPFM measurements of the CPD of the titanium carbonitride was measured with the compensation voltage applied first to the AFM tip (Figure 28 b) and c)) and then to the sample (Figure 28 d) and e)).

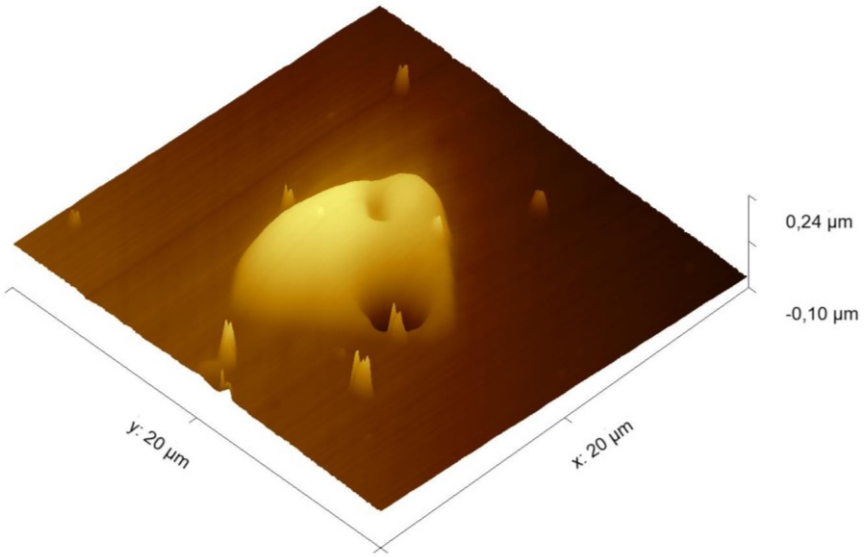

(a)

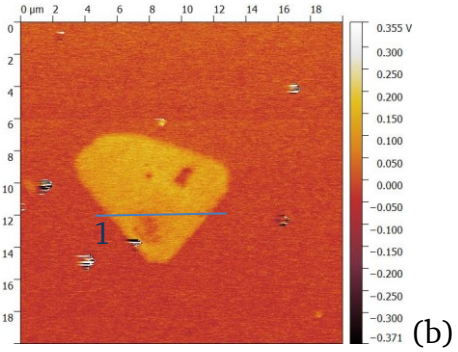

(b)

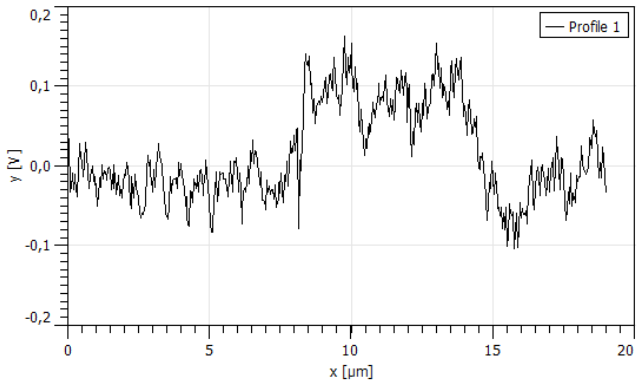

(c)

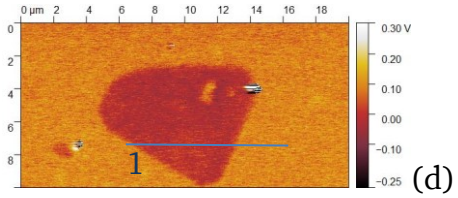

(d)

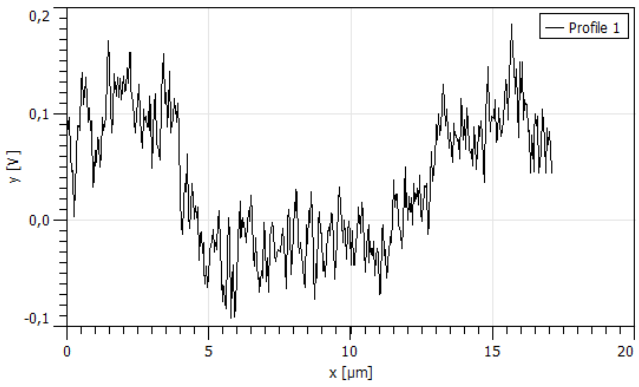

(e)

Figure 28: SKPFM measurements of the potential distribution on the Ti(C,N) inclusion. a) AFM measurement of the topography; b) potential distribution measured with the compensation voltage applied to the AFM tip;c) potential line profile corresponding to the graph b); d) potential distribution measured with the compensation voltage applied to the sample; e) potential line profile corresponding to the graph d)

In both cases the measured work function of the inclusion appears to be higher than the surrounding area. Thus, the titanium carbonitride can be regarded being nobler than the matrix. According to the potential profiles, presented in Figure 28, the difference between the titanium carbonitride and matrix can be amounted up to 150-160 mV.

In contrast, measurements performed on the niobium-carbonitride revealed almost no difference between the Nb(C,N) and matrix, Figure 29 b) and c). However, after the etching of the sample in V2A-etchant, performed for 30 seconds at room temperature (23°C), the difference of 100 mV between the matrix and the niobium inclusion could be successfully measured, Figure 29 d) and e).

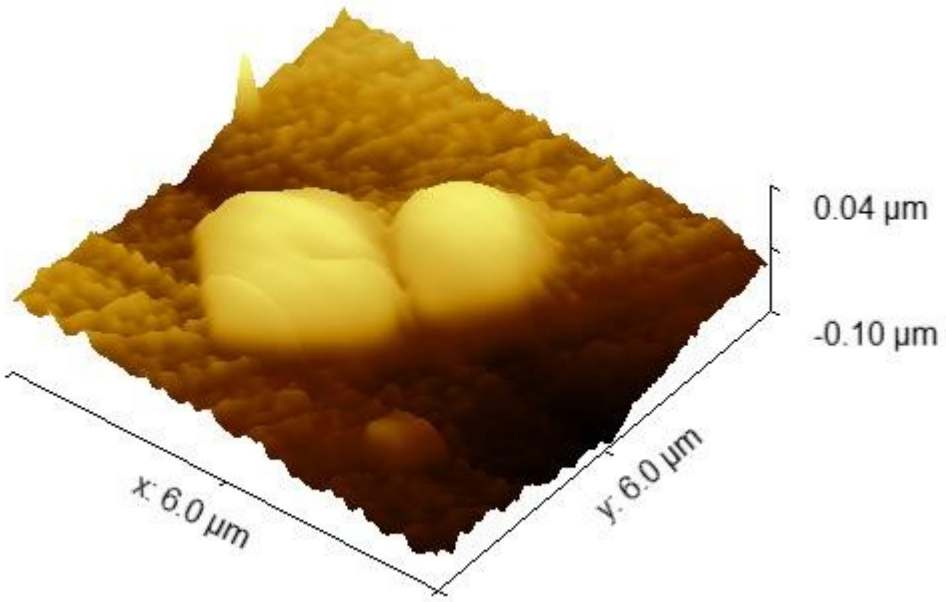

(a)

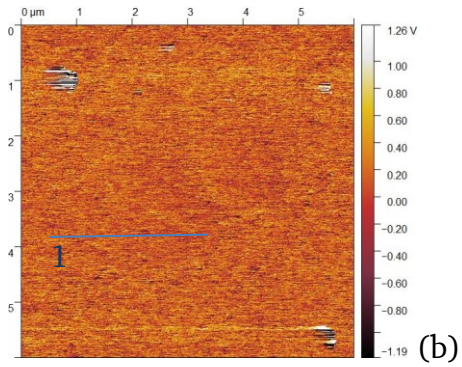

(b)

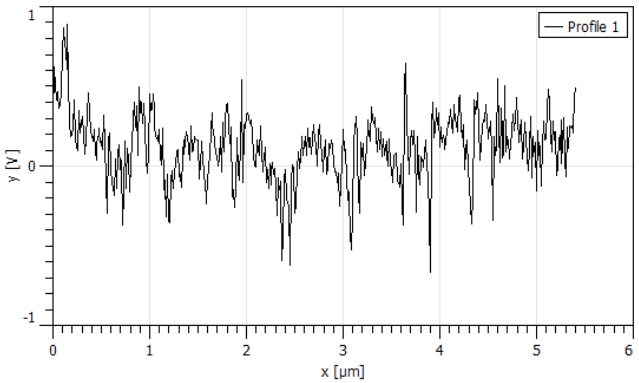

(c)

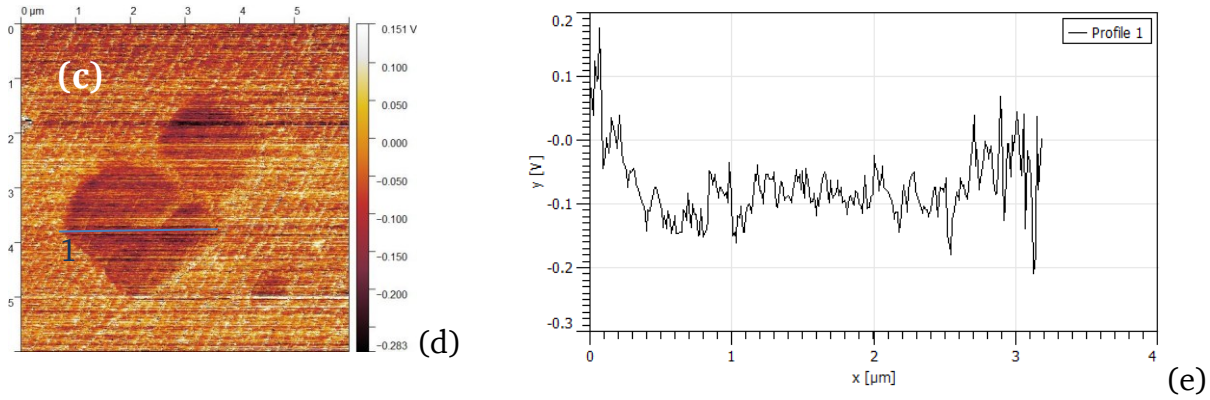

Figure 29: SKPFM measurements of the potential distribution on the Nb(C,N) inclusion. a) AFM measurement of the topography; b) potential distribution measured with the compensation voltage applied to the sample; c) potential line profile corresponding to the graph b); d) potential distribution measured with the compensation voltage applied to the sample after etching; e) potential line profile corresponding to the graph d)

These measurements point out that both kinds of carbonitrides presented in the microstructure of alloy 718 (Ti(C,N) and Nb(C,N)) are expected to reveal a rather noble corrosion behavior in comparison to the surrounding matrix. Same tendency was observed for the δ phase, which was found to be about 30-60 mV nobler than the surrounding matrix, Figure 30.

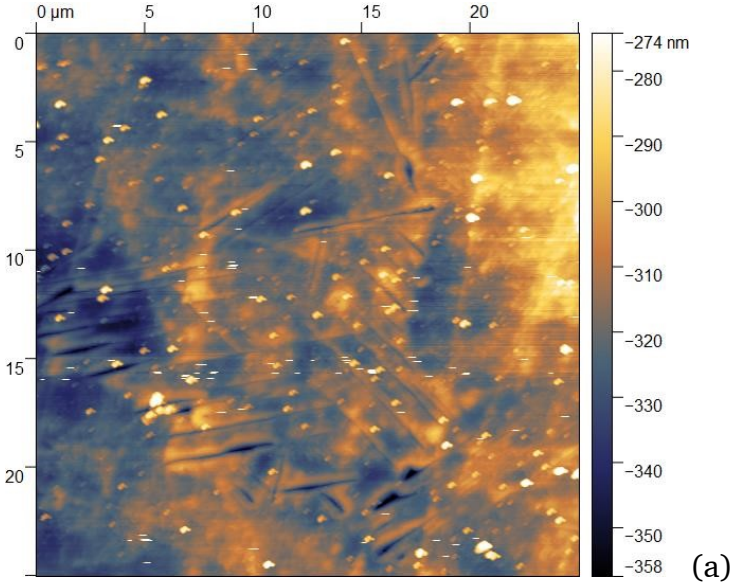

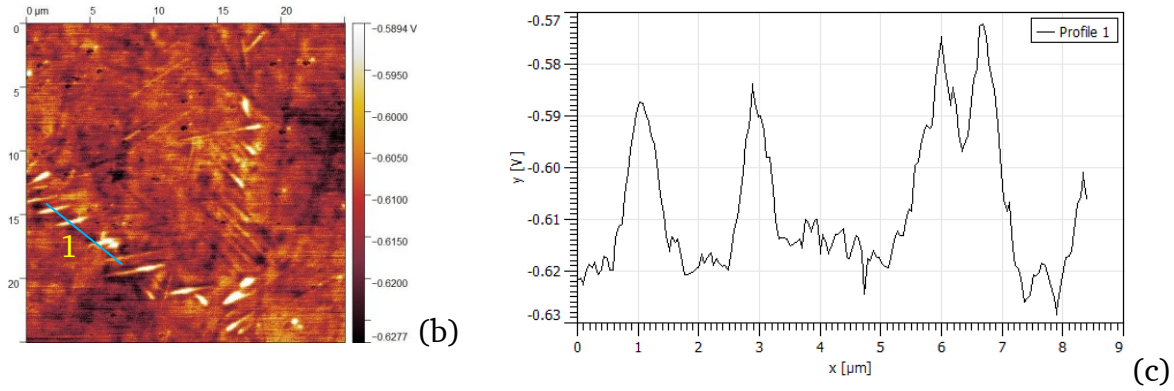

Figure 30: Measurements on δ phase of a polished sample (OPS-etching) a) AFM measurement of the topography; b) potential distribution on corresponding site measured with the compensation voltage applied to the AFM tip; c) potential line profile corresponding to the graph b)

Since all the intermetallic inclusions reveal a certain CPD to the surrounding matrix, it can be assumed that the matrix/inclusion interfaces would act as preferential sites for localized corrosion attack when the material is subjected to corrosive electrolytes.

5.5 Mechanical properties

Variation of the mechanical properties of the material in regards to the change of aging temperature was examined via measurements of hardness (DIN EN ISO 6507-1 [184]) and tensile tests (DIN EN ISO 6892-1[185]). Round smooth specimens were used for this purpose, Figure 72. The hardness measurements were performed on the polished samples according to the measurement specification DIN EN ISO 6507-1 via measurement device Struers DuraScan-70 with the measurement uncertainty of 9.9 HV10. The original hardness values were obtained in HV10 and converted to the HRC values according to the DIN EN ISO 18265 [186] specification.

As expected, both material hardness and strength values decreased along with the increasing content of the δ phase, Table 8.

Table 8: Mechanical properties of alloy 718 in relation to the aging temperature

Material variant	Yield strength (average of 3 tests) [MPa]	Tensile strength (average of 3 tests) [MPa]	Hardness, HRC (average of 5 measurements)	δ-phase content [μm^{-1}]
720+620	1112±18	1318±5	43.3±0.9	0.02
760	976±12	1266±7	40.4±0.4	0.02
775	940±33	1254±16	37.2±1.1	0.16
800	834±47	1195±14	35.5±1.2	0.46
870	535±10	955±7	21.0±0.3	$\gg 1$

Fracture surface observation of the tested samples revealed ductile failure mode with characteristic dimples for all of the samples. Figure 74.

5.6 Conclusions to the chapter 5

The results presented in this chapter have identified the major differences of the chosen material variants regarding their microstructure and mechanical properties. Due to the applied approaches regarding the metallographic characterization, it was possible to quantitatively describe the obtained material conditions and therefore establish a correlation between the aging procedure and the resulting microstructural peculiarities. It was shown

that the increase in the aging temperature led to the coarsening and coalescence of the $\gamma' + \gamma''$ precipitations as well as to the enhanced precipitation of the grain boundary δ-phase. At the same time, no significant changes of the carbonitride morphology was observed for material variants aged at different temperatures.

In addition, Scanning Kelvin Probe measurements performed on the intermetallic inclusions revealed that both carbonitrides and δ phase precipitations appeare to be noble in comparison to the surrounding matrix and therefore might act as sources for galvanic corrosion when immersed into aqueous solutions.

The outlined observations provide a basis for the interpretation of the following investigations of the corrosion and hydrogen embrittlement susceptibility of alloy 718.

6 Results of corrosion tests

6.1 Potentiodynamic scan measurements

Potentiodynamic scan measurements were performed on the material variants 760 and 870 to investigate possible effects of the aging temperature on the pitting susceptibility of the material. Five test series with the variation of temperature, pH value, sodium chloride concentration and the polarization scan rate were carried out for each material to obtain the testing conditions under which the differences in corrosion behavior are the most pronounced. The evaluation of the material performance was implemented by comparison of the breakdown potential values which were determined at the anodic current densities of 100 μA/cm², Figure 31.

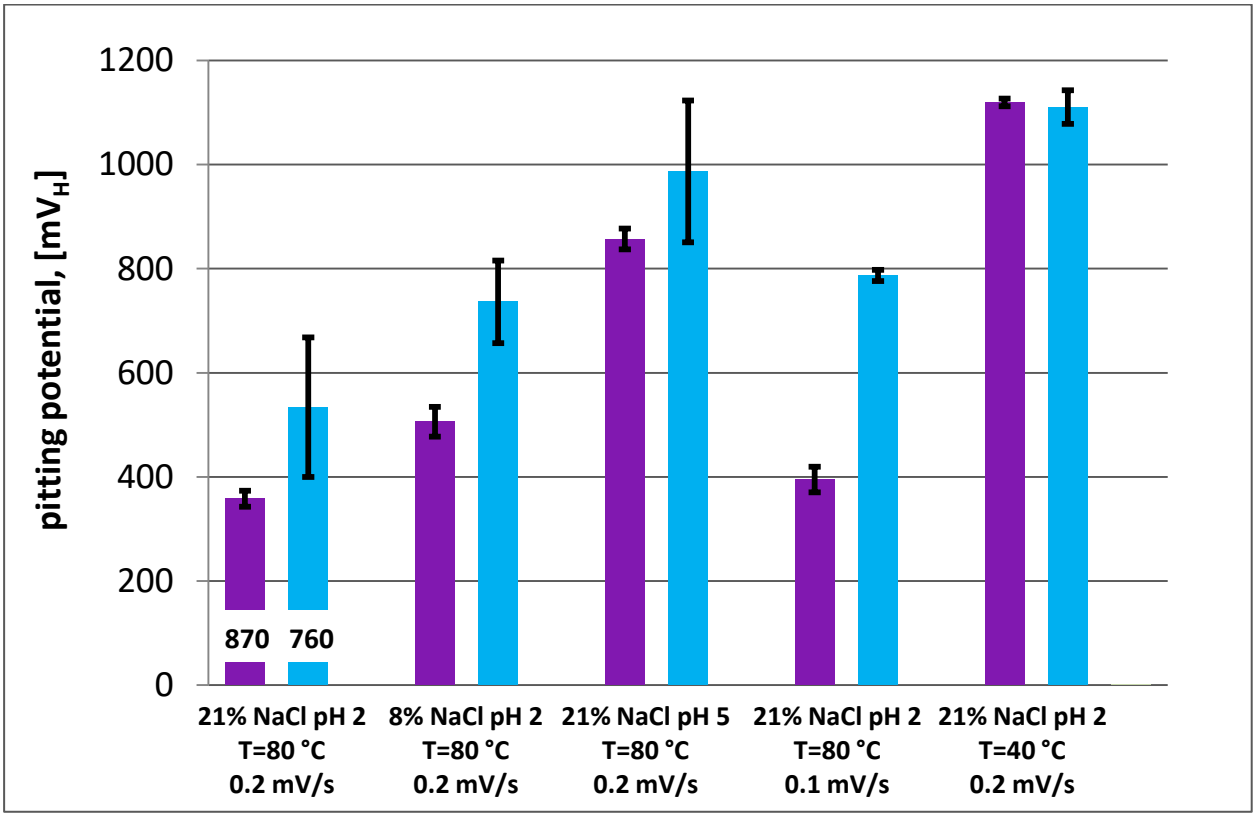

Figure 31: Influence of δ phase content on the pitting potential, measured at different testing conditions, adopted from [101]

Temperature is found to be the strongest factor impacting the corrosion behavior. When tested at 40 °C both material heats demonstrate a passive behavior throughout the whole polarization range with a slight increase near 1100 – 1200 mV$_H$, Figure 32. Reversion of

the polarization lead to the immediate drop of the anodic current density to values below the passive range (~100 μA/cm²). No significant differences of the material performance can be recognized at these testing conditions.

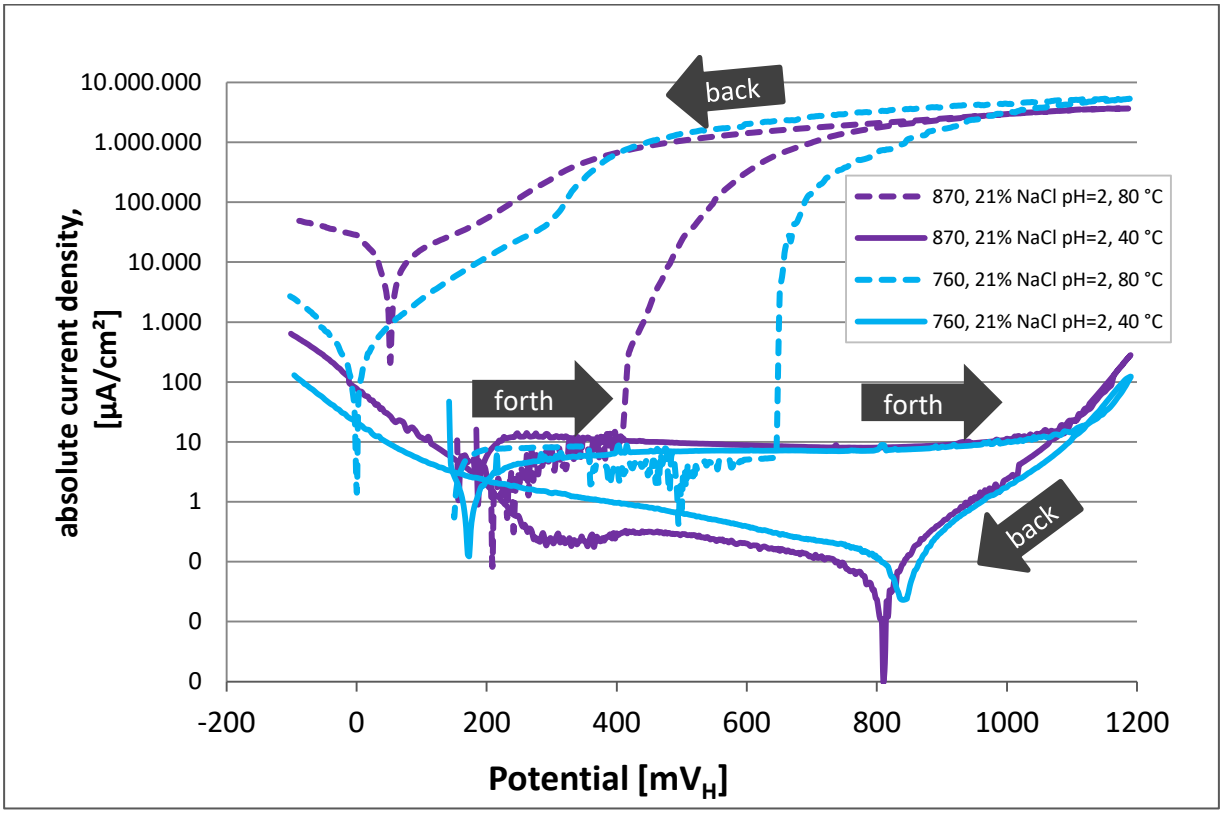

Figure 32: Temperature influence on the potentiodynamic scan measurements on alloy 718 with different content of δ phase, adopted from [101]

An increase of the temperature up to 80 °C results in the reduction of the passive potential areas along with the value of the breakdown potential for both material variants, Figure 31. However, the material 870 revealed a tendency for lower pitting potentials compared to the material 760, indicating a reduced resistance to localized corrosion. In the electrolyte with the reduced concentration of sodium chloride, both material variants demonstrated an increase in the pitting potential values of approx. 150 mV (obtained in 8% NaCl pH=2). On the other hand, an increase of the pH value to 5 leads to the further shift of the breakdown potentials to the noble range, even though the sodium chloride concentration remained high (21%). In 21% NaCl solution pH=5 material 760 exhibited breakdown potential similar to the one obtained at 40 °C. The observed alteration of the material behavior, caused by the increase of solution pH value, is most likely attributed to the improved re-passivation, due to the reduced concentration of hydrogen cations, (see chapter

2.4). Influence of the surface re-passivation processes on the material corrosion performance appears even more distinct, when tested at slower polarization scan rate (21% NaCl pH=2 at 0.1 $mV \cdot s^{-1}$), because the system is given more time to adjust to the corrosion encroachment. Therefore, the explicit differences in the pitting potential values, observed for both materials when tested at 0.1 $mV \cdot s^{-1}$, clearly indicate that discrepancies in the material performance are caused by the passivation and/or re-passivation processes. Certain differences between the two material variants were identified during the sample surface observations after the conducted experiments, Figure 33. The corrosion products built up within the pit appeared to be dark and shiny in case of the variant 760, Figure 33-a, and rather light and matt for the variant 870, Figure 33-b. However, after the removal of the corrosion products, the differences were gone, Figure 33-c and Figure 33-d.

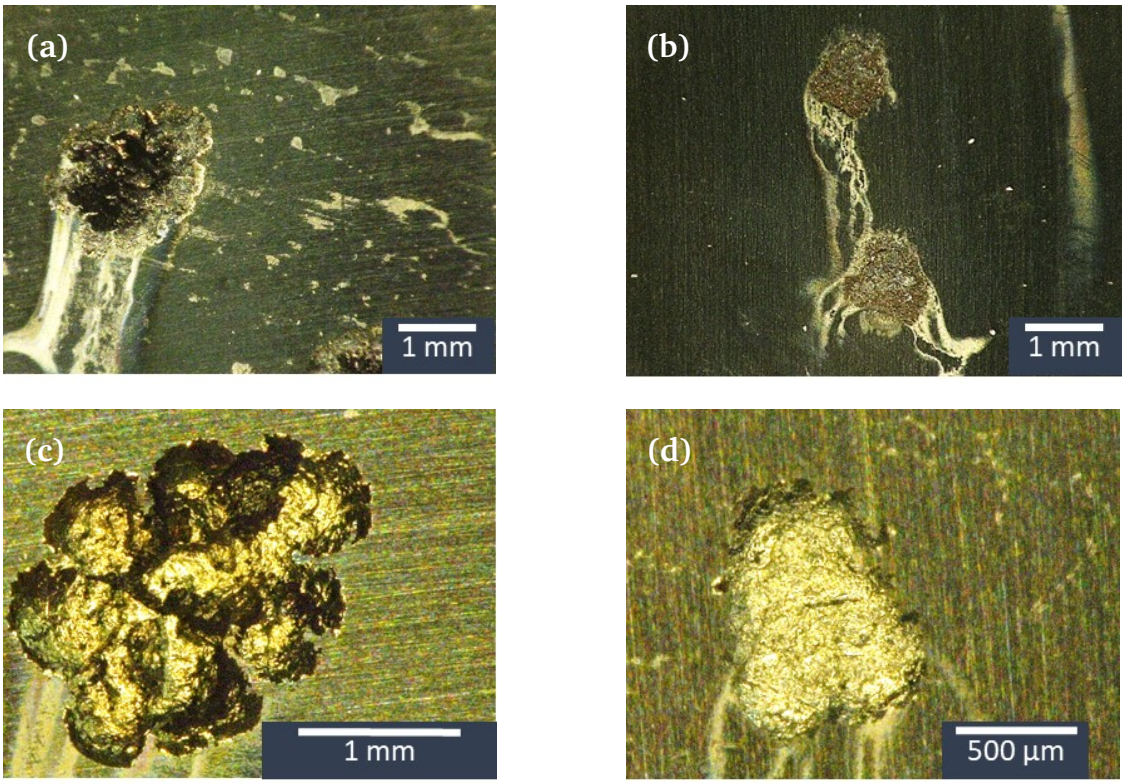

Figure 33: Exemplary light microscopy micrographs of the alloy 718 after the potentiodynamic scan tests in 21% NaCl pH=2 at 80 °C (a,c)material variant 760; (b,d) – material variant 870

Additional material variants with less significant differences in the material microstructure were tested in 21% NaCl solution pH=2 at 80 °C with 0.1 $mV \cdot s^{-1}$ scan rate, as the most distinct differentiation of the material variants behavior was observed at this experimental conditions. Obtained pitting potentials imply a slight correlation between the corrosion behavior of the material and its δ phase content, Figure 34.

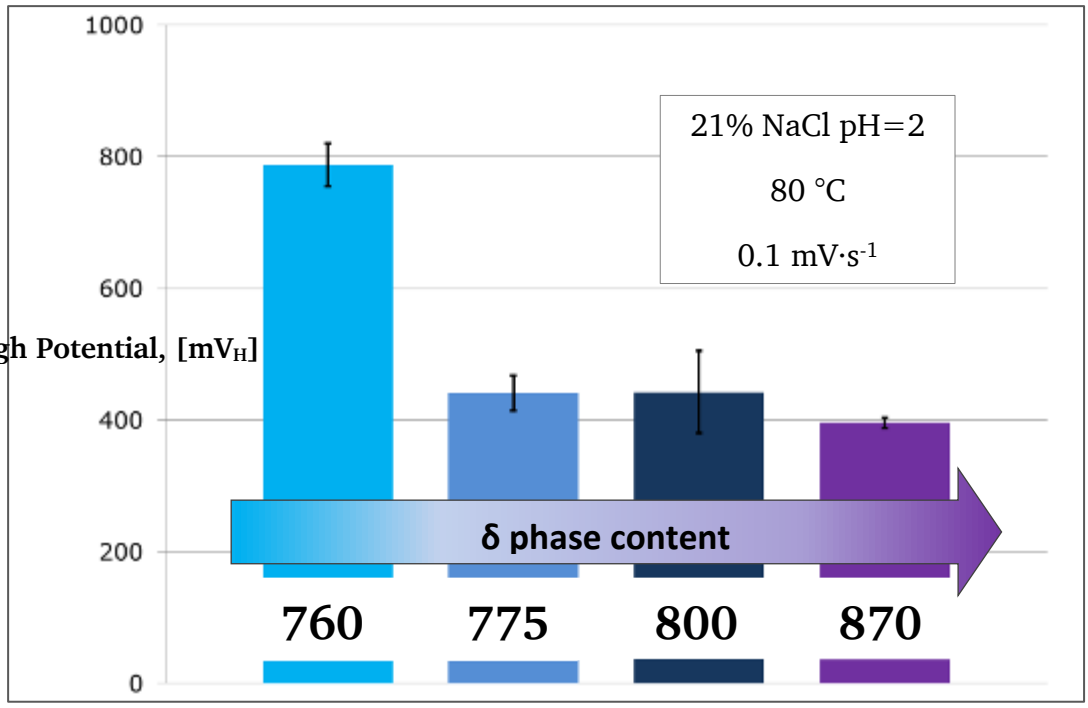

Figure 34: Breakthrough potential in regards to the δ phase content, measured in 21% NaCl pH=2 at 80°C with a polarization scan rate of 0.1 mV·s^{-1}

The observed drop of the pitting potential in the diagram from Figure 34 implies a possible existence of some critical amount of δ phase, beyond which the local corrosion resistance of the material would be impeded.

The electrochemical potentiodynamic scan measurements performed on alloy 718 indicate certain material susceptibility to localized forms of corrosion at elevated temperatures, which is observed to be in slight correlation with the δ phase content, as variant 760 with the smallest amount of grain boundary δ precipitates shows the least local corrosion susceptibility under the tested conditions.

6.2 Open circuit potential measurements

Evolution of the open circuit potential of the samples 760 and 870 over large period of time (15 hours) was recorded in order to monitor the possible differences in the passivation behavior of the alloy 718. The tests were conducted under slightly different conditions to those described in chapter 6.1: 90°C, 21 wt.-% NaCl pH=2.3 as opposed to 80°C, 21wt.-% NaCl pH=2.0. Nevertheless, these deviations are negligible, so that the obtained experimental results still can be compared to the ones presented in the chapter 6.1. Measurements were repeated three times for each material variation to ensure the reproducibility of the obtained values. An increase of the open circuit potential over time is observed for both heats, Figure 35. The difference of the material performance can be evaluated by

the analysis of the potential transients (potential drops), which can be attributed to the nucleation of the non-stable pitting sites. From the plots in the presented diagram, Figure 35, it can be recognized that both material variants demonstrated the transients in the similar potential range. This observation indicates a similar nature of the nucleation sites for the local corrosion for both heats. However, the 10 hours delay in the occurrence of the potential transients suggests that the degradation of the protective passive layer of material 760 took place at a slower rate in comparison to the material 870. Thus, it can be concluded that under the testing conditions that the variant 760 possesses higher passivity and resistance to localized corrosion as opposed to the variant 870.

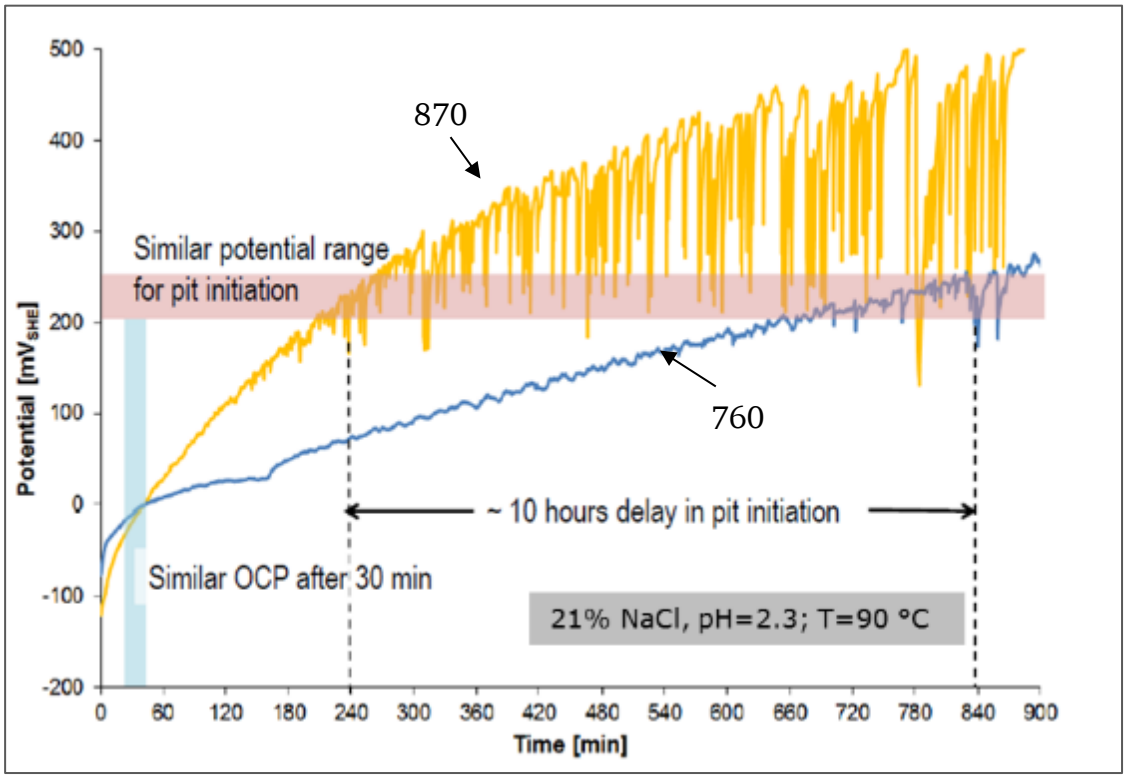

Figure 35: OCP measurements of material 870 and 760 in 21% NaCl solution pH=2.3(HCl)

Subsequent to the electrochemical tests the sample surfaces were examined by means of light microscopy and SEM in order to identify the sites of localized corrosion. Scanning electron microscopy reveal small pitting-like defects with similar appearance on both material variants, Figure 36. Local EDX-measurements were carried out to identify the nature of this defect points. According to the measurements, those defects appear to be titanium and niobium carbonitrides (Ti,Nb(C,N)), Figure 37.

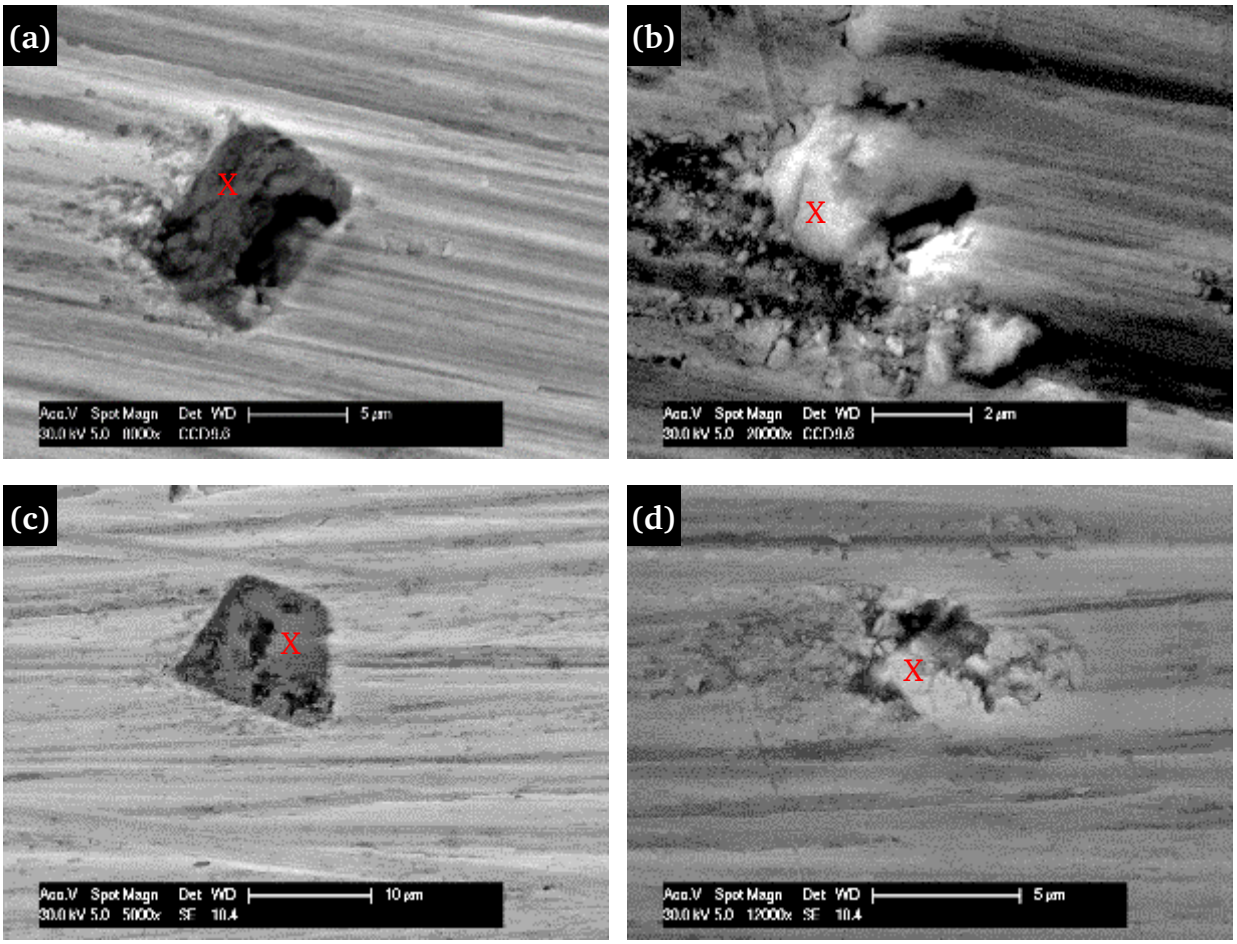

Figure 36: Surface examination of the aged alloy 718 after open circuit potential measurements: (a) and (b) – material 760; (c) and (d) – material 870

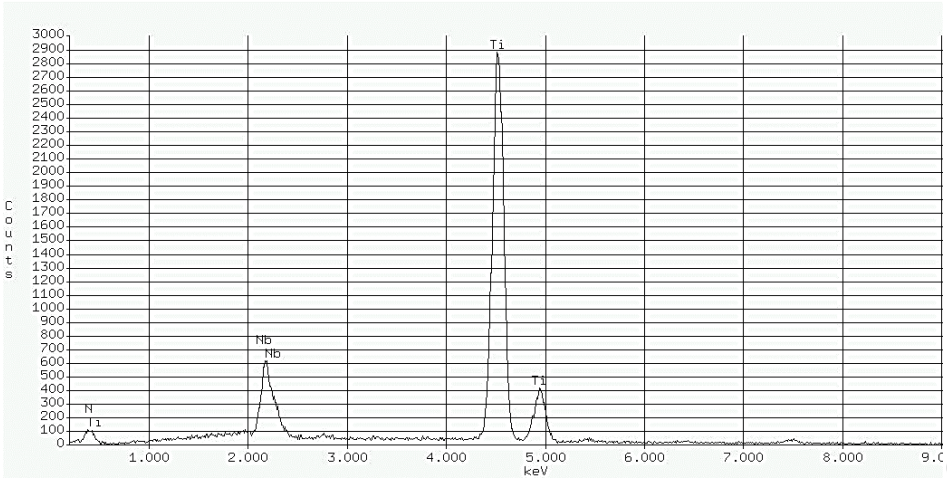

(a)

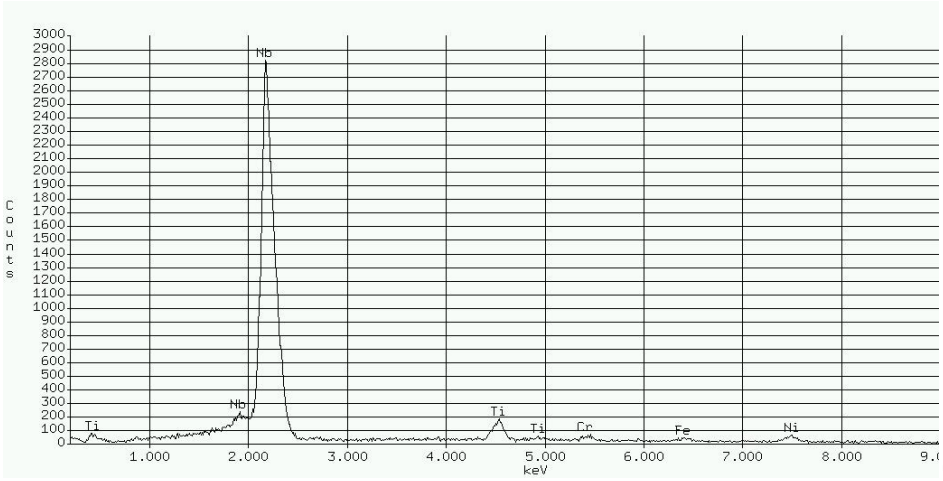

(b)

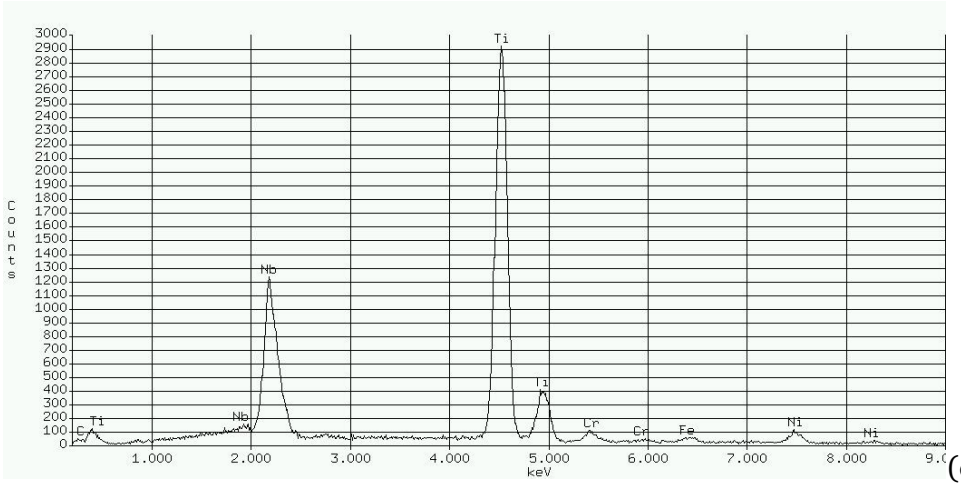

(c)

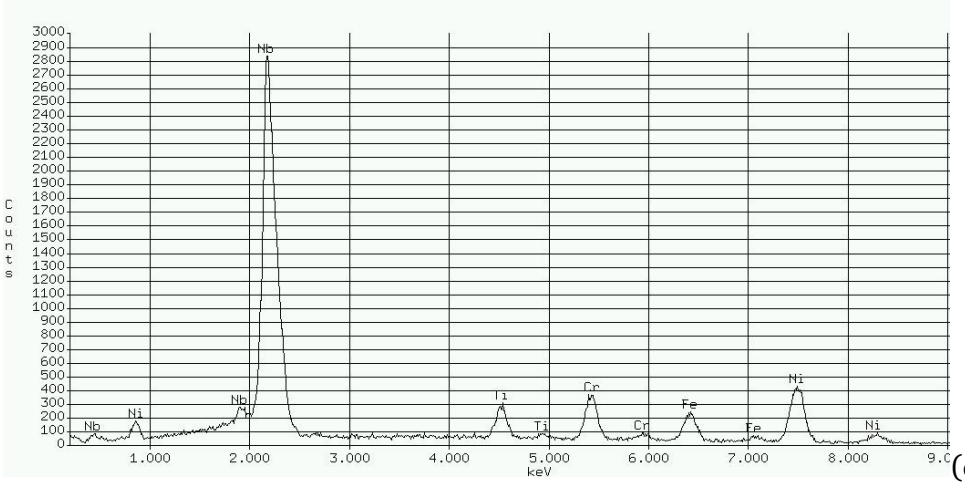

(d)

Figure 37: EDX-measurements on the pitting sites, presented in Figure 36: (a) EDX-spectrum corresponding to the Figure 36-a; (b) EDX-spectrum corresponding to the Figure 36-b; (c) EDX-spectrum corresponding to the Figure 36-c; (d) EDX-spectrum corresponding to the Figure 36-d

Statistical analysis of these defects by means of 3d microscopy (Leica DCM 3D) identifies some differences in their shape in regard to the aging procedure. In case of material 870 they appear to be slightly deeper and wider as compared to material 760, Figure 38. This difference can be attributed to the earlier onset of the semi-stable pitting corrosion on the

material variant 870, and as a result a longer lasting active corrosion process.

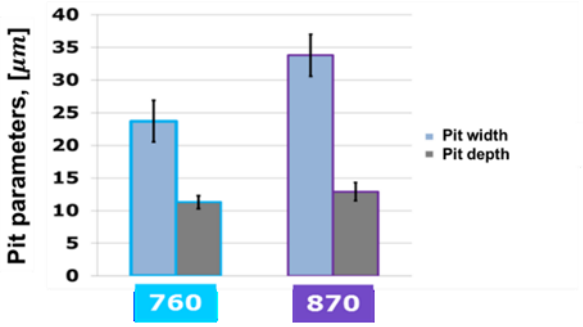

Figure 38: Width and depth of the surface defects on aged alloy 718 after open circuit potential measurements measured on 10 different pitting sites

The outlined results of electrochemical open circuit potential measurements, carried out on the alloy 718 at 90 °C in 21% sodium chloride solution pH=2.3 (HCl), confirm the differences in material susceptibility to localized corrosion reported in chapter 4.1.1. However, the recorded OCP (Open Circuit Potential)-transients demonstrate that the nucleation of the meta-stable pits occurs in the same potential range for both material variants, indicating the same nature of the pits in both cases. SEM observations of the tested samples and the EDX measurements performed on the corrosion defects allowed to identify them as Ti,Nb(C,N). No corrosion defects could be attributed to the presence of the δ phase precipitations.

6.3 Electrochemical impedance spectroscopy measurements

Differences in material passivation behavior with respect to the aging procedure were investigated by means of electrochemical impedance spectroscopy (EIS) measurements. This measurement technique provides the necessary sensitivity to address the question about the influence of the aging temperature and hydrogen dissolved in the bulk on the material ability to passivate in corrosive electrolytes. Experiments consist of seven single measurements which were performed one after another for the total duration of four hours. Comparison of the data obtained in the beginning and at the end of the test sequence allows to make a conclusion about passive layer alterations under different testing conditions. Two concentrations of sodium chloride solutions (0.5 and 5 wt.-%) acidified to pH 3 by addition of hydrochloric acid were used for the study of the hydrogen impact on the passivation processes. The reduction of the sodium chloride concentration in comparison to the previous tests aimed for the higher differentiation of the experimental results and less intense corrosion reactions. Bode plots of the experimental data demonstrate the impedance and phase as a function of the potential frequency for samples of material 760 with and without hydrogen pre-charging, measured in 0.5 wt.-% and 5.0 wt.-% sodium chloride

solution pH 3, Figure 39-a and Figure 39-b. The curves corresponding to the measurements in 5 wt.-% sodium chloride solution can be gained from the annex, Figure 69 and Figure 70. Comparison of the impedance curves at the beginning and at the end of the measurement series reveals an increase of impedance values measured at 10^{-2} Hz in both cases, indicating the sample surface passivation during the experiment. Introduction of hydrogen into the sample leads to the reduction of the polarization resistance immediately from the start of the measurement: the impedance curves of hydrogen charged samples are below the impedance curves of the samples without hydrogen charging. In case of the material 760 this gap becomes smaller, Figure 39-a, suggesting a negligible effect of hydrogen on the passivation at the given corrosion conditions. In contrast, the gap between the impedance measured for the material 870 with and without hydrogen charging is getting larger with the time, Figure 39-b.

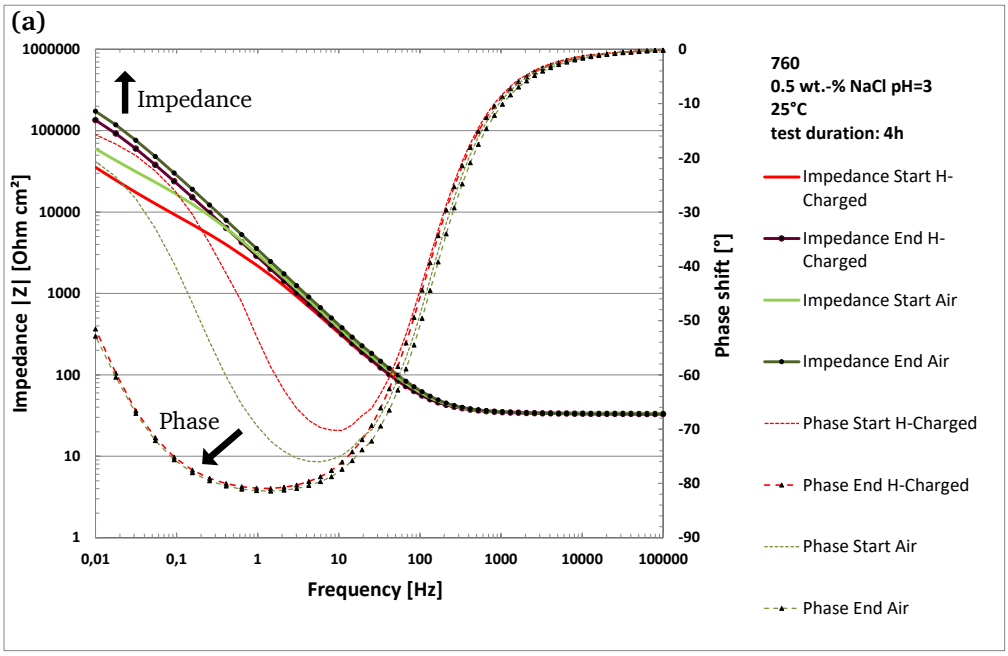

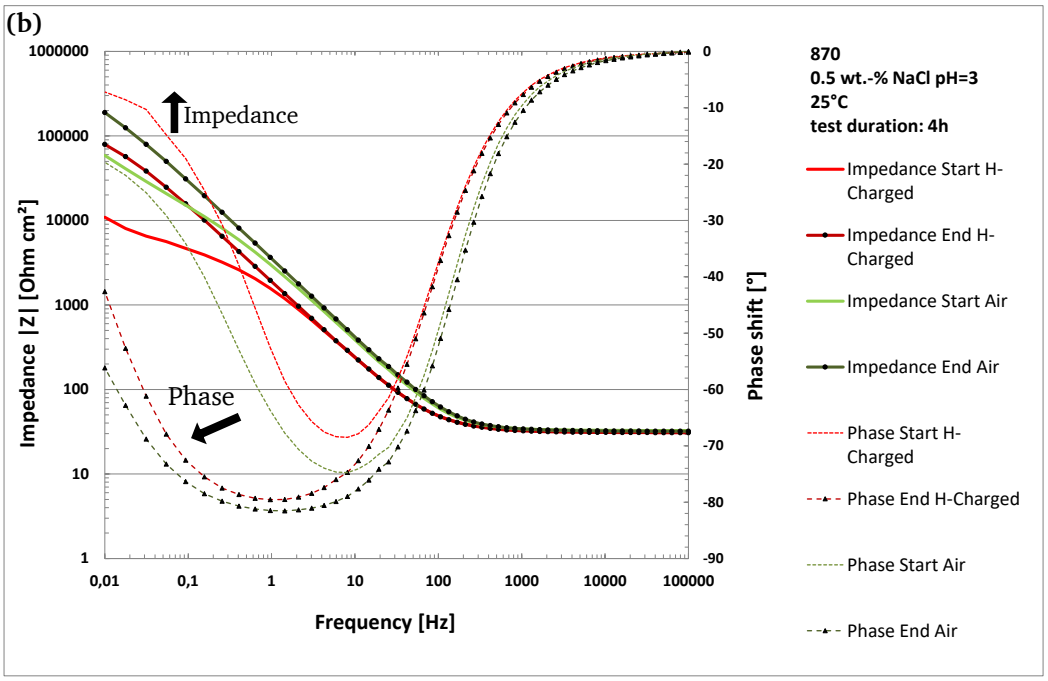

Figure 39: Comparison of the Bode plots of EIS measurements (a) material 760 in 0.5% NaCl pH=3; (b) material 870 in 0.5 wt.% NaCl pH=3

Comparison of the polarization resistance values measured at the end of the test cycle in a chart diagram point in Figure 40 demonstrates an enhanced detrimental effect of hydrogen in case of the material 870.

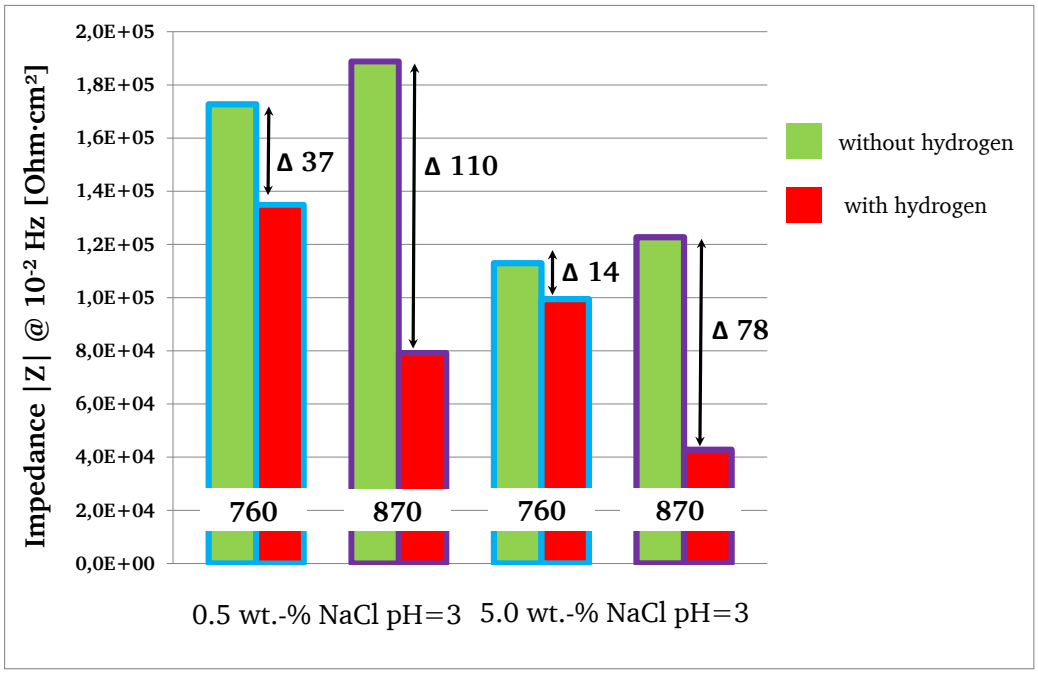

Figure 40: Polarization resistance measured at 0.01 Hz for material variants 760 and 870 at the end of each measurement cycle

Roughness profile measurements were carried out for each sample to quantify the surface

corrosion depth and morphology, Figure 41.

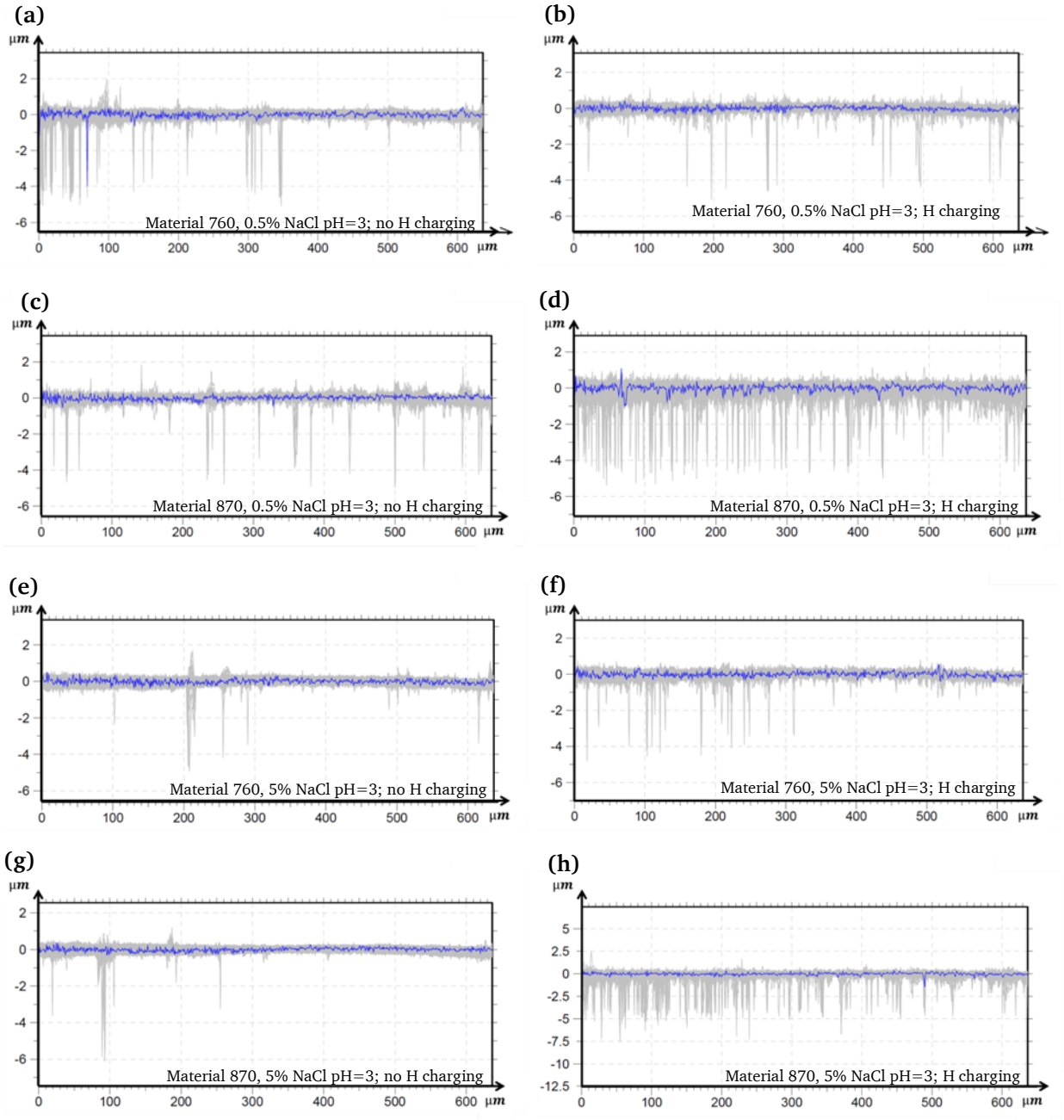

Figure 41: Surface topography profiles of the sample's surfaces after the EIS measurements

The graphs in Figure 41 represent each 360 roughness profiles, captured on the surface of each sample after the EIS measurements. Thus, these profiles can be taken as a characteristic for the corrosion damage. It can be seen that in the absence of hydrogen both material variants show similar degradation extent in both electrolytes. In contrast to that, introduction of hydrogen to the samples leads to the more distinguishable behavior of the tested materials: it is clear that the variant 870 suffered more than 760.

6.4 Conclusions to chapter 6

Presented results correlate with the sample's surface topography profiles after the EIS measurements. Hydrogen charged samples of material 870 exhibit an increase in surface roughness caused by corrosion defects (Figure 41 d and h) compared to the not hydrogenated samples (Figure 41 c and g). The surfaces topography profiles of the material 760 on the other hand demonstrated no significant difference with respect to the hydrogen precharging.

The results presented in this chapter indicate certain differences in corrosion behavior of the material variants aged at different temperatures. Although the content of the δ phase was one of the most significantly varied microstructural parameters, no direct evidence of any correlation between the δ phase precipitations and nucleation of the corrosion defects was found. All the observed corrosion defects, generated on the sample surface during the corrosion tests were identified as titanium or niobium carbonitrides by means of EDX-measurements. At the same time, the results of material characterization presented in chapter 5.2.1 state no deviations in the fraction of carbonitrides due to the variation of the aging temperature. Thus, the observed differences in electrochemical behavior of the material variants 760 and 870 might result from the changes of the oxide layers, formed on the surface of the sample as a result of the atmospheric oxidation.

7 Results of the hydrogen permeability and solubility examination

7.1 Hydrogen permeation measurements

Hydrogen permeation measurements were initially performed on the solution annealed samples in order to determine the impact of grain boundary diffusion on the hydrogen permeation in the material. The results of the measurements are presented in Figure 42. Measured effective hydrogen diffusion coefficients are two orders of magnitude higher than those declared in literature, [187], [162], [137], [50]. The reason for this rather contradictory result is not entirely clear, but one possible explanation could be the well know concentration dependence of the hydrogen diffusion process, which was reported by other researchers, [188], [189]. This argument seems to be even more convincing once considering the magnitude of the charging current densities, applied in the current experiments for the hydrogen evolution, which happens to be about two orders of magnitude higher than those used in other studies. The high charging current density was chosen to increase the measurement sensitivity, as it directly impacts the measurement accuracy. Another plausible reason for the observed results might be the short-cut diffusion of hydrogen along the grain boundaries, which is a known fact in case of nickel, where grain boundary diffusion was measured to be significantly higher than the bulk diffusion. The obtained results are in agreement with the expectations regarding the correlation of diffusion coefficients with the grain size. The highest diffusion coefficient was measured for the fine grained material variant 1030 with an average grain diameter of 50 to 80 μm. In contrast to that, material variant 1090 with an average grain diameter of about 220 to 320 μm revealed the lowest effective diffusion coefficient of 1.4 10^{-7} cm²/s.

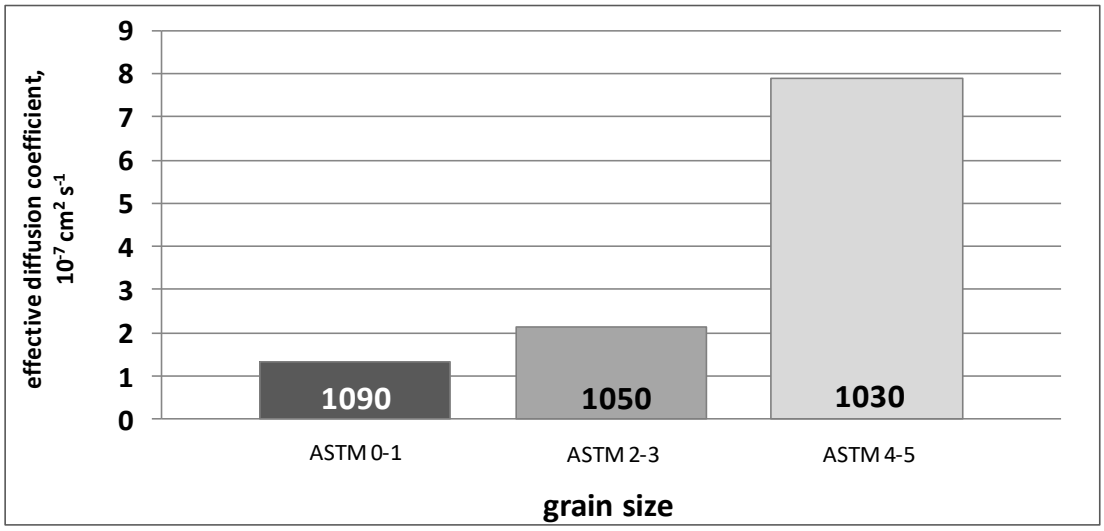

Figure 42: Correlation between the grain size and effective hydrogen diffusion coefficients

Additionally, experiments were carried out on the aged samples of alloy 718 to address

the impact of the secondary phase precipitates on hydrogen diffusion. As can be seen in Figure 43, the presence of secondary phase precipitations led to deceleration of hydrogen diffusion within the material in comparison to the annealed material 1030, Figure 43. This effect can be attributed to the trapping effect of the precipitations, since the grain size remained the same for all the tested samples, Table 4. Material variant 800 with higher amount of grain boundary δ phases and fewer but larger γ'' phases, revealed the lowest hydrogen diffusion coefficient (ca. 1.25 10^{-7} cm^2/s), followed by the material variant 720 (1.6 10^{-7} cm^2/s) with the amount of δ phases similar to the variant 1030 and higher fraction of fine γ'' precipitates. These results appear to be plausible, since the trapping energy of δ phase is slightly higher than the one of γ'', [137]. Surprisingly, material variant 870 with the largest amount of δ phases, observed both on the grain boundaries and within the grain, exhibited the effective hydrogen diffusion coefficient comparable to the annealed sample.

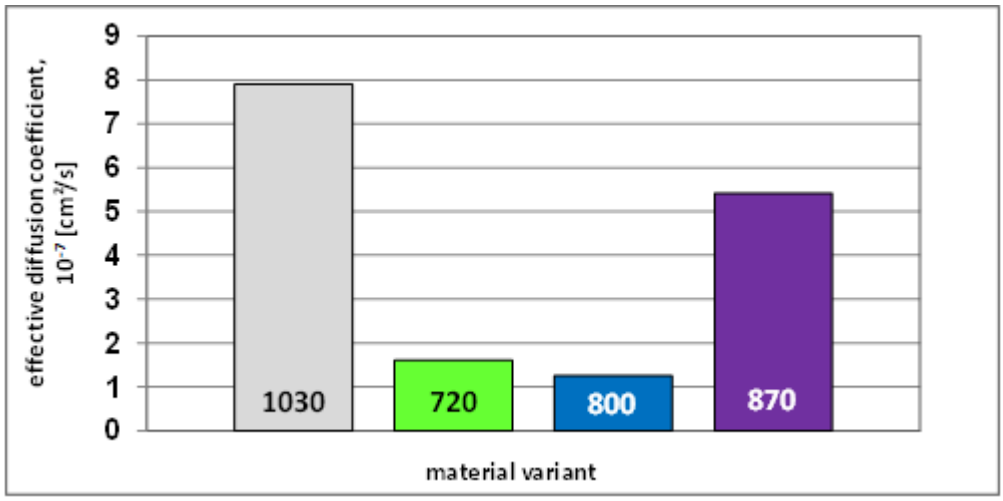

Figure 43: Correlation between the microstructure of the nickel base alloy 718 and the effective hydrogen diffusion coefficients

This observation could be explained when assuming that the hydrogen permeation transients recorded in this study could be assigned primarily to the diffusion along the grain boundaries, whereas the bulk diffusion gives a negligible contribution to the measured signal. Then the hydrogen propagation through the different heats of alloy 718 could be schematically described with the pictograms presented in Figure 44. In the absence of any precipitations on the grain boundary, hydrogen propagates rather quickly along the large inner surface given by the grain boundaries, Figure 44-a. The presence of the secondary phase precipitations would naturally slow down the hydrogen diffusion speed, proportionally to the magnitude of the binding energy of the precipitations, Figure 44-b and Figure 44-c. Large δ phases however, might create alternative inner surfaces for hydrogen

shortcut diffusion path and therefore accelerate the overall hydrogen diffusion in comparison to the material with the lower content of grain boundary δ phases, Figure 44-d.

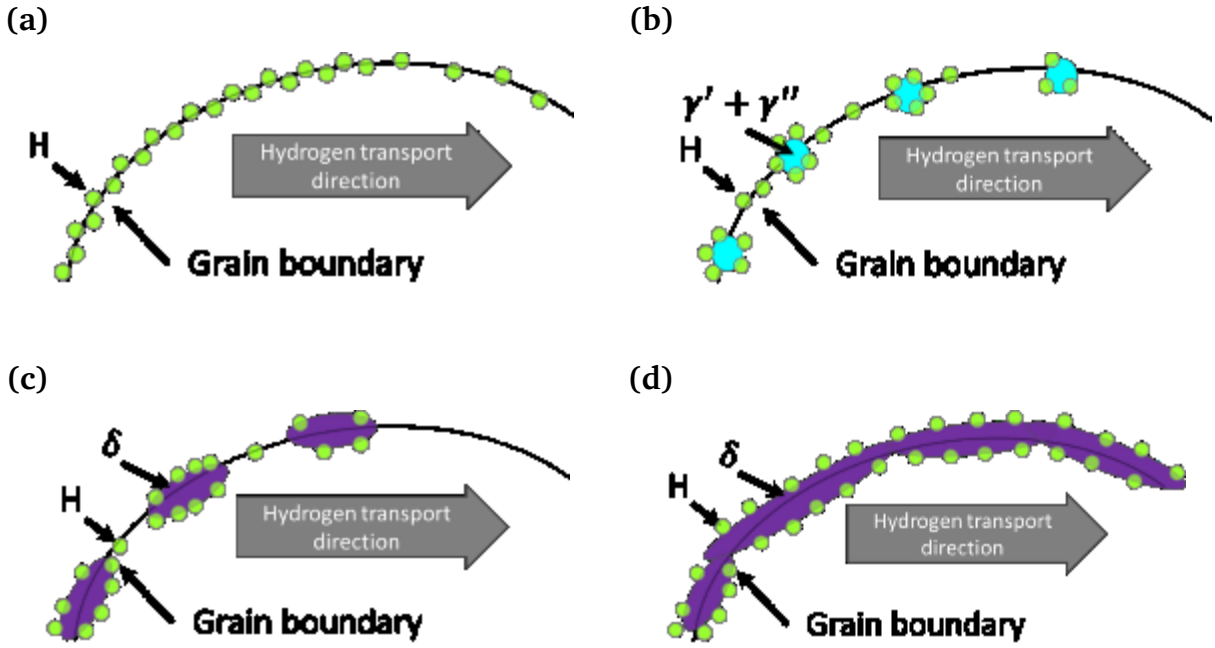

Figure 44: Proposed hydrogen transport mechanism in alloy 718 in the presence of different phase precipitations: (a) hydrogen diffusion along the grain boundaries in the solution annealed material; (b) hydrogen diffusion along the grain boundaries in the variant 720; (c) hydrogen diffusion along the grain boundaries in the variant 800; (d) hydrogen diffusion along the δ/matrix interfaces in the variant 870

It is worth mentioning that aside from the material microstructure, the recorded hydrogen permeation transients might be as well influenced by the oxide layers formed on the surface of the samples entry side during the atmospheric oxidation, as they are well known to impede hydrogen diffusion processes. However, these oxide layers are supposed to be reduced due to the polarization in the cathodic range, applied for the hydrogen evolution reaction. Thus, the impact of this layers on the obtained results can be assumed to be negligible.

7.2 Hydrogen solubility measurements

Differences in the microstructure of the material heats cause slight deviations in the amount of the measured hydrogen, Figure 45. However, considering the detection limit of 0.01 ppm, these differences in total hydrogen content can be assumed as significant. The obtained values of the dissolved hydrogen appear to be lower than reported in the literature, [80]. This deviation might be attributed to the significant differences in the temperature regime of the applied charging procedure (150 °C versus 23 °C chosen in this work).

The lowest hydrogen content is obtained for the annealed samples, whereas the highest amount of dissolved hydrogen is observed for the material variant aged at 800 °C. These observations are in agreement with previous conclusions, since hydrogen concentration seems to increase along with the increment in the fraction of the secondary phase precipitations.

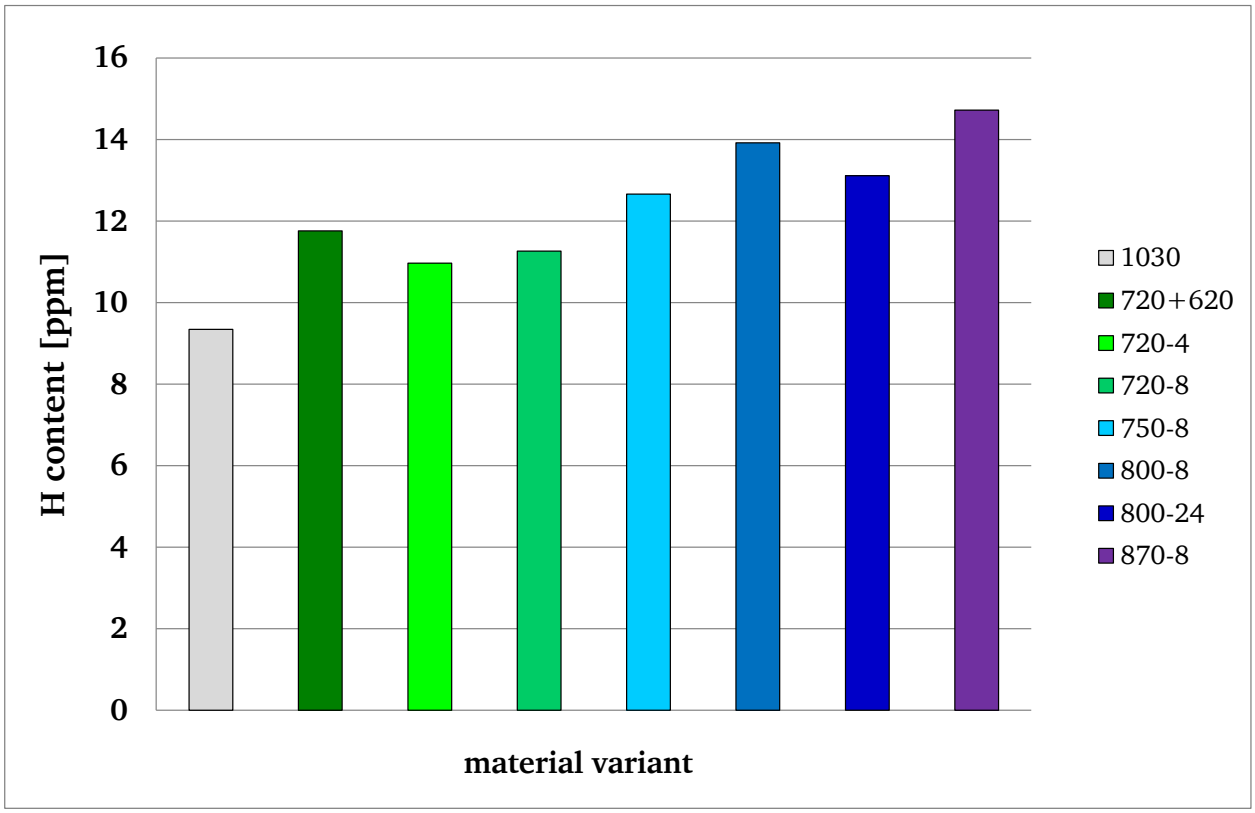

Figure 45: Hydrogen content measured in alloy 718 aged at different temperatures

Since $\gamma' + \gamma''$ and δ precipitates represent reversible trapping sites for hydrogen, a variation of material microstructure regarding their size and density is expected to affect the hydrogen solubility in the material. As the $\gamma' + \gamma''$/matrix and δ/matrix interfaces can be assumed to be the most favorable sites for hydrogen trapping, the concentration of stored hydrogen is expected to depend on the size of the interface areas. To reassess this hypothesis, measured hydrogen contents were plotted in regards to the factor of interface, estimated according to the equation given in (15).

$$S = 2\pi a \cdot \left(a + \frac{b^2}{\sqrt{a^2 - b^2}} \cdot ln\left(\frac{a + \sqrt{a^2 - b^2}}{b} \right) \right) \cdot \theta, \qquad \theta = \frac{N_{\gamma' + \gamma''}}{nm^2} \tag{15}$$

Assuming that the alteration of the precipitation size does not influence their coherency,

the amount of stored hydrogen is expected to linearly increase along with the interface $\gamma' + \gamma''$/matrix. It is evident from the diagram on Figure 46 that all the investigated material (except for 720-8) variants reveal this proportionality.

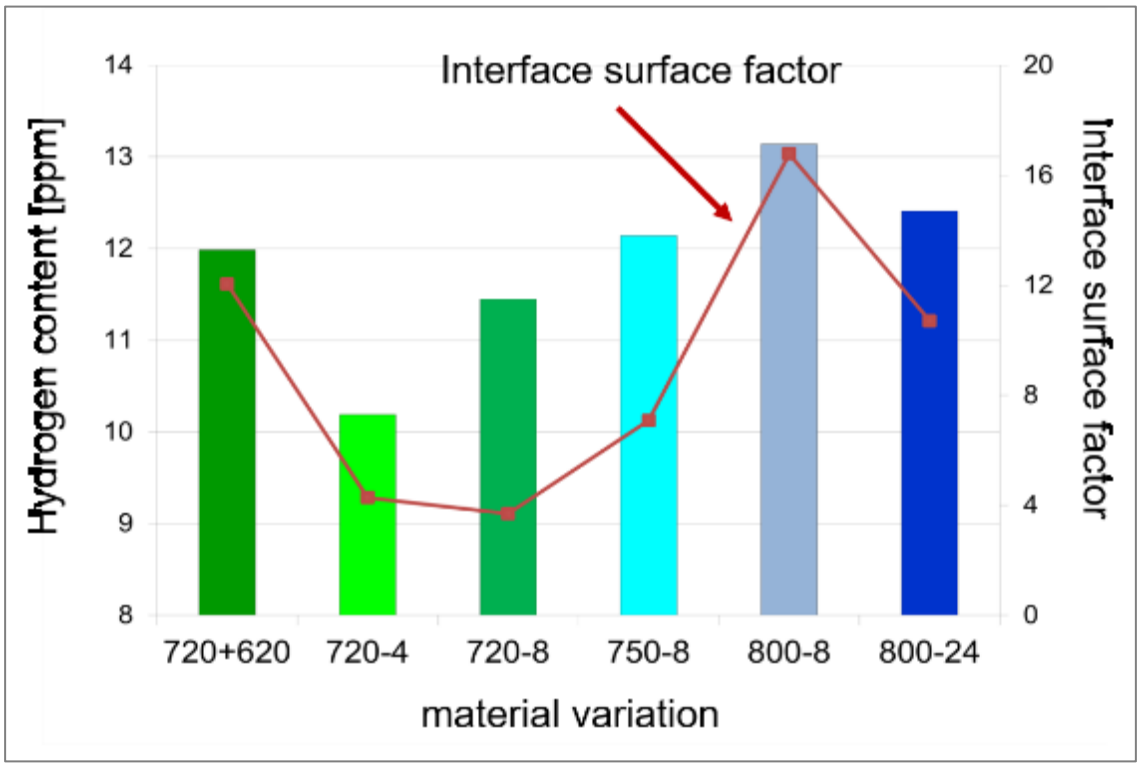

Figure 46: Correlation between the hydrogen content and the $\gamma' + \gamma''$/matrix interface

7.3 Conclusions to chapter 7

Comparing the measured hydrogen contents to the estimated values of effective hydrogen diffusion coefficients, it is evident that the measurements demonstrate a certain correlation. For instance, the solution annealed variant with the highest effective diffusion coefficient demonstrates the lowest hydrogen solubility among the tested material heats. The same observation can be made for the material variants 720 and 800: in both cases hydrogen solubility appears to be inversely proportional to the measured diffusion coefficients. Therefore, the reduction in hydrogen propagation speed observed for aged specimens of alloy 718 could be attributed to the trapping effect of the secondary phase precipitates.

The results presented in this chapter illustrate that the phenomena of hydrogen diffusion as well as hydrogen solubility in alloy 718 are surely influenced by the physical metallurgy of the material. The obtained values of effective hydrogen diffusion coefficients imply the preferential hydrogen diffusion along grain boundaries (as opposed to the bulk) and its

trapping on the secondary phase precipitates. Further, the observed trends confirm the results of the previous findings, which suggested the binding energy of the δ phase to be slightly higher than that of $\gamma' + \gamma''$ precipitates.

8 Examination of hydrogen embrittlement susceptibility

The impact of the aging temperature on the hydrogen embrittlement (HE) susceptibility of alloy 718 was investigated via tensile tests at a constant displacement rate, which were performed on the round notches samples as described in chapter 4.3. As it was stated in chapter 2.3 material degradation due to the stress corrosion cracking is often supported by hydrogen embrittlement damage mechanism. Thus, examination of the possible correlations between the material microstructure and its susceptibility to hydrogen embrittlement might provide an important insight for the metallurgic improvement of the material performance.

8.1 Tensile tests at a displacement rate (0.2 mm/h) under simultaneous cathodic hydrogen charging

Tensile tests conducted at a displacement rate of 0.2 millimeter per hour can be considered as rather fast, especially when taking into account the low hydrogen diffusivity in alloy 718. Representative curves for the alteration in tensile force and the sample elongation recorded during the test for each of the investigated material heats are presented in Figure 47. Due to the chosen sample geometry, sample elongation during the experiment was measured by means of crosshead travel signal obtained from the tensile testing machine.

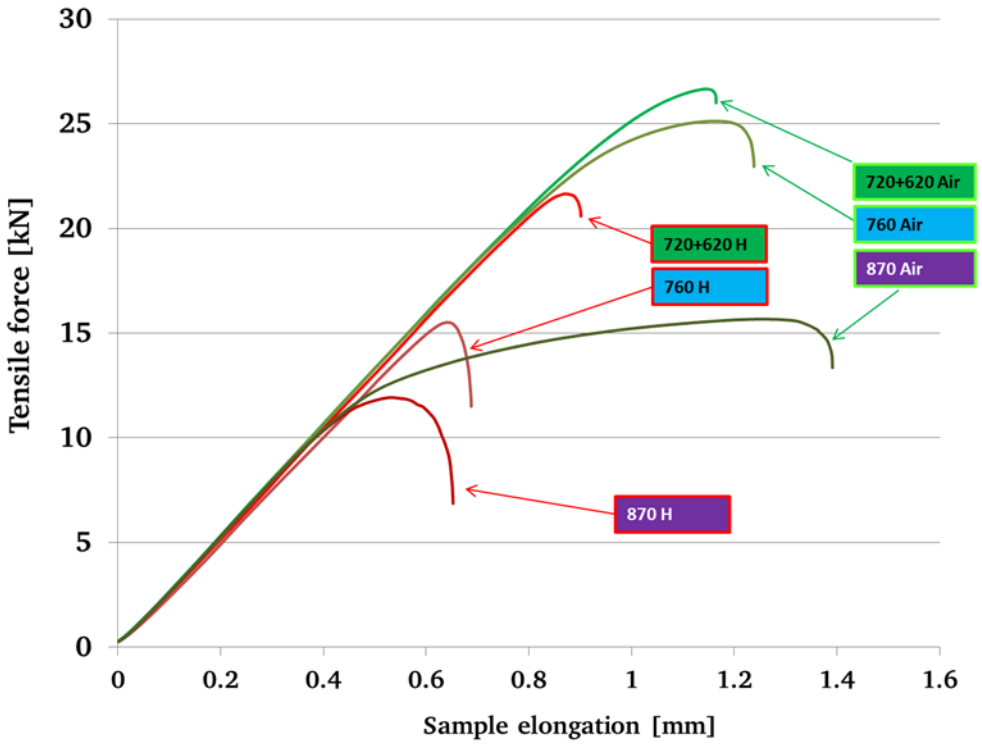

Figure 47: Tensile force - elongation curves of different alloy 718 heats obtained during SSR tests (displacement rate 0.2 mm/h) in air at 23°C (green lines) and under simultaneous hydrogen charging (30 mA/cm² in 1.0 M $(NH_4)_2SO_4$ at 23°C) (red lines)

The curves obtained in air demonstrate an agreement with the expected material behavior based on the hardness measurements: an overaged heat 870 exhibits the largest sample elongation, whereas the hardest (>43 HRC) double-step aged material yielded at the highest tensile force and the smallest elongation. Simultaneous hydrogen charging performed during the tensile testing leads to the reduction of both tensile force and the total sample elongation. However, as the material ranking remains to be the same in terms of the yielding tensile force, the total elongation of the samples reveals the opposite trend. The specimens of the overaged material 870 now exhibits both lowest yield force and elongation whereas the hardest material 720+620 demonstrates only minor performance alteration in the presence of hydrogen. The calculated hydrogen embrittlement (HE) coefficients presented in the chart diagram in Figure 48, quantify the observed trend. At first sight, the results presented on the diagram imply a rising HE susceptibility of the alloy 718 which goes along with the increase in the aging temperature. The estimated content of the grain boundary δ phase of the material heats 720+620 and 760 is the same, yet there is a significant difference in the material performance. Therefore, the difference in the material performance cannot be attributed to the grain boundary δ phase alone.

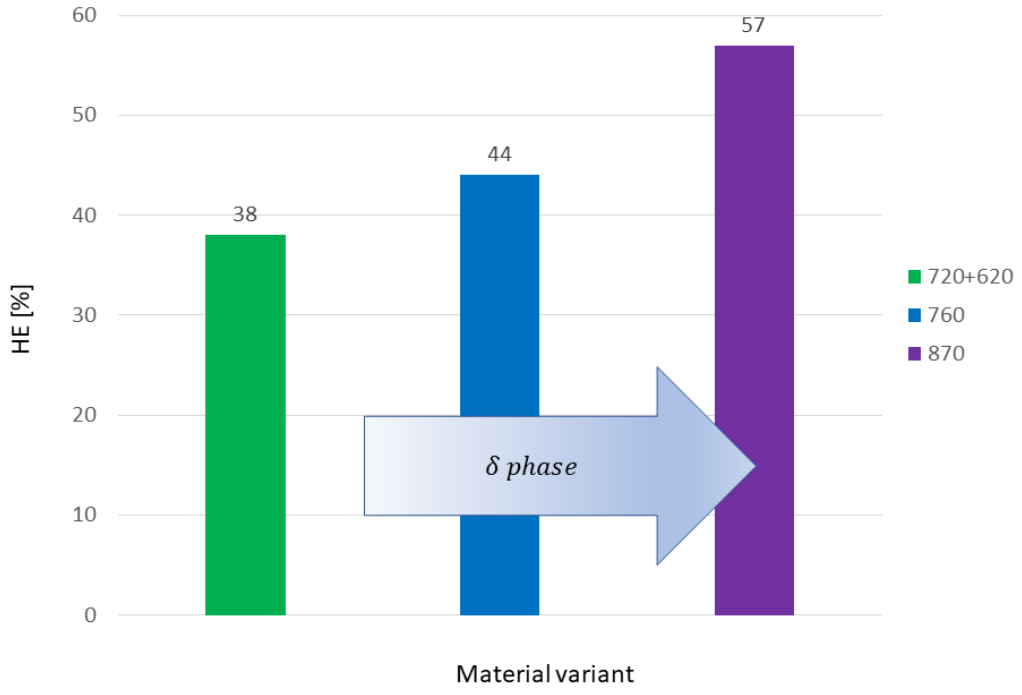

Figure 48: Hydrogen embrittlement susceptibility of aged alloy 718 in regards to the heat treatment temperature estimated via SSR tests at the displacement rate of 0.2 mm/h

Secondary electron microscopy observations of the fracture surfaces indicated a combination of the dimpled ductile fracture mode in the center of the specimen and a brittle ring facing the outer sample's surface, Figure 49.

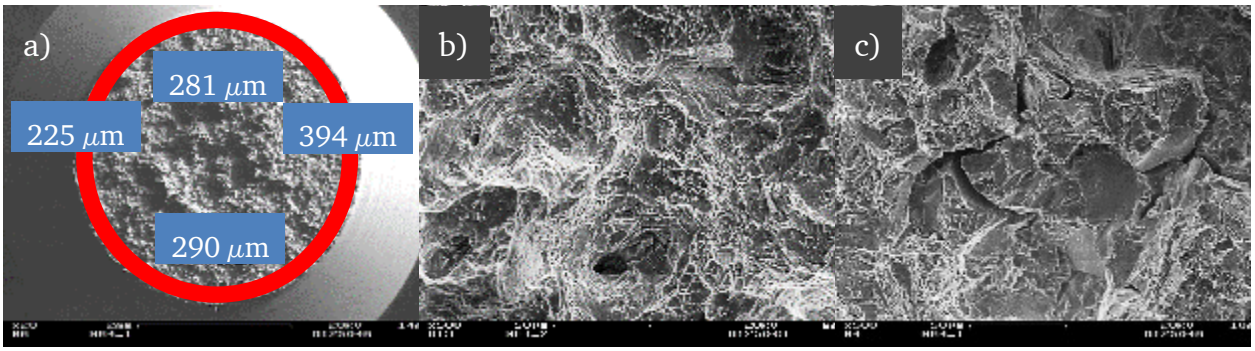

Figure 49 a) Fracture surface of the double-step aged alloy 718 (720+620), failed due to the tensile test with a constant displacement rate (0.2 mm/h) under simultaneous cathodic hydrogen charging (30 mA/cm² in 1 M $(NH_4)_2SO_4$) at 23°C; (b) detailed view of the center area; (c) detailed view of the brittle area, marked with the red ring

Detailed examination of the fracture surfaces by means of SEM revealed variation of the width of the brittle outer ring among the chosen material heats, Figure 50. Comparing the SEM micrographs presented in Figure 50 – a), c), e) it can be stated that the width of the outer brittle ring expands according to the sequence 720+620 / 760 / 870 and matches the extent of plastic scope of the corresponding material in the diagram presented in Figure 47. Also double-step aged and overaged materials demonstrated higher portion of transgranular fracture mode (Figure 50-b and Figure 50-f) as opposed to the prevalent intergranular fracture mode and rather smooth grain surfaces observed on the fracture surface of the heat 760, Figure 50 - d.

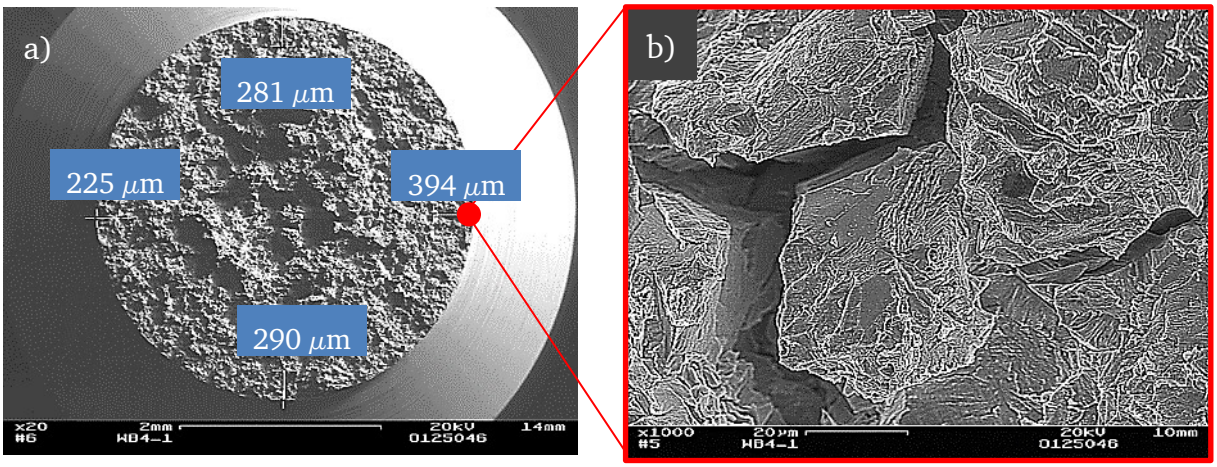

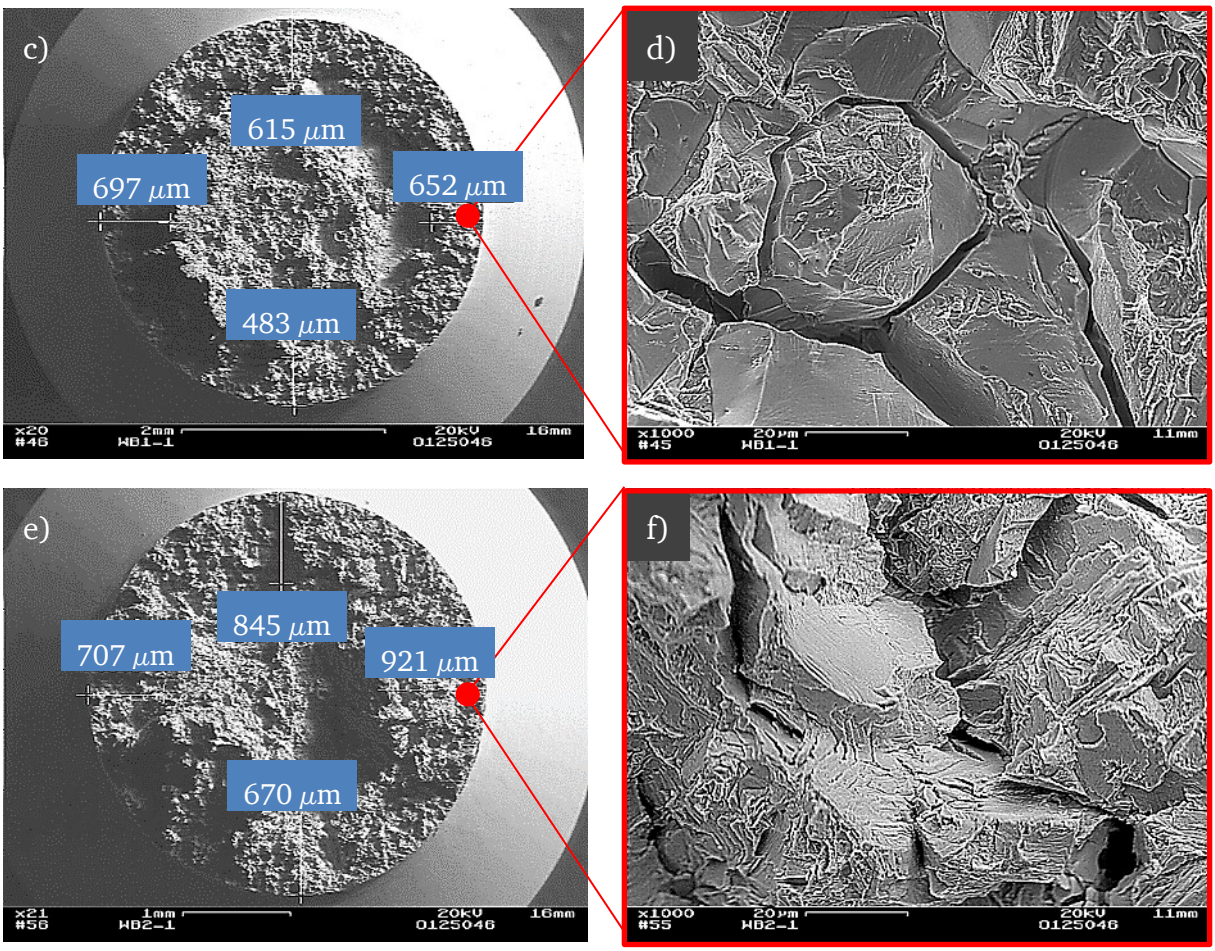

Figure 50: SEM micrographs of fracture surfaces of alloy 718 yielded in SSR tests at a displacement rate 0.2 mm/h under simultaneous hydrogen charging (30 mA/cm² in 1 M $(NH_4)_2SO_4$ at 23°C): a), b) – material variant 720+620 – an overview and detailed view; c), d) – material variant 760 – an overview and detailed view; e), f) – material variant 870 – an overview and detailed view

8.2 Tensile tests at displacement rate (0.2 mm/h) performed on the precharged specimens

The results obtained on the specimens of material heats 760 and 870, charged with hydrogen for 14 days prior to the tensile tests at displacement rate 0.2 mm/h are presented in comparison to the simultaneously charged samples tensioned at the same conditions, Figure 51. The change in the hydrogen charging mode significantly changed the material behavior: only minor reduction in the magnitude of the tensile force and no reduction of the sample could be observed for the precharged specimens.

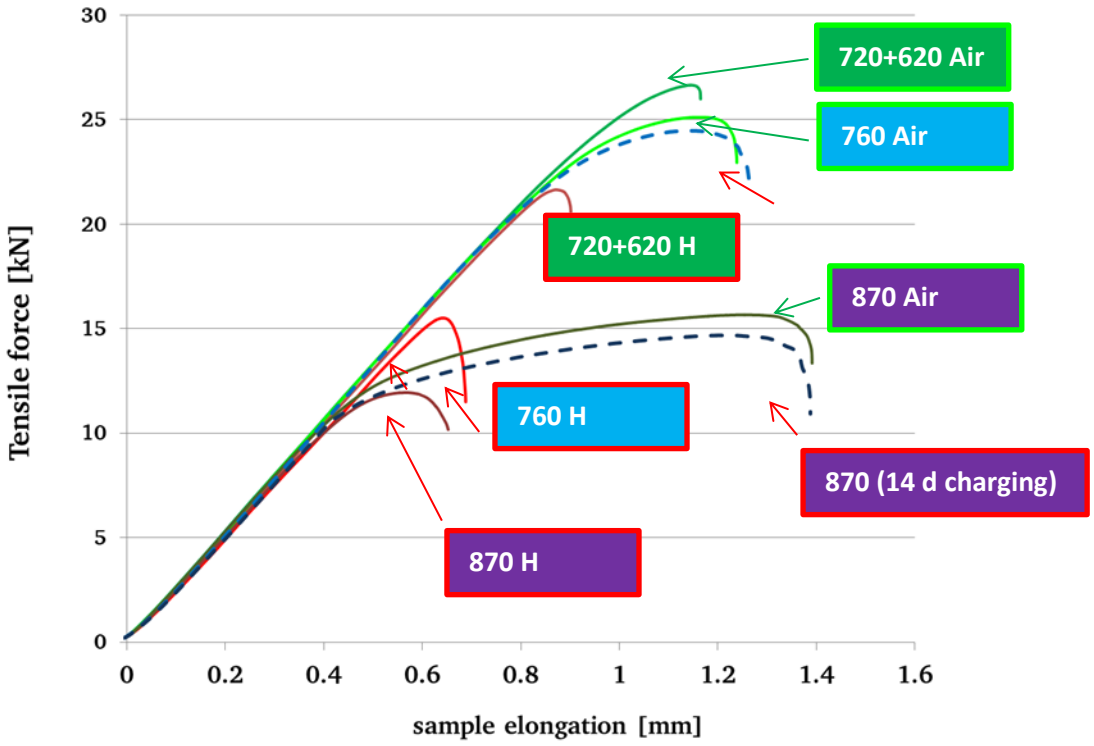

Figure 51: Tensile force - elongation curves of different alloy 718 heats obtained during SSR tests (displacement rate 0.2 mm/h) in air at 23°C (green lines) and under simultaneous hydrogen charging (30 mA/cm² in 1.0 M $(NH_4)_2SO_4$ at 23°C) (red lines) in comparison to the ex-situ charged specimens (dashed blue lines)

Examination of the specimens fracture surfaces via SEM revealed similar arrangements of the brittle and ductile fracture modes as presented in Figure 49. Yet the width of the outer brittle ring appears to be significantly smaller: ca. 100 μm in comparison to ca. 600 μm for the heat 760 and about 220 μm in comparison to ca. 800 μm for 870, Figure 52. Furthermore, the observed fractures are mostly transgranular with minor intergranular features.

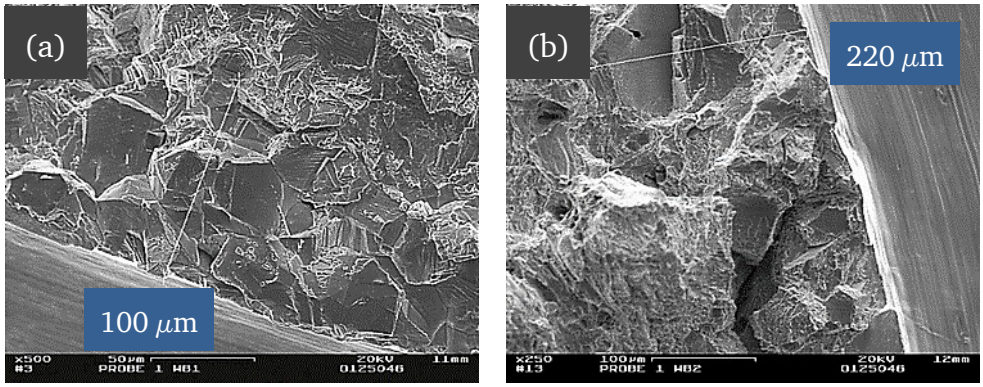

Figure 52: SEM micrographs of fracture surfaces of the aged alloy 718 specimens, precharged with hydrogen for 14 days and tested in a tensile test at displacement rate 0.2 mm/h in air at 23°C: a) detailed view of the outer ring for material 760; b) detailed view of the outer ring for material 870

8.3 Tensile tests at slow displacement rate (0.02 mm/h) under simultaneous cathodic hydrogen charging

The results of the tensile tests carried out at a slower displacement rate (0.02 mm/h) under simultaneous cathodic hydrogen charging are demonstrated in Figure 53. In addition to the variants 720+620, 760 and 870, material heats 775 and 800 were investigated to address the question of the role of the grain boundary δ phase precipitate in the HE failure mechanism.

As expected, samples with the highest hardness (ca. 43 HRC) yield at the highest tensile force. However, this time its total elongation is comparable to less hard material heats, such as material variants 760 or 800. Samples of material 760 reached notch strength level similar to 775, although yielded at slightly reduced elongation. Simultaneous cathodic hydrogen charging of the tensile samples resulted in a distinct differentiation of the material performance in regards to the microstructure variation. Surprisingly, the material heat 760, with the second highest hardness among the chosen material variants, yields at a lower tensile force than the less hard material 775.

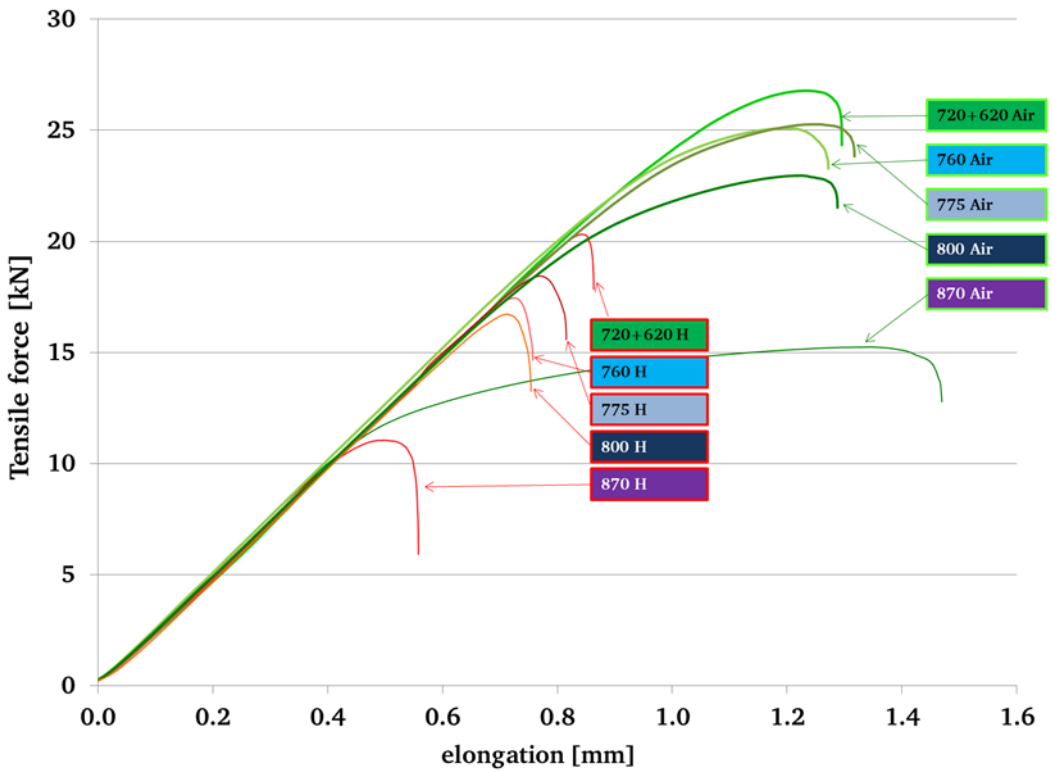

Figure 53: Tensile force - elongation curves of different alloy 718 heats obtained during SSR tests (displacement rate 0.02 mm/h) in air at 23°C (green lines) and under simultaneous hydrogen charging (30 mA/cm² in 1.0 M $(NH_4)_2SO_4$ at 23°C) (red lines)

A comparison of the HE values for each material heat reveals the impact of the aging temperature on the hydrogen embrittlement susceptibility of the material, Figure 54.

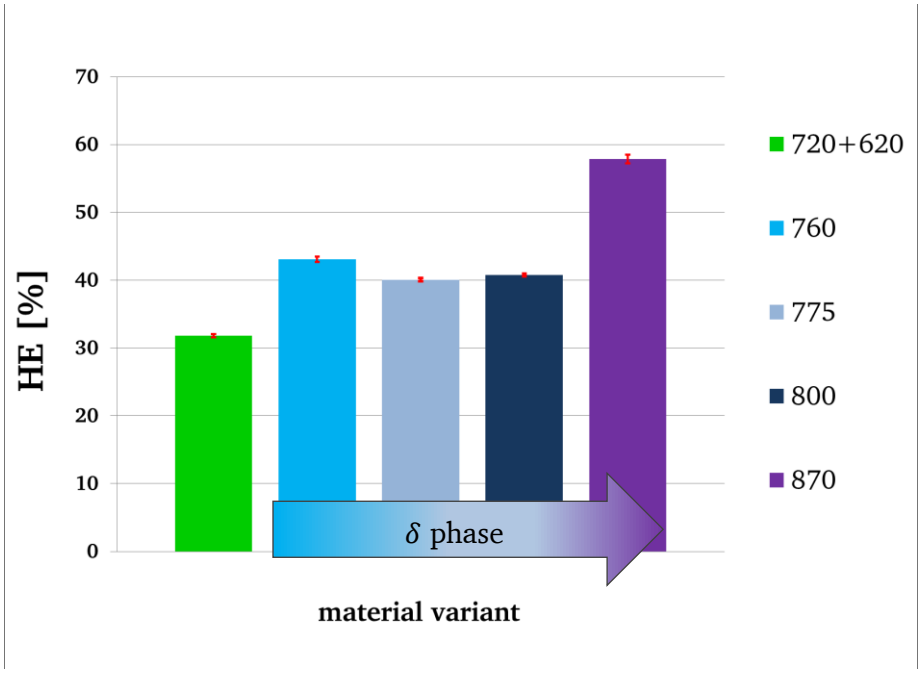

Figure 54: Hydrogen embrittlement susceptibility of aged alloy 718 in regards to the heat treatment temperature

The calculated coefficients of hydrogen embrittlement susceptibility demonstrate no correlation with the estimated amount of δ phase or with the material hardness, which is in agreement with the previous observations. The material with the highest hardness and lowest amount of grain boundary δ phase showed the lowest susceptibility to hydrogen embrittlement, followed by the material 775 with an increased amount of δ. On the other hand, the highest hydrogen embrittlement susceptibility was observed for material variants 760 and 870 with the small and large amount of δ precipitates (0.16 to >>1 particles per micrometer of the grain boundary).

The arrangement of the ductile and brittle fracture modes was observed to be the same as for the specimens tested at a higher displacement rate reported in chapter 8.1, Figure 55.

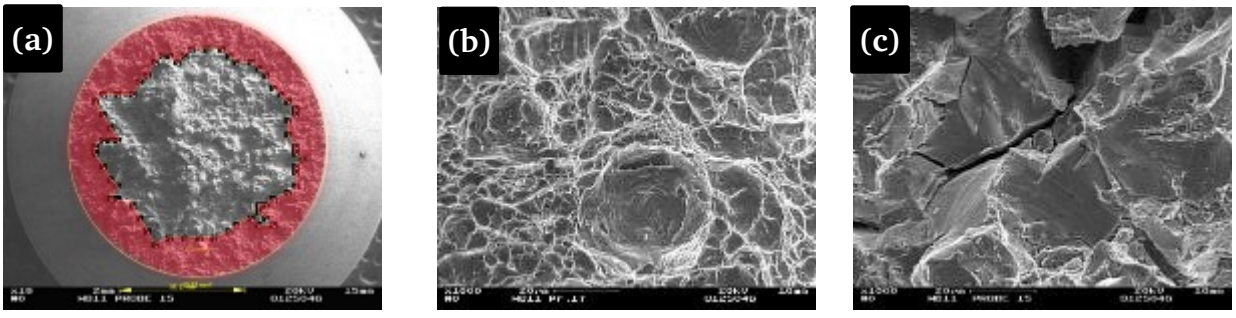

Figure 55: (a) Fracture surface of the aged alloy 718 specimen (775), failed due to the SSR test (0.02 mm/h) under simultaneous cathodic hydrogen charging (30 mA/cm² in 1 M $(NH_4)_2SO_4$) at 23 °C; (b) detailed view of the center area; (c) detailed view of the brittle area, marked with red color in (a)

Fractographic analysis of the brittle area indicated a mixture of intergranular (IG) and

transgranular (TG) fracture modes in all the tested material heats, Figure 56.

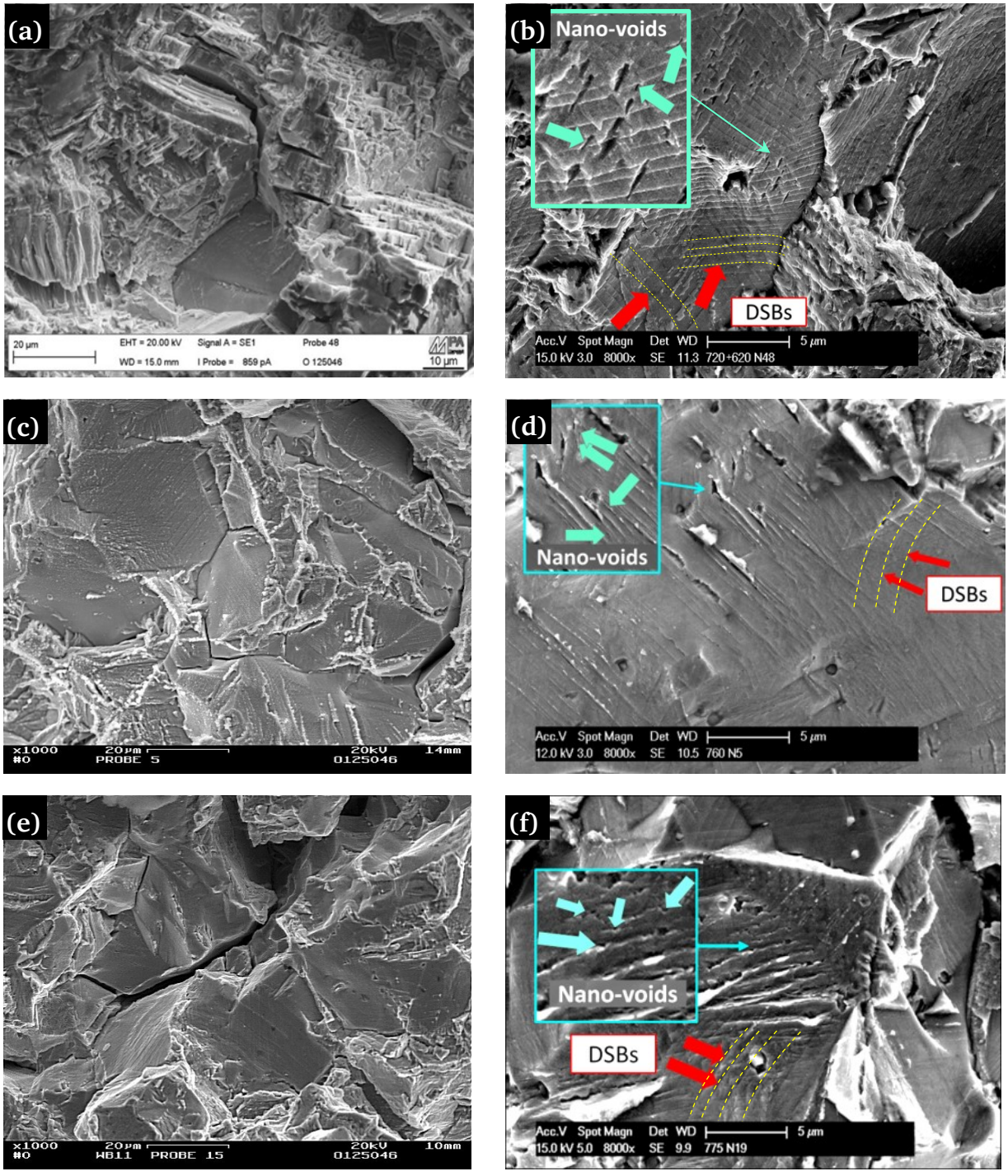

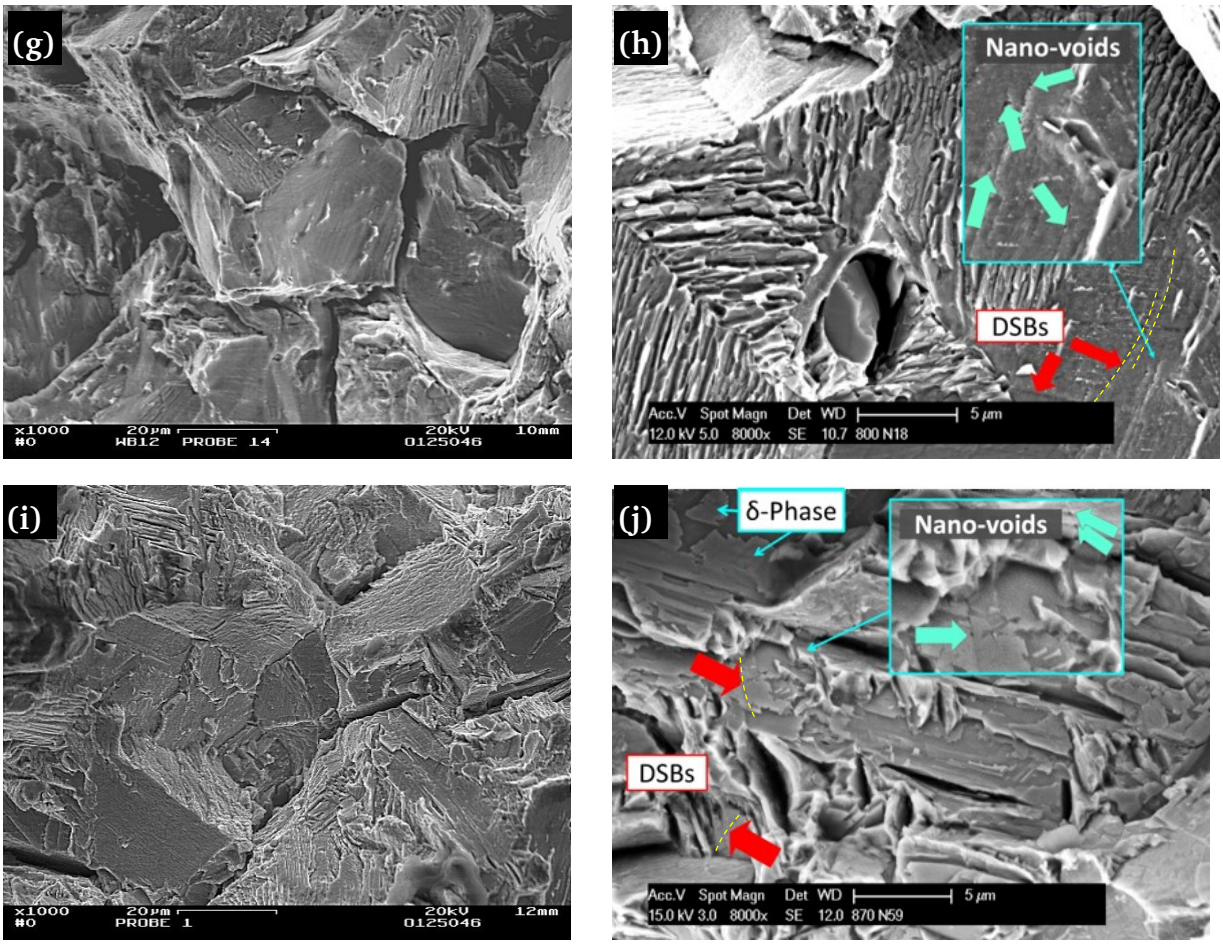

Figure 56: SEM micrographs of the alloy 718 samples yielded in the tensile test at a displacement rate 0.02 mm/h under simultaneous hydrogen charging (30 mA/cm² in 1.0 M $(NH_4)_2SO_4$ at 23°C) : (a) and (b) – 720+620; (c) and (d) – 760; (e) and (f) – 775; (g) and (h) – 800; (i) and (j) – 870

It is well known that alloy 718 deforms by planar slip mode when subjected to a monotonic tensile load at room temperature. Formation of arrays of Dislocation Slip Bands (DSB) on {111} slip planes was observed on the fracture surfaces of all the material heats, tested in air at a displacement rate of 0.02 mm/h, Figure 56. These observations are in agreement with the other reports available for this material, [48], [166], [87]. The appearance of these structures is believed to be a result of a shear localization along the {111} planes, intensified by the slow tension. In the presence of hydrogen the observed DSBs become more distinct and parallel to each other, Figure 56. Nano-voids formed at the intersection of the DSBs were observed for all the material variants, suggesting the HELP to be the main failure mechanism. On the other hand, the SEM micrographs of the longitudinal section of the material 870 demonstrate the change in the fracture mode from IG to TG in the presence of the δ phase, as a result of the HEDE mechanism, Figure 57-b.

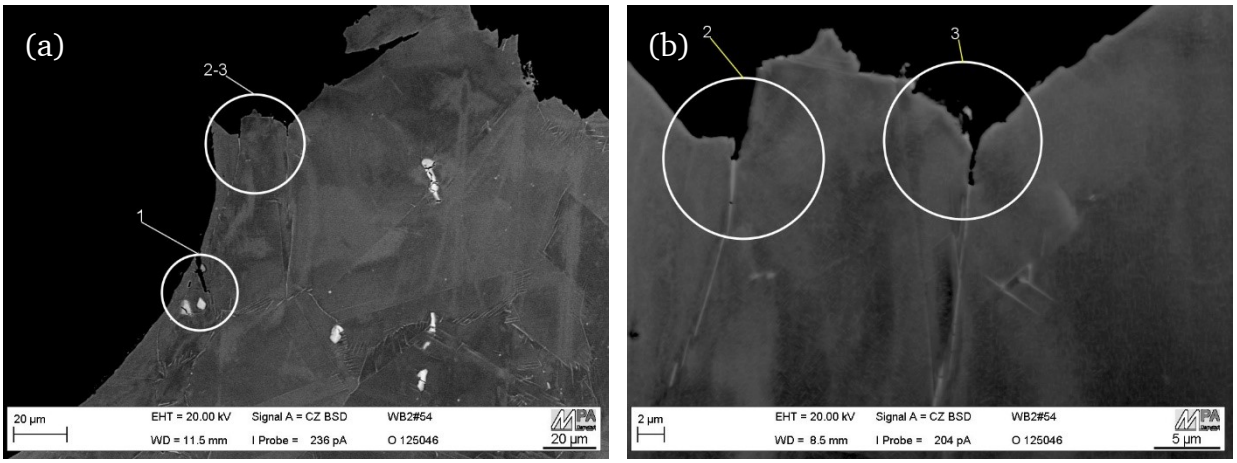

Figure 57: Longitudinal section of round tensile notched sample of the material 870, yielded in the tensile test at a displacement rate 0.02 mm/h under simultaneous hydrogen charging (30 mA/cm² in 1.0 M $(NH_4)_2SO_4$ at 23°C)

8.4 Visualization of the hydrogen path on the fracture surface of the tensioned specimen (0.02 mm/h) under simultaneous hydrogen charging

To address the discrepancies regarding the width of the brittle areas on the fracture surfaces of samples with in-situ and ex-situ hydrogen charging, hydrogen visualization by a silver decoration technique was carried out on one of the samples of the heat 870 after it was tested at a displacement rate of 0.02 mm/h under simultaneous hydrogen charging.

The results of this experiment are presented in Figure 58 and Table 7.

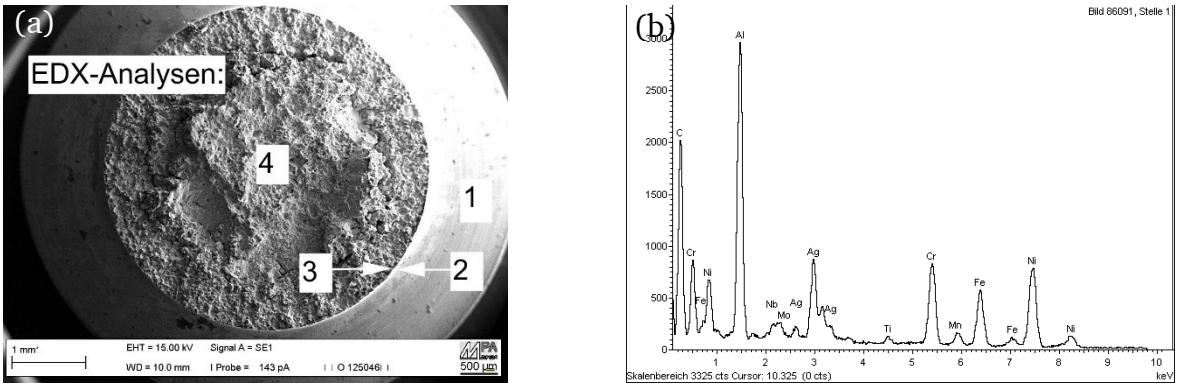

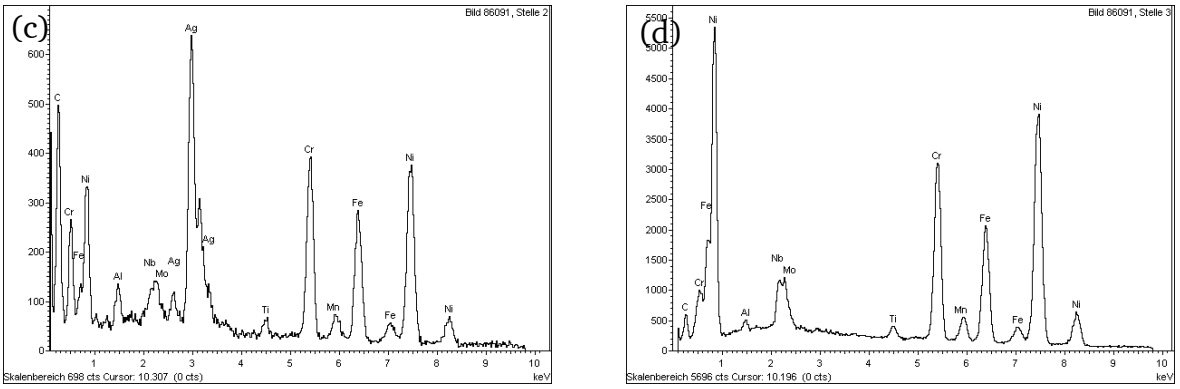

Figure 58: Hydrogen visualization by means of silver decoration carried out on the fracture surface of the material variant 870 tensioned at a displacement rate of 0.02 mm/h under simultaneous hydrogen charging (30 mA/cm² in 1.0 M $(NH_4)_2SO_4$ at 23°C): a) – an overview; b) EDX-spectrum recorded for the position Nr. 1; c) EDX-spectrum recorded for the position Nr. 2; d) EDX-spectrum recorded for the position Nr. 3

Table 9: Particulars to the EDX-spectra presented in Figure 58

	Concentration of the chemical element in wt.-%									
Pos.	C	Al	Ti	Cr	Fe	Ni	Nb	Mo	Ag	Sum
1	46.22	11.94	0.51	8.18	7.05	15.58	1.01	1.09	8.52	100
2	27.70	1,31	0.85	11.68	11.07	23.05	1.71	1.78	20.85	100
3	13.17	0.65	0.84	16.50	14.45	45.59	5.12	3.36	0.33	100

The largest amount of deposited silver was detected on the notch flank, indicating an intensive hydrogen absorption in the surface layer during the experiment, Figure 58-b and Figure 58-c. However, on the fracture surface itself EDX-measurements indicated minor amounts of silver only in the area within the range of 20 μm from the sample surface which corresponds to the grain diameter of the chosen material variant, Figure 58-d. Taking into account that the width of the brittle ring amounts to about 800 μm, it can be stated that the bulk hydrogen most likely did not make a major contribution to the failure mechanism. This conclusion leads to the assumption of hydrogen transport by moving dislocations as the main diffusion mechanism.

8.5 Conclusions to chapter 8

Summarizing the results outlined in the present chapter, it can be said that all of the tested material variants revealed a certain sensitivity to HE under chosen experimental conditions. According to the calculated coefficients of HE susceptibility, the material performance does not strictly correlate with its hardness or with the amount of grain boundary δ phases. Fracture surface documentation was carried out on the hydrogenated samples using SEM. Without any exception, all the material variants revealed ductile micro-void coalescence mode in the center section of the fracture surface and features characteristic for the intergranular and transgranular cracking, located in the outer ring section of the

fracture surface. Detailed SEM examination performed on the intergranular areas of the brittle sections of all the material heats revealed slip traces attributed to the arrays of DSB. Nano-voids formed at the intersection of the DSBs were observed for all the material variants, suggesting the HELP to be the main failure mechanism. The results of the hydrogen visualization experiment performed on the fracture surface of the material 870 support this hypothesis by emphasizing the role of dislocation movement in the process of hydrogen diffusion. SEM observations of the longitudinal section of the material 870 indicate a change of the crack path from intergranular to transgranular mode in the vicinity of the δ phase as a result of HEDE mechanism.

Both HEDE and HELP mechanisms should be considered to explain the hydrogen assisted failure of the alloy 718. The susceptibility of the material is rather correlated with the size and the density of the secondary phase precipitates than with the measured material hardness.

9 Discussion

The experimental results presented in the previous four chapters confirm the strong dependency of the aging procedure for superalloy 718 on its overall corrosion behavior.

Measurements via Scanning Kelvin Probe Force Microscopy revealed the differences in surface potential between the matrix and intermetallic inclusions such as titanium and niobium carbonitrides (Ti, Nb (C,N)) and δ phases to be in the range of 150, 100 and 50 mV, respectively. Thus, these precipitations can be expected to act as a galvanic element and to represent the sites of the preferential localized corrosion attack.

Furthermore, similar potential range for the metastable pit growth observed for different material heats during the long term open circuit potential (OCP) measurements on materials 760 and 870 indicates the same nature of the localized corrosion elements and therefore supports the above stated hypothesis. The SEM and EDX examinations of the samples after the corrosion experiments demonstrated pit initiations taking place in the vicinity of titanium and niobium carbonitrides in case of both material variants. However, no evidence could be found to support the theory of a galvanic corrosion occurring on the matrix/δ phase interface. Since the fraction of carbonitrides is not influenced in the aging temperature range and it is the amount of the δ phase that is of significant difference in the tested material variants, these observation can be regarded as rather contradicting.

On the other hand the potentiodynamic scan measurements performed on the materials heated in the temperature range between 760 and 870 °C demonstrate significant differences in their corrosion performance, which was evaluated by comparison of the breakthrough potentials. These deviations in corrosion behavior can also be attributed to the structural differences in the oxide layers, which were observed by means of X-ray photoelectron spectroscopy (XPS)-measurements performed on material heats 760 and 870. The dependence of the material sensitivity on the pH value of the corrosive electrolyte indicated during potentiodynamic scan measurements implies the importance of the passivation process on the overall performance of the superalloy 718, as the amount of hydronium ions mostly affects the course of the cathodic partial reaction.

Summarizing the results regarding the examinations on the dependency of the corrosion behavior on the microstructure, it can be concluded that titanium and niobium carbonitrides are most likely the root cause of the material corrosion degradation. Yet the observed differences in the material behavior must arise from the variations in the passive film structure and consequently the material's capability to passivate. Examinations of the passivation behavior of superalloy 718 carried out via electrochemical impedance spectroscopy (EIS) demonstrate a significant reduction of the passivation capability in the presence of hydrogen dissolved in the bulk of the material. It was shown that the passive layer

of the heat aged at higher temperature (870) loses its protective features faster, than that of the heat 760. It is conceivable that the depletion of the protective properties due to the hydrogen absorption may be a key factor for the degradation mechanism in hydrogen containing aggressive environments.

The microstructure of superalloy 718 is also found to influence the hydrogen diffusivity and solubility in the material. Hydrogen effective diffusion coefficients measured by means of electrochemical hydrogen permeation experiments on the samples with various grain sizes showed an inverse proportionality to the average grain size. This observation supports the hypothesis of the hydrogen short-cut diffusion path along the grain boundaries of nickel base alloy 718. This kind of hydrogen diffusion behavior is similar to the phenomenon observed in pure nickel specimens. Hydrogen permeation experiments carried out on the aged samples of alloy 718 demonstrated the trapping effect of the secondary phase precipitates such as $\gamma' + \gamma''$ and δ. As the precipitation of carbonitrides is not expected to vary in the aging temperature range, all the differences in the hydrogen permeation behavior can be associated with the changes in the secondary phase precipitation size and volume fraction. Acknowledging the fact that hydrogen diffusion in nickel base alloy 718 occurs primarily along the grain boundaries, it can be assumed that hydrogen trapping would take place on the grain boundary precipitates. These experiments are found to be in agreement with hydrogen contents obtained on the samples with various precipitation morphology by means of carrier gas hot extraction measurements. Measured hydrogen contents appear to be in correlation with the matrix/precipitation surface interface and thus confirm the abovementioned hypothesis.

The experimental results on the HE susceptibility of the nickel base alloy 718 reveal the general sensitivity of the material to the HE. Significant differences in material behavior observed during tests on the precharged versus in-situ charged specimens suggest that the major amount of hydrogen is dragged to the grain boundaries by moving dislocations. Fracture surfaces of the samples tested in air demonstrate the localization of the plastic strain in the slip bands during deformation of the alloy 718. Thus, the total amount of hydrogen transported to the grain boundaries by moving dislocations should be proportional to the number of dislocations situated within the slip band, [190], which after Blankenship et al. [191] should follow the relationship given in (16).

$$N = V^{1/2} r^{1/2} L \frac{C_p}{C_B b} \tag{16}$$

Where V is the volume fraction of shearable precipitates, r is the middle radius of the shearable particle, L is the slip length which can be estimated by the middle grain diameter, b is the burgers vector, and C_p and C_B are related to the APB and the matrix shear

modulus. Since the C_p, C_B and b are assumed to be identical for the different heats of the same material ingot and L is not affected by the aging temperature, all the differences in the number of dislocations, situated within one slip band in case of the chosen material variants should result from the variation of the volume fraction and the average radius of the strengthening phases, i.e. $\gamma' + \gamma''$. Thus, a specific number of dislocations within one slip band, N* can be introduced as

$$N^* = \frac{N}{L \cdot \frac{c_p}{c_b \cdot b}} = V^{1/2} \cdot r^{1/2}$$

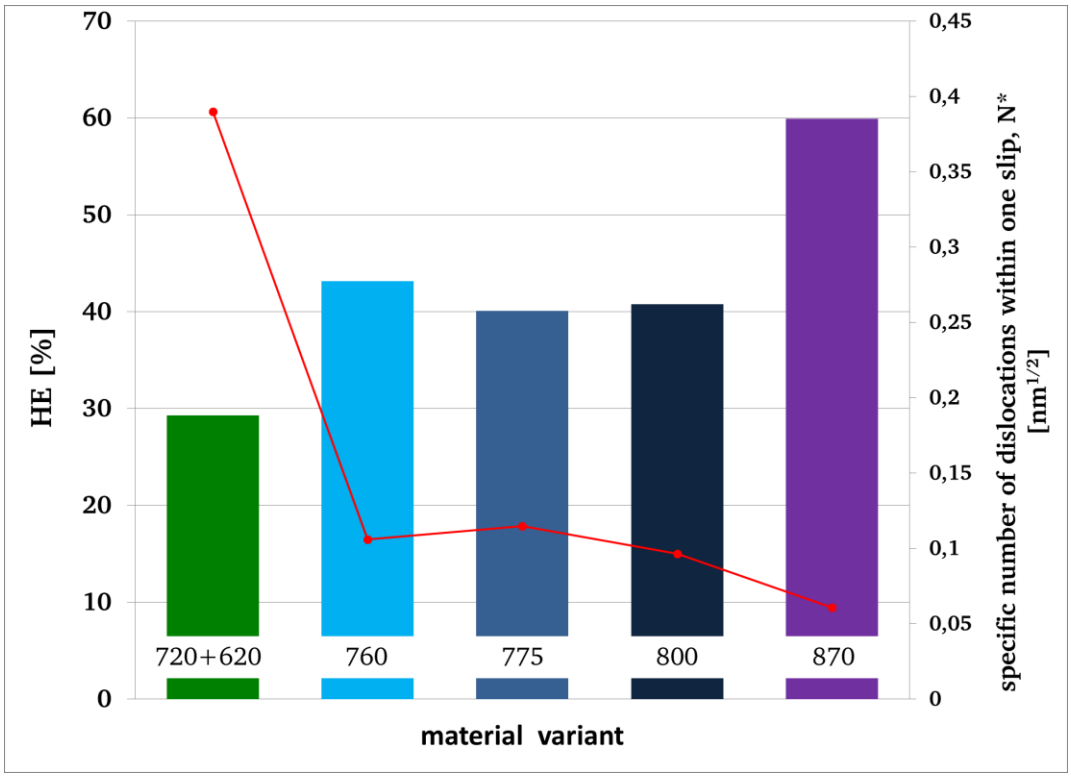

Figure 59: Correlation between the HE susceptibility coefficient and the morphology of the strengthening phase precipitates

Plotting the estimated HE susceptibility coefficients over N*[1] shows the expected inverse correlation and thus supports the suggested hypothesis. For a given chemical composition, the hydrogen embrittlement susceptibility of nickel base alloy 718 is inversely proportional to the square root of the product of the average size and the volume fraction of the strengthening phase precipitations. Thus, it is the morphology of the strengthening phases but not the hardness (as suggested in the specification API 6ACRA) that influence the performance of super alloy 718 under simultaneous hydrogen charging.

[1] The data for the materials 760 and 870 were obtained using the values given in [194]

10 Summary and outlook

Improvement of the material performance in severe corrosion environments is only possible on provision of the optimal microstructure. The knowledge about interactions between corrosive environments and the material microstructure is essential for this purpose. However, available data on the corrosion resistance of alloy 718 in respect to the variation of its microstructure revealed the lack of systematic analysis. To fill this gap, following objectives were set and achieved within the framework of this research project, Table 10.

Table 10: Outline of the main research objectives of this work

Research objective 1: Characterisation of the material properties in regards to the aging procedure
✓ It was possible to **quantitatively characterize** the material microstructure in regards to the **content of δ phase**, **size and fraction of $\gamma' + \gamma''$** precipitates
✓ **Local potential differences** between the matrix and secondary phase precipitates (**δ phase and Ti,Nb(C,N)**) were successfully measured via SKPFM
✓ Qualitative **differences in the oxide film structures** of the different material variants could be detected by means of XPS measurements
✓ The **decrease of materials strength and hardness with the increasing age hardening temperature**, caused by the coarsening of the strengthening $\gamma' + \gamma''$ precipitates was documented
Research objective 2: Evaluation of the interaction between the material microstructure and its corrosion resistance
✓ Slight **correlation between the age hardening temperature and material corrosion resistance** was identified
✓ Impact of the **alloy microstructure on the hydrogen diffusivity and solubility** was identified
✓ **Synergistic interactions between the hydrogen**, dissolved in the microstructure of alloy 718 **and the material corrosion resistance** were studied **in regards to the material microstructure**
✓ **Hydrogen embrittlement susceptibility of alloy 718** was evaluated **in regards to the material microstructure**

The original contribution to knowledge of this work is linking of the heat treatment dependent properties of alloy 718 with the course of action of the particular damage processes representing single sub processes of the material degradation due to the SCC, Figure 60.

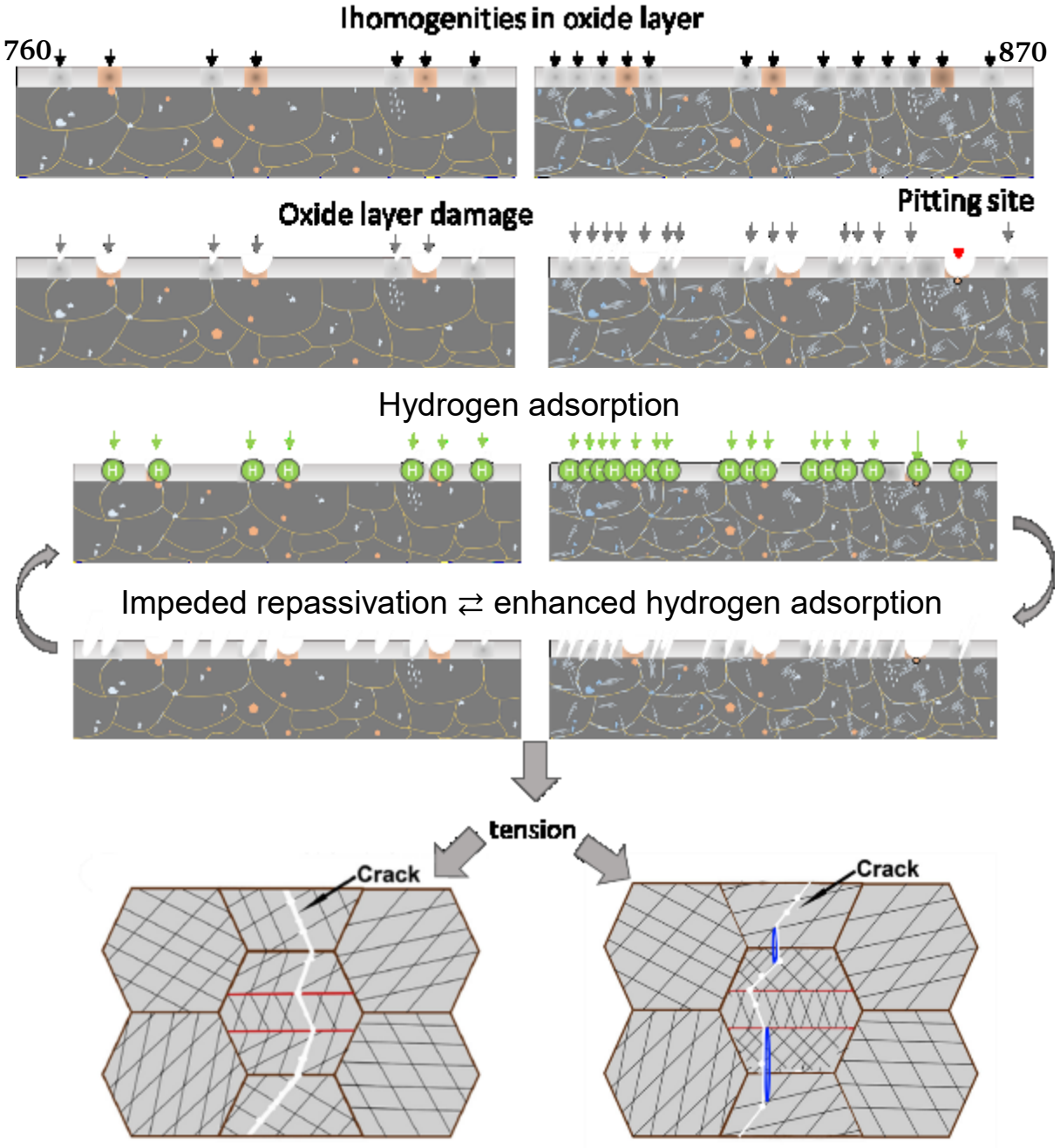

Figure 60: Proposed damage mechanism for alloy 718

Considering the experimentally obtained data on the material performance regarding its microstructure, the observed differences in corrosion behavior could be attributed to the alterations of the oxide layers structure caused by the variation of the aging temperature.

Local damage of the protective film would lead to an increased hydrogen adsorption and, as a result, impeded re-passivation capability of the material. This in turn would further increase the hydrogen adsorption, and so on. In the presence of local plastic deformation, the adsorbed hydrogen interacts with dislocations according to the HELP theory, causing the material to fail at a reduced elongation. The experimental observations evidence for the δ phase and carbonitrides contribution to HEDE failure mechanism. Therefore, it can be recommended to adjust the manufacturing process in order to reduce the amount of these precipitates. Further, HE susceptibility coefficients were found to be in a strong correlation with the morphology of the $\gamma' + \gamma''$phase precipitates. Although the double-step aged material 720+620 would not pass the restrictions of the NACE MR0175 specification due to its hardness, the hydrogen embrittlement susceptibility of this heat was measured to be the lowest among all the tested material variants. Thus, a revision of the specification might be worth consideration.

Based on the findings following directions for the future research might be suggested:

- Formation of the passive and reaction layer on the material surface depending on the chosen aging temperature and their interactions with hydrogen
- Effects of the size and volume fraction of the strengthening phase precipitation on the localization of the shear stress in the slip bands and their interaction with hydrogen.

For the first point, a systematic study of the oxide layers by means of Secondary Ion Mass Spectrometry complemented by Atom Probe Tomography measurements would probably be the most promising approach. As regards for the reaction layer, i.e. the salt film, built on the metal surface due to the chemical reaction of the oxide layer with the corrosive environment, there are some reports of the successful deployment of the Auger electron spectrometry for this purpose, [192].

Microscale tensile tests on the hydrogenated samples performed under in-situ microscope observations similar to [193] or in-situ electrochemical nanoindentation experiments [194] might provide the necessary insight about the interaction processes between the strengthening intermetallic phases, dislocations and hydrogen. Further, the recent experiments on the strengthening mechanism by $\gamma' + \gamma''$phases imply certain alteration processes resulting from the dislocation cutting and the consequent localization of the shear

stress. The results of this work emphasize the importance of the shear stress localization and planar slip for the degradation mechanism of alloy 718. Since the width of slip bands is believed to depend on the microstructural features [195], a systematic study of the slip band width alteration might be helpful for the understanding of degradation mechanisms in correlation with the material microstructure.

Bibliography

[1] S. A. Holditch and R. R. Chianelli, “Factors That Will Influence Oil and Gas Supply and Demand in the 21st Century,” *MRS Bulletin*, vol. 33, no. 04, pp. 317–323, 2008.

[2] J. Ward, “High Performance Age Hardenable Nickel Alloys Solve Problems in Sour Oil and Gas Service,” *Offshore World*, no. November, pp. 43–47, 2010.

[3] O. G. Helmuth Sarmiento Klapper, Jutta Klöwer, “Hydrogen embrittlement - the game changing factor on the applicability of Nickel based alloys in oilfield technology,” *Philosophical Transactions of the Royal Society A: Mathematical, Physical and Engineering Sciences*, no. April, pp. 1–22, 2015.

[4] S. Mannan and S. Patel, “A NEW HIGH STRENGTH CORROSION RESISTANT ALLOY FOR,” *NACE Corrosion*, vol. 718, no. 6, 2008.

[5] C. Zhou, S. Zheng, C. Chen, and G. Lu, “The effect of the partial pressure of H2S on the permeation of hydrogen in low carbon pipeline steel,” *Corrosion Science*, vol. 67, pp. 184–192, 2013.

[6] M. Ziomek-Moroz, “Environmentally Assisted Cracking of Drill Pipes in Deep Drilling Oil and Natural Gas Wells,” *Journal of Materials Engineering and Performance*, vol. 21, no. June, pp. 1061–1069, May 2011.

[7] “NACE MR0175-2002, MR0175/ISO 15156,” pp. 650–658, 2003.

[8] S. Ghosh, S. Yadav, and G. Das, “Study of standard heat treatment on mechanical properties of Inconel 718 using ball indentation technique,” *Materials Letters*, vol. 62, no. 17–18, pp. 2619–2622, Jun. 2008.

[9] P. E. Rashmi, B; Bhavsar, “Use of Alloy 718 and 725 in Oil and Gas Industry,” *Superalloys 718, 625, 706 and Various Derivatives (2001)*, pp. 47–55, 2001.

[10] R. M. Latanision, “Physical metallurgy of nickel-base alloys as it relates to corrosion,” *Journal of Materials Engineering*, vol. 10, no. 2, pp. 143–162, Jun. 1988.

[11] N. Sridhar, “Hydrogen Absorption and Embrittlement of Candidate Container Materials,” 1991.

[12] L. Liu *et al.*, “Effect of delta phase on hydrogen embrittlement of inconel 718 by notch tensile tests,” *J. Mater. Sci. Technol.*, vol. 47, no. 2, pp. 355–367, Feb. 2005.

[13] M. G. Burke, T. R. Mager, M. T. Miglin, and J. L. Nelson, “The Effect of Thermal Treatment on SCC of Alloy 718: A Structure - Properties Study,” *superalloys 718, 625, 706 and Various Derivatives*, pp. 763–773, 1994.

[14] R. A. Carneiro, R. C. Ratnapuli, and V. de Freitas Cunha Lins, “The influence of chemical composition and microstructure of API linepipe steels on hydrogen induced cracking and sulfide stress corrosion cracking,” *Materials Science and Engineering: A*, vol. 357, no. 1–2, pp. 104–110, Sep. 2003.

[15] S. A. Mccoy, B. C. Puckett, and E. L. Hibner, “High Performance Age-Hardenable Nickel Alloys Solve Problems in Sour Oil and Gas Service.”

[16] A. Mathiazhagan, “Corrosion Management for effective mitigation of corrosion in Ships - Overview,” vol. 12, pp. 1–5, 2011.

[17] API, “API Standard 6A718, Nickel Base alloy 718 (UNS N07718) for Oil and Gas Drilling and Production Equipment, 2nd Edition, December 2009,” no. December, 2009.

[18] D. F. Paulonis and J. J. Schirra, “Alloy 718 at Pratt & Whitney–Historical Perspective and Future Challenges,” *Superalloys*, vol. 718, no. 625,706, pp. 13–23, 2001.

[19] O. Golenishcheva, G. Andersohn, M. Oechsner, and M. P. A. Ifw, “Hydrogen Diffusion Mechanism in Nickel Base Alloy 718,” in *EUROCORR 2014*, 2014, pp. 4–5.

[20] J. W. Brooks and P. J. Bridges, “Metallurgical Stability of Inconel Alloy 718,” in *Superalloys 1988 (Sixth International Symposium)*, 1988, pp. 33–42.

[21] ASTM, “ASTM E112-13: Standard Test Methods for Determining Average Grain Size,” *ASTM International*, pp. 1–28, 2013.

[22] S. J. Patel and G. D. Smith, “THE ROLE OF NIOBIUM IN WROUGHT SUPERALLOYS.”

[23] F. Cortial, J. M. Corrieu, and C. Vernot-Loier, “Influence of heat treatments on microstructure, mechanical properties, and corrosion resistance of weld alloy 625,” *Metallurgical and Materials Transactions A*, vol. 26, no. 5, pp. 1273–1286, May 1995.

[24] G. D. Smith and S. J. Patel, “The Role of Niobium in Wrought Precipitation-Hardened Nickel-Base Alloys,” *Superalloys 718, 625, 706 and Various Derivatives (2005)*, pp. 135–154, 2005.

[25] M. Sundararaman, P. Mukhopadhyay, and S. Banerjee, “Precipitation of the Delta-Ni3Nb Phase in Two Nickel Base Superalloys,” *Metallurgical Transactions A*, vol. 19, no. March, pp. 453–465, 1988.

[26] A. Devaux *et al.*, “Gamma double prime precipitation kinetic in Alloy 718,” *Materials Science and Engineering: A*, vol. 486, no. 1–2, pp. 117–122, Jul. 2008.

[27] H. T. Lee and S. W. Lee, “The morphology and formation of gamma prime in nickel-base superalloy,” *Journal of Materials Science Letters*, vol. 9, no. 5, pp. 516–517, May 1990.

[28] L. Liu, C. Zhai, C. Lu, W. Ding, A. Hirose, and K. F. Kobayashi, “Study of the effect of δ phase on hydrogen embrittlement of Inconel 718 by notch tensile tests,” *Corrosion Science*, vol. 47, no. 2, pp. 355–367, Feb. 2005.

[29] J. M. Oblak, D. F. Paulonis, and D. S. Duvall, “Coherency strengthening in Ni base alloys hardened by DO22 gamma” precipitates,” *Metallurgical Transactions*, vol. 5, no. January, pp. 143–153, 1974.

[30] S. Fujuyama and K. Yokogawa, “γ′Precipitate in Inconel 718,” *J. Mater. Sci. Technol.*, vol. 10, pp. 293–303, 1994.

[31] D. Jianxin, X. Xishan, and Z. Shouhua, “COARSENING BEHAVIOR OF y ” PRECIPITATES IN,” *scripta metallurgica et Materialia*, vol. 33, no. 12, pp. 1933–1940, 1995.

[32] S. Zhao, X. Xie, G. D. Smith, and S. J. Patel, “Gamma prime coarsening and age-hardening behaviors in a new nickel base superalloy,” *Materials Letters*, vol. 58, no. 11, pp. 1784–1787, Apr. 2004.

[33] C. Slama, C. Servant, and G. Cizeron, “Aging of the Inconel 718 alloy between 500 and 750 °C,” *Journal of Materials Research*, vol. 12, no. 09, pp. 2298–2316, 1997.

[34] C. Slama and M. Abdellaoui, “Structural characterization of the aged Inconel 718,” *Journal of Alloys and Compounds*, vol. 306, no. 1–2, pp. 277–284, Jun. 2000.

[35] J. H. Du, X. D. Lu, Q. Deng, J. L. Qu, J. Y. Zhuang, and Z. Y. Zhong, “High-temperature structure stability and mechanical properties of novel 718 superalloy,” *Materials Science and Engineering: A*, vol. 452–453, pp. 584–591, Apr. 2007.

[36] T. Alam, M. Chaturvedi, S. P. Ringer, and J. M. Cairney, “Precipitation and clustering in the early stages of ageing in Inconel 718,” *Materials Science and Engineering A*, vol. 527, no. 29–30, pp. 7770–7774, 2010.

[37] H.-T. Lee and W.-H. Hou, “Development of fine-grained structure and the mechanical properties of nickel-based Superalloy 718,” *Materials Science and Engineering: A*, vol. 555, pp. 13–20, Jun. 2012.

[38] M. K. Miller, S. S. Babu, and M. G. Burke, “Intragranular precipitation in alloy 718,” *Material Science and Engineering*, vol. 270, no. 1999, pp. 14–18, 2008.

[39] H. Guo, M. C. Chaturvedi, N. L. Richards, and G. S. McMahon, “Interdependence of character of grain boundaries, intergranular segregation of boron and grain boundary liquation in simulated weld heat-affected zone in inconel 718,” *Scripta Materialia*, vol. 40, no. 3, pp. 383–388, Jan. 1999.

[40] J. He, X. Y. Tang, S. Fukuyama, and K. Yokogawa, “Boundary in Y" Precipitates in INCONEL 718 nickel-base superalloy,” *Acta metall. mater*, vol. 43, no. 12, pp. 4403–4409, 1995.

[41] M. C. Chaturvedi and Y. Han, “Strengthening mechanisms in Inconel 718 superalloy,” *Metal Science*, vol. 17, no. 3, pp. 145–149, Mar. 1983.

[42] C. Slama, C. Servant, and G. Cizeron, “Aging of the Inconel 718 alloy between 500 and 750 °C,” *Journal of Materials Research*, vol. 12, no. 09, pp. 2298–2316, 1997.

[43] L. Whitmore and E. Al., “Transmission electron microscopy of single and double aged 718Plus superalloy,” *Materials Science and Engineering: A*, vol. 534, pp. 413–423, Feb. 2012.

[44] L. Viskari and K. Stiller, “Atom probe tomography of Ni-base superalloys Allvac 718Plus and Alloy 718,” *Ultramicroscopy*, vol. 111, no. 6, pp. 652–658, 2011.

[45] L. Viskari, Y. Cao, M. Norell, G. Sjöberg, and K. Stiller, “Grain boundary

microstructure and fatigue crack growth in Allvac 718Plus superalloy," *Materials Science and Engineering A*, vol. 528, no. 6, pp. 2570–2580, 2011.

[46] A. K. Roy and A. Venkatesh, "Evaluation of yield strength anomaly of Alloy 718 at 700–800°C," *Journal of Alloys and Compounds*, vol. 496, no. 1–2, pp. 393–398, Apr. 2010.

[47] D. Cai, W. Zhang, P. Nie, W. Liu, and M. Yao, "Dissolution kinetics of δphase and its influence on the notch sensitivity of Inconel 718," *Materials Characterization*, vol. 58, no. 3, pp. 220–225, Mar. 2007.

[48] K. J. Leonard, M. N. Gussev, J. N. Stevens, and J. T. Busby, "Analysis of stress corrosion cracking in alloy 718 following commercial reactor exposure," *Journal of Nuclear Materials*, vol. 466, pp. 443–459, 2015.

[49] D. H. Ping, Y. F. Gu, C. Y. Cui, and H. Harada, "Grain boundary segregation in a Ni–Fe-based (Alloy 718) superalloy," *Materials Science and Engineering: A*, vol. 456, no. 1–2, pp. 99–102, May 2007.

[50] J. J. M. Jebaraj, D. J. Morrison, and I. I. Suni, "Hydrogen diffusion coefficients through Inconel 718 in different metallurgical conditions," *Corrosion Science*, vol. 80, pp. 517–522, Mar. 2014.

[51] Z. F. Yin, W. Z. Zhao, W. Y. Lai, and X. H. Zhao, "Electrochemical behaviour of Ni-base alloys exposed under oil/gas field environments," *Corrosion Science*, vol. 51, no. 8, pp. 1702–1706, 2009.

[52] H. Kaesche, *Corrosion of Metals*. Berlin, Heidelberg: Springer Berlin Heidelberg, 2003.

[53] A. Lasia, "Applications of Electrochemical Impedance Spectroscopy to Hydrogen Adsorption, Evolution and Absorption into Metals," *Modern Aspects of Electrochemistry*, vol. 35, pp. 1–49, 2002.

[54] C. Gabrielli, G. Maurin, L. Mirkova, H. Perrot, and B. Tribollet, "Transfer function analysis of hydrogen permeation through a metallic membrane in a Devanathan cell. I. Theory," *Journal of Electroanalytical Chemistry*, vol. 590, no. 1, pp. 1–14, May 2006.

[55] G. Zheng, B. N. Popov, and R. E. White, "Hydrogen-Atom Direct-Entry Mechanism into Metal Membranes," *Journal of The Electrochemical Society*, vol. 142, no. 1, p. 154, 1995.

[56] Fukai, *The Metal-Hydrogen System. Basic Bulk Properties*, Second, Re. .

[57] S. Frappart, X. Feaugas, J. Creus, F. Thebault, L. Delattre, and H. Marchebois, "Study of the hydrogen diffusion and segregation into Fe–C–Mo martensitic HSLA steel using electrochemical permeation test," *Journal of Physics and Chemistry of Solids*, vol. 71, no. 10, pp. 1467–1479, Oct. 2010.

[58] J. A. Fenske, "Microstructure and hydrogen induced failure mechanisms in iron-nickel weldments," Univeristy of Illinois at Urbana-Champaign, 2010.

[59] D. Pérez Escobar, K. Verbeken, L. Duprez, and M. Verhaege, “Evaluation of hydrogen trapping in high strength steels by thermal desorption spectroscopy,” *Materials Science and Engineering: A*, vol. 551, pp. 50–58, Aug. 2012.

[60] L. W. Tsay, M. Y. Chi, Y. F. Wu, J. K. Wu, and D.-Y. Lin, “Hydrogen embrittlement susceptibility and permeability of two ultra-high strength steels,” *Corrosion Science*, vol. 48, no. 8, pp. 1926–1938, Aug. 2006.

[61] F. Lecoester, J. Che, and D. Noel, “Hydrogen embrittlement of the Ni-base Alloy 600 correlated with hydrogen transport by dislocations,” *Material Science and Engineering*, vol. 262, pp. 173–183, 1999.

[62] J. K. Tien, A. W. Thompson, and I. M. Bernstein, “Hydrogen Transport by Dislocations,” *meatllurgical Transactions A*, vol. 7A, no. June, pp. 821–829, 1976.

[63] A. H. Cottrell, “Dislocation theory of yielding and strain ageing of iron.,” *Proc. Phys. Soc. London Sec. A*, vol. 62, no. 48, pp. 49–62, 1949.

[64] C. Borchers, T. Michler, and A. Pundt, “Effect of Hydrogen on the Mechanical Properties of Stainless Steels,” *Advanced Engineering Materials*, vol. 10, no. 1–2, pp. 11–23, Feb. 2008.

[65] J. Kolts and N. Sridhar, “Environmental Embrittlement of Nickel and Nickel-Base Alloys An Analogy to Steels and Austenitic Stainless Steels,” *J. Materials for Energy Systems*, vol. 8, no. 3, pp. 306–318, 1986.

[66] F. Foct, T. Magnin, and O. Bouvier, “Stress corrosion cracking mechanisms of alloy 600 polycrystals and single crystals in primary water—Influence of hydrogen,” *Metallurgical and Materials Transactions A*, vol. 31, no. 8, pp. 2025–2036, Aug. 2000.

[67] R. H. Jones, *Environmental Effects on Engineered Materials*. New York, Basel: Marcel Dekker, Inc., 2001.

[68] R. N. Parkins, “Current Understanding of Stress-Corrosion Cracking,” no. December, 1992.

[69] N. Eliaz, A. Shachar, B. Tal, and D. Eliezer, “Characteristics of hydrogen embrittlement , stress corrosion cracking and tempered martensite embrittlement in high-strength steels,” *Engineering Failure Analysis*, vol. 9, pp. 167–184, 2002.

[70] A. P. Jivkov, “Stress corrosion cracking as evolving interface problem,” *Corrosion*, vol. 2, pp. 79–85, 2004.

[71] H.-J. Bargel and G. Schulze, *Werkstoffkunde*. 2012.

[72] D. S. Morton, S. A. Attanasio, G. A. Young, P. L. Andresen, and T. M. Angeliu, “LM-00K059 The Influence of Dissolved Hydrogen on Nickel Alloy SCC : A Window to Fundamental Insight,” 2000.

[73] F. P. Ford, “Current understanding of the mechanisms of stress corrosion and corrosion fatigue.,” *Environment-sensitive fracture: evaluation and comparison of test methods*, pp. 32–51, 1984.

[74] Y. Z. Jia, H. Li, N. N. Hu, Q. Y. Wang, and J. Q. Wang, "Comparative assessment of near-neutral pH stress corrosion cracking resistance of pipeline steels with different strength," *Materials and Corrosion*, vol. 66, no. 11, pp. 1250–1254, 2015.

[75] ASTM International, "ASTM F2078-15 - Standard Terminology Relating to Hydrogen Embrittlement Testing," no. G 15, pp. 1–5, 2014.

[76] I. M. Robertson *et al.*, "Hydrogen Embrittlement Understood," *Metallurgical and Materials Transactions A*, vol. 46, no. 6, pp. 2323–2341, Jun. 2015.

[77] J. Song and W. a. Curtin, "A nanoscale mechanism of hydrogen embrittlement in metals," *Acta Materialia*, vol. 59, no. 4, pp. 1557–1569, Feb. 2011.

[78] M. L. Martin, J. A. Fenske, G. S. Liu, P. Sofronis, and I. M. Robertson, "On the formation and nature of quasi-cleavage fracture surfaces in hydrogen embrittled steels," *Acta Materialia*, vol. 59, no. 4, pp. 1601–1606, 2011.

[79] T. Neeraj, R. Srinivasan, and J. Li, "Hydrogen embrittlement of ferritic steels: Observations on deformation microstructure, nanoscale dimples and failure by nanovoiding," *Acta Materialia*, vol. 60, no. 13–14. pp. 5160–5171, 2012.

[80] F. Galliano, E. Andrieu, C. Blanc, J. M. Cloue, D. Connetable, and G. Odemer, "Effect of trapping and temperature on the hydrogen embrittlement susceptibility of alloy 718," *Materials Science and Engineering A*, vol. 611, pp. 370–382, 2014.

[81] V. Demetriou, "THE EFFECT OF MICROSTRUCTURE ON THE PERFORMANCE OF NICKEL BASED ALLOYS FOR USE IN OIL AND GAS APPLICATIONS," 2016.

[82] X. Li, Y. Wang, P. Zhang, B. Li, X. Song, and J. Chen, "Effect of pre-strain on Hydrogen embrittlement of High strength steels," *Materials Science and Engineering: A*, vol. 616, pp. 116–122, 2014.

[83] L. Fournier, D. Delafosse, and T. Magnin, "Cathodic hydrogen embrittlement in alloy 718," *Materials Science and Engineering: A*, vol. 269, no. 1–2, pp. 111–119, Aug. 1999.

[84] P. J. Ferreira, I. M. Robertson, and H. K. Birnbaum, "Hydrogen effects on the interaction between dislocations," *Acta Materialia*, vol. 46, no. 5, pp. 1749–1757, Mar. 1998.

[85] D. Delafosse and T. Magnin, "Hydrogen induced plasticity in stress corrosion cracking of engineering systems," vol. 68, 2001.

[86] D. P. Abraham and C. J. Altstetter, "Hydrogen-Enhanced Localization of Plasticity in an Austenitic Stainless Steel," *Metallurgical and materials Transactions A*, vol. 26, no. November, 1995.

[87] Z. Zhang, G. Obasi, R. Morana, and M. Preuss, "Hydrogen assisted crack initiation and propagation in a nickel-based superalloy," *Acta Materialia*, vol. 113, pp. 272–283, 2016.

[88] Strattmann, *Encyclopedia of Electrochemistry, Volume 4, Corrosion and Oxide Films*,

2. Wiley-VCH, 2003.

[89] B. G. Pound, “The effect of aging on hydrogen trapping in precipitation-hardened alloys,” *Corrosion Science*, vol. 42, 2000.

[90] A. Turnbull, “2009 W . R . Whitney Award Lecture : Local Hydrogen Generation and Its Impact on Environment-Assisted Cracking and Crevice Corrosion,” *Corrosion*, vol. 66, no. 5, pp. 1–11, 2010.

[91] T. A. Suter, “Mikroelektrochemische Untersuchungen bei austenitischen ‘rostfreien’ Stählen,” Eidgenössische technische Hochschule Zürich, 1997.

[92] J. W. Oldfield, “Test techniques for pitting and crevice corrosion resistance of stainless steels and nickel-base alloys in chloride-containing environments,” *International Material Reviews*, vol. 32, no. 3, 1987.

[93] N. J. J. Laycock and R. C. C. Newman, “Localised dissolution kinetics, salt films and pitting potentials,” *Corrosion Science*, vol. 39, no. 10–11, pp. 1771–1790, 1997.

[94] J. Soltis, “Passivity breakdown, pit initiation and propagation of pits in metallic materials - Review,” *Corrosion Science*, vol. 90, pp. 5–22, 2015.

[95] H. Kaesche, “Die Passivität der Metalle,” in *Die Korrosion der Metalle*, Berlin, Heidelberg: Springer Berlin Heidelberg, 2011, pp. 198–269.

[96] Q. Yang, “Effect of Hydrogen on Passivity and Corrosion Related Behavior of Austenitic Stainless Steels,” Edmonton, Alberta, 2000.

[97] J. Chêne and a. M. Brass, “Role of temperature and strain rate on the hydrogen-induced intergranular rupture in alloy 600,” *Metallurgical and Materials Transactions A*, vol. 35, no. February, pp. 457–464, 2004.

[98] N. Amokrane, C. Gabrielli, E. Ostermann, and H. Perrot, “Investigation of hydrogen adsorption-absorption on iron by EIS,” *Electrochimica Acta*, vol. 53, pp. 700–709, 2007.

[99] F. Arjmand and A. Adriaens, “Microelectrochemical Investigation of the Effect of Cathodic Polarisation on the Corrosion Resistance of 304L Stainless Steel in a 1 M NaCl Solution,” *International Journal of Electrochemical Science*, vol. 7, pp. 8007–8019, 2012.

[100] A. Ejaz *et al.*, “The effects of hydrogen on anodic dissolution and passivation of iron in alkaline solutions,” *Corrosion Science*, vol. 101, pp. 165–181, 2015.

[101] O. Golenishcheva, M. Oechsner, G. Andersohn, J. Kloewer, and A. Aghajani, “Influence of Delta-phase Precipitation on the Pitting Performance of UNS (N07718),” in *Corrosion 2014*, 2014, no. 3895, pp. 1–15.

[102] G. D. Smith, “Corrosion Resistance of Nickel-Containing Alloys in Petrochemical Environments.”

[103] G. a. Young and J. R. Scully, “Evidence that carbide precipitation produces hydrogen

traps in Ni-17Cr-8Fe alloys," *Scripta Materialia*, vol. 36, no. 6, pp. 713–719, 1997.

[104] T. Nambu *et al.*, "Enhanced hydrogen embrittlement of Pd-coated niobium metal membrane detected by in situ small punch test under hydrogen permeation," *Journal of Alloys and Compounds*, vol. 446–447, pp. 588–592, Oct. 2007.

[105] G. Zhang *et al.*, "Analysis of hydrogen diffusion coefficient during hydrogen permeation through pure niobium," *International Journal of Hydrogen Energy*, vol. 33, no. 16, pp. 4419–4423, Aug. 2008.

[106] E. E. Underwood and J. E.A. Starke, "Quantitative stereological methods for analyzing important microstructural features in fatigue of metals and alloys."

[107] L. Rongbin, Y. Mei, L. Wenchang, and H. Xianchang, "Effects of Cold Rolling on Precipitates in Inconel 718 Alloy," *Journal of materials engineering and performance*, vol. 11, no. October, pp. 504–508, 2002.

[108] S. Azadian, L.-Y. Wei, and R. Warren, "Delta phase precipitation in Inconel 718," *Materials Characterization*, vol. 53, no. 1, pp. 7–16, Sep. 2004.

[109] R. Riley, "Bragg's law for X-ray crystal diffraction," *Physics Education*, vol. 5, no. 6, pp. 371–372, 1970.

[110] W. C. Liu, F. R. Xiao, M. Yao, Z. L. Chen, Z. Q. Jiang, and S. G. Wang, "The influence of cold rolling on the precipitation of delta phase in inconel 718 alloy," *Scripta Materialia*, vol. 37, no. 1, pp. 53–57, 1997.

[111] R. . Li, M. Yao, W. . Liu, and X. . He, "Isolation and determination for δ γ′ and γ″ phases in Inconel 718 alloy," *Scripta Materialia*, vol. 46, no. 9, pp. 635–638, May 2002.

[112] ASTM, "Standard Test Method for Electrochemical Critical Pitting Temperature Testing of," *ASTM G 150*, vol. 99, no. Reapproved, pp. 1–13, 2004.

[113] ASTM, "Standard guide for laboratory immersion corrosion testing of metals TM0169/G31-12a," *ASTM International*, vol. G31–12a, pp. 1–10, 2012.

[114] E. L. Hibner, "A New Age-Hardenable Corrosion Resistant Alloy for Deep Sour Gas Well Service," *Superalloys 718, 625 and Various Derivatives (1991)*, pp. 895–903, 1991.

[115] A. Groysman, *Corrosion for Everybody*. Springer Dordrecht Heidelberg London New York, 2010.

[116] ASTM G61-86 (Reapproved 2014), "Standard Test Method for Conducting Cyclic Potentiodynamic Polarization Measurements for Localised Corrosion Susceptibility of Iron-,Nickel-,or Cobalt-Based Alloys," vol. 86, no. Reapproved 2014, pp. 1–9, 2014.

[117] J. R. Groh and R. W. Duvelius, "Influence of Corrosion Pitting on Alloy 718 Fatigue Capability," *Superalloys 718, 625, 706 and Various Derivatives (2001)*, pp. 583–592, 2001.

[118] T. Chen, H. John, J. Xu, Q. Lu, J. Hawk, and X. Liu, “Influence of surface modifications on pitting corrosion behavior of nickel-base alloy 718. Part 2: Effect of aging treatment,” *Corrosion Science*, vol. 78, pp. 151–161, Jan. 2014.

[119] L. M. R. Aguilar, Z. R. P, and E. L. F, “Electrochemical Noise Analysis of Nickel Based Superalloys in Acid Solutions,” *International Journal of electrochemical science*, vol. 9, pp. 523–533, 2014.

[120] C. A. . b Loto, “Electrochemical noise measurement technique in corrosion research,” *International Journal of Electrochemical Science*, vol. 7, no. 10, pp. 9248–9270, 2012.

[121] H. S. Klapper, J. Goellner, A. Burkert, and A. Heyn, “Environmental factors affecting pitting corrosion of type 304 stainless steel investigated by electrochemical noise measurements under potentiostatic control,” *Corrosion Science*, vol. 75, pp. 239–247, Oct. 2013.

[122] W. Melitz, J. Shen, A. C. Kummel, and S. Lee, “Kelvin probe force microscopy and its application,” *Surface Science Reports*, vol. 66, no. 1, pp. 1–27, Jan. 2011.

[123] M. Rohwerder and F. Turcu, “High-resolution Kelvin probe microscopy in corrosion science: Scanning Kelvin probe force microscopy (SKPFM) versus classical scanning Kelvin probe (SKP),” *Electrochimica Acta*, vol. 53, no. 2, pp. 290–299, 2007.

[124] P. Schmutz, “Corrosion Study of AA2024-T3 by Scanning Kelvin Probe Force Microscopy and In Situ Atomic Force Microscopy Scratching,” *Journal of The Electrochemical Society*, vol. 145, no. 7, p. 2295, 1998.

[125] B. Kagay, S. Coryell, K. Findley, and A. Nissan, “Slow Strain Rate and Rising Step Load Hydrogen Embrittlement Testing of UNS N07718,” in *NACE Corrosion*, 2016, no. 7861, pp. 1–15.

[126] I. K. Pokhodnya and V. I. Shvachko, “NATURE OF HYDROGEN BRITTLENESS OF STRUCTURAL STEELS,” vol. 37, no. 2, pp. 87–96, 2001.

[127] C. M. Younes, a. M. Steele, J. a. Nicholson, and C. J. Barnett, “Influence of hydrogen content on the tensile properties and fracture of austenitic stainless steel welds,” *International Journal of Hydrogen Energy*, vol. 38, no. 11, pp. 4864–4876, 2013.

[128] K. A. Esaklul and T. M. Ahmed, “Prevention of failures of high strength fasteners in use in offshore and subsea applications,” *Engineering Failure Analysis*, vol. 16, no. 4, pp. 1195–1202, 2009.

[129] S. L. Robinson, B. P. Somerday, and N. R. Moody, “HYDROGEN EMBRITTLEMENT OF STAINLESS STEELS,” *Methods*.

[130] M. Cornet, C. Bertrand, and M. D. A. C. Belo, “Hydrogen Embrittlement of Ultra-Pure Alloys of the Inconel 600 Type : Influence of the Additions of Elements (C , P , Sn , Sb) f •,” *Metallurgical Transactions A*, vol. 13, no. January, pp. 141–144, 1982.

[131] I. Capelle, J. Dmzatrakh, “HYDROGEN EFFECT ON LOCAL FRACTURE EMANATING FROM NOTCHES IN PIPELINE FROM STEEL API X52 J. Capelle,” *Strength of Materials*, vol. 41, no. 5, pp. 493–500, 2009.

[132] T. Keller, “Verhalten von Wasserstoff in Titanlegierungen : Absorption , Diffusion und Phasenumwandlungen,” TU Darmstadt, 2005.

[133] S. I. Mikitishin, V. V. Fedorov, O. M. Sergientko, O. R. Sokolovskii, and Y. M. Spas, “Determination of the diffusion coefficient of hydrogen in Metals from the rate of change in the electrical resistance in desorption,” no. 1, pp. 22–25, 1985.

[134] M. A. V Devanathan and Z. Stachurski, “The Adsorption and Diffusion of Electrolytic Hydrogen in Palladium,” *Proceedings of the Royal Society A: Mathematical, Physical and Engineering Sciences*, vol. 270, pp. 90–102, 1962.

[135] American Society for Testing Materials, “Standard Practice for Evaluation of Hydrogen Uptake , Permeation , and Transport in Metals by an Electrochemical Technique,” *G148-97*, vol. i, no. Reapproved, pp. 1–10, 2011.

[136] D. Norm, “DIN EN ISO 17081 - Elektrochemische Wasserstoffpermeation,” 2008.

[137] A. Turnbull, R. G. Ballinger, I. S. Hwang, M. M. Morra, M. Psaila-Dombrowski, and R. M. Gates, “Hydrogen transport in nickel-base alloys,” *Metallurgical Transactions A*, vol. 23, no. December, pp. 3231–3244, Dec. 1992.

[138] J. Svoboda, G. Mori, A. Prethaler, and F. D. Fischer, “Determination of trapping parameters and the chemical diffusion coefficient from hydrogen permeation experiments,” *Corrosion Science*, vol. 82, pp. 93–100, May 2014.

[139] P. Manolatos, C. Duret-Thual, J. Le Coze, M. Jerome, and E. Bollinger, “The electrochemical permeation of hydrogen in steels without palladium coating. Part II: Study of the influence of microstructure on hydrogen diffusion,” *Corrosion Science*, vol. 37, no. 11, pp. 1785–1796, 1995.

[140] P. Manolatos and M. Jerome, “A thin palladium coating on iron for hydrogen permeation studies,” *Electrochimica Acta*, vol. 41, no. 3, pp. 359–365, 1996.

[141] P. C. association of Petroleum, “Use of International Standard NACE MR0175/ISO15156,” 2008.

[142] E. L. Hibner and B. Puckert, “High-Strength Corrosion Resistant Nickel Base alloy 725HS for severe sour oil and gas field applications.”

[143] I. L. W. Wilson and M. G. Burke, “The Effect of Microstructure on the SCC Behavior of Alloy 718,” *Superalloys 718, 625 and Various Derivatives (1991)*, pp. 681–693, 1991.

[144] E. L. Hibner, “Innovative nickel alloys for service in critical marine applications.”

[145] M. T. Miglin and J. L. Nelson, “Strain Rate Sensitivity of Alloy 718 Stress Corrosion Cracking,” *Superalloys 718, 625 and Various Derivatives (1991)*, pp. 695–704, 1991.

[146] W. L. Kimmerle, M. T. Miglin, and J. L. Nelson, “STRESS CORROSION CRACKING OF ALLOY 718 IN PRIMARY WATER,” *The Minerals, Metals and Materials Society*, 1989.

[147] J. Xu, H. John, G. Wiese, X. Liu, and B. H. Incorporated, “OIL-GRADE ALLOY 718

IN OIL FIELD DRILLING APPLICATION," *TMS (The Minerals, Metals & Materials Society)*, pp. 923–932, 2010.

[148] T. Chen, J. Nutter, J. Hawk, and X. Liu, "Corrosion fatigue crack growth behavior of oil-grade nickel-base alloy 718. Part 1: Effect of corrosive environment," *Corrosion Science*, vol. 89, pp. 146–153, 2014.

[149] L. Tan, X. Ren, K. Sridharan, and T. R. Allen, "Corrosion behavior of Ni-base alloys for advanced high temperature water-cooled nuclear plants," *Corrosion Science*, vol. 50, no. 11, pp. 3056–3062, Nov. 2008.

[150] J. Yao, S. A. Meguid, and J. R. Cahoon, "Hydrogen Diffusion and Its Relevance to Intergranular Cracking in Nickel," *Metallurgical Transactions A*, vol. 24, no. January, pp. 105–112, 1993.

[151] H. Hagi, Y. Hayashi, and N. Ohtani, "Diffusion Coefficient of Hydrogen in Pure Iron between 230 and 300 K," *Transactions of the Japan Institute of Metals*, vol. 20, no. 7, pp. 349–357, 1979.

[152] I. M. B. G.M. Pressouyre, "A Quantitative Analysis of Hydrogen Trapping," *Metallurgical Transactions A*, vol. 9, no. November, pp. 1571–1580, 1978.

[153] J. P. Hirth, "Effects of Hydrogen on the Properties of Iron and Steel," *Metallurgical Transactions*, vol. 11, no. June, pp. 861–890, 1980.

[154] M. Choi *et al.*, "Tensile behavior of hydrogen-charged 316L stainless steel at elevated temperatures," *Materials Science and Engineering: A*, vol. 595, pp. 165–172, Feb. 2014.

[155] J. M. Zagal, H. F. López, O. Flores, J. L. Albarran, and L. Martínez, "Microstructural effects on the hydrogen permeation of an Inconel alloy 690," *Corrosion Science*, vol. 50, no. 12, pp. 3371–3377, 2008.

[156] A. M. Brass and A. Chanfreau, "ACCELERATED DIFFUSION OF HYDROGEN GRAIN BOUNDARIES IN NICKEL," *Acta Materialia*, vol. 44, no. 9, pp. 3823–3831, 1996.

[157] T. M. Harris, "Hydrogen diffusion and trapping in electrodeposited nickel," Massachusetts Institute of Technology, 1989.

[158] A. Oudriss *et al.*, "Grain size and grain-boundary effects on diffusion and trapping of hydrogen in pure nickel," *Acta Materialia*, vol. 60, no. 19, pp. 6814–6828, Nov. 2012.

[159] T. M. Harris and R. M. Latanision, "Grain Boundary Diffusion of Hydrogen in Nickel," *Metallurgical Transactions A*, vol. 22, no. February, pp. 351–355, 1991.

[160] C. Marte and R. Kirchheim, "Hydrogen diffusion in nanocrystalline nickel indicating a structural change within the grain boundaries after annealing," *Scripta Materialia*, vol. 37, no. 8, pp. 1171–1175, Oct. 1997.

[161] D. T. Peterson, A. B. Hull, and B. A. Loomis, "Hydrogen Embrittlement Considerations in Niobium-Base Alloys For Application in the Iter Divertor," 1992.

[162] W. M. Robertson, “Hydrogen Permeation and Diffusion in Inconel 718 and Incoloy 903,” *Metallurgical Transactions A*, vol. 8, no. November, pp. 1709–1712, 1977.

[163] D. Connétable, F. Galliano, G. Odemer, C. Blanc, and É. Andrieu, “DFT study of the solubility of hydrogen and carbon in Ni3Nb-D0a and Ni3Nb-D022 systems,” *Journal of Alloys and Compounds*, vol. 610, pp. 347–351, 2014.

[164] Z. Tarzimoghadam *et al.*, “Multi-scale and spatially resolved hydrogen mapping in a Ni-Nb model alloy reveals the role of the δphase in hydrogen embrittlement of alloy 718,” *Acta Materialia*, vol. 109, pp. 69–81, 2016.

[165] J. K. Zahra Tarzimoghadam, Dirk Ponge, Dierk Raabe, “Hydrogen-assisted Failure in Nickel base alloy UNS N07718,” in *NACE Corrosion*, 2016, no. 244, pp. 1–10.

[166] P. D. Hicks and C. J. Altstetter, “Hydrogen-Enhanced Cracking of Superalloys,” *metallurgical transactions A*, vol. 23, no. January, pp. 237–249, 1992.

[167] Z. Tarzimoghadam, D. Ponge, J. Klöwer, and D. Raabe, “Hydrogen-assisted failure in Ni-based superalloy 718 studied under in situ hydrogen charging: The role of localized deformation in crack propagation,” *Acta Materialia*, vol. 128, pp. 365–374, Apr. 2017.

[168] L. Liu, C. Lu, W. Ding, A. Hirose, and K. F. Kobayashi, “Effect of delta phase on hydrogen embrittlement of inconel 718 by notch tensile tests,” *J. Mater. Sci. Technol.*, vol. 21, no. 2, pp. 256–260, 2005.

[169] G. Sjoberg and D. Gornu, “Hydrogen embrittlement of Cast Alloy 718. Effects of Homogenization, grain size and δphase,” *Superalloys 718, 625, 706 and Various Derivatives, E.A. Loria ed., TMS*, pp. 679–689, 2001.

[170] A. Hirose, Y. Arita, Y. Nakanishi, and K. F. Kobayashi, “Decrease in hydrogen embrittlement sensitivity of INCONEL 718 by laser surface softening,” *Materials Science and Engineering: A*, vol. 219, no. 1, pp. 71–79, 1996.

[171] K. A. Yushchenko, V. S. Savchenko, and O. N. Ostapenko, “Effect of heat treatment on the resistance of a dispersion hardening nickel alloy to hydrogen embrittlement,” pp. 17–20, 1992.

[172] B. D. Craig, “Evaluation and Application of Highly Alloyed Materials for Corrosive Oil Production,” *Journal materials for Energy Systems*, vol. 5, no. 1, pp. 53–58, 1983.

[173] S. Huizinga, W. E. Like, B. McLoughlin, and J. De Jong, “Offshore Nickel Alloy Tubing Hanger and Duplex Stainless Steel Piping Failure Investigations,” 2003.

[174] B. Kagay, K. Findley, S. Coryell, and A. B. Nissan, “Effects of alloy 718 microstructure on hydrogen embrittlement susceptibility for oil and gas environments,” *Materials Science and Technology*, vol. 32, no. 7, pp. 697–707, May 2016.

[175] O. Golenishcheva, M. Oechsner, A. Aghajani, G. Andersohn, and J. Kloewer, *Influence of delta-phase precipitation on the pitting performance of UNS (N07718)*. 2014.

[176] M. a. V. Devanathan, Z. Stachurski, and W. Beck, “A Technique for the Evaluation of Hydrogen Embrittlement Characteristics of Electroplating Baths,” *Journal of The Electrochemical Society*, vol. 110, no. 8, pp. 886–890, 1963.

[177] O. Gosheva, M. Oechsner, G. Andersohn, J. Klöwer, and A. Aghajani, “Impact of microstructure on hydrogen solubility and diffusivity in UNS 07718,” in *NACE Corrosion*, 2016.

[178] S. Frappart *et al.*, “Hydrogen trapping in martensitic steel investigated using electrochemical permeation and thermal desorption spectroscopy,” *Scripta Materialia*, vol. 65, no. 10, pp. 859–862, Nov. 2011.

[179] D. M. Symons and A. W. Thompson, “The Effect of Hydrogen on the Fracture of Alloy X-750,” *Metallurgical and Materials Transactions A*, vol. 27, no. January, pp. 101–110, 1996.

[180] M. Koyama, D. Yamasaki, T. Nagashima, C. C. Tasan, and K. Tsuzaki, “In situ observations of silver-decoration evolution under hydrogen permeation: Effects of grain boundary misorientation on hydrogen flux in pure iron,” *Scripta Materialia*, vol. 129, pp. 48–51, 2017.

[181] ASTM International, *TM 0177 Laboratory Testing of Metals for Resistance to Sulfide Stress Cracking and Stress Corrosion Cracking in H2S Environments*. 2016.

[182] J. Klöwer, H. Sarmiento Klapper, O. Gosheva, and Z. Tarzimoghadam, “Effect of microstructural particularities on the corrosion resistance of nickel alloy UNS N07718 - What really makes the difference?,” *Corrosion 2017, Paper no. 9068 (New Orleans, Louisiana)*, 2017.

[183] T. Lehmann, *Bildverarbeitung für die Medizin : grundlagen, modelle, methoden, anwendungen*. Springer, 1997.

[184] ISO, *ISO 6507-1:2005: Metallic materials -- Vickers hardness test -- Part 1: Test method*. 2005.

[185] Beuth, “DIN EN ISO 6892-1:2009-12 - Zugversuch - Teil 1: Prüfverfahren bei Raumtemperatur / Tensile testing - Part 1: Method of test at room temperature,” *Beuth*. 2009.

[186] D. Norm, “DIN EN ISO 18265: Metallische Werkstoffe - Umwertung von Härtewerten,” *Normenausschuss Materialprüfung NMP im DIN*, p. 90, 2014.

[187] J. Xu, X. K. Sun, W. X. Chen, and Y. Y. Li, “Hydrogen permeation and diffusion in iron-base superalloys,” *Acta Metallurgica et Materialia*, vol. 41, no. 5, pp. 1455–1459, May 1993.

[188] R. A. Oriani, “The physical and Metallurgical Aspects of Hydrogen in Metals,” in *Fourth International Conference on Cold Fusion 1993*, 1993.

[189] C. N. Park, J.-Y. Lee, and G. W. Hong, “The effects of defect character on hydrogen diffusion in metals,” *Journal of Materials Science Letters*, vol. 2, no. 9, pp. 475–479, Sep. 1983.

[190] S. Chen, M. Zhao, and L. Rong, “Effect of grain size on the hydrogen embrittlement sensitivity of a precipitation strengthened Fe-Ni based alloy,” *Materials Science and Engineering A*, vol. 594, pp. 98–102, 2014.

[191] C. P. Blankenship Jr., E. Hornbogen, and E. A. S. Jr., “Predicting slip behavior in alloys containing shearable and strong particles,” *Materials Science and Engineering: A*, vol. 169, no. 1–2, pp. 33–41, Sep. 1993.

[192] P. Marcus, J. Oudar, and I. Olejord, “Studies of the influence of sulphur on the passivation of nickel by Auger electron spectroscopy and electron spectroscopy for chemical analysis,” *Materials Science and Engineering*, vol. 42, pp. 191–197, Jan. 1980.

[193] D. W. Worthem, I. M. Robertson, F. a. Leckie, D. F. Socie, and C. J. Altstetter, “Inhomogeneous deformation in INCONEL 718 during monotonic and cyclic loadings,” *Metallurgical Transactions A*, vol. 21, no. 12, pp. 3215–3220, Dec. 1990.

[194] A. Barnoush, “Hydrogen embrittlement,revisited by in situ electrochemical nanoindentation,” 2007.

[195] H. S. Ho, M. Risbet, and X. Feaugas, “On the unified view of the contribution of plastic strain to cyclic crack initiation: Impact of the progressive transformation of shear bands to persistent slip bands,” *Acta Materialia*, vol. 85, pp. 155–167, 2015.

[194] J. Klöwer, O. Gosheva, H. S. Klapper, Z. Tarzimoghadam, Effect of heat treatment and microstructural particularities on the corrosion resistance of nickel alloy 718, presented in SteelyHydrogen2018, 29-31 May, **2018**

Index of Figures

Index of tables

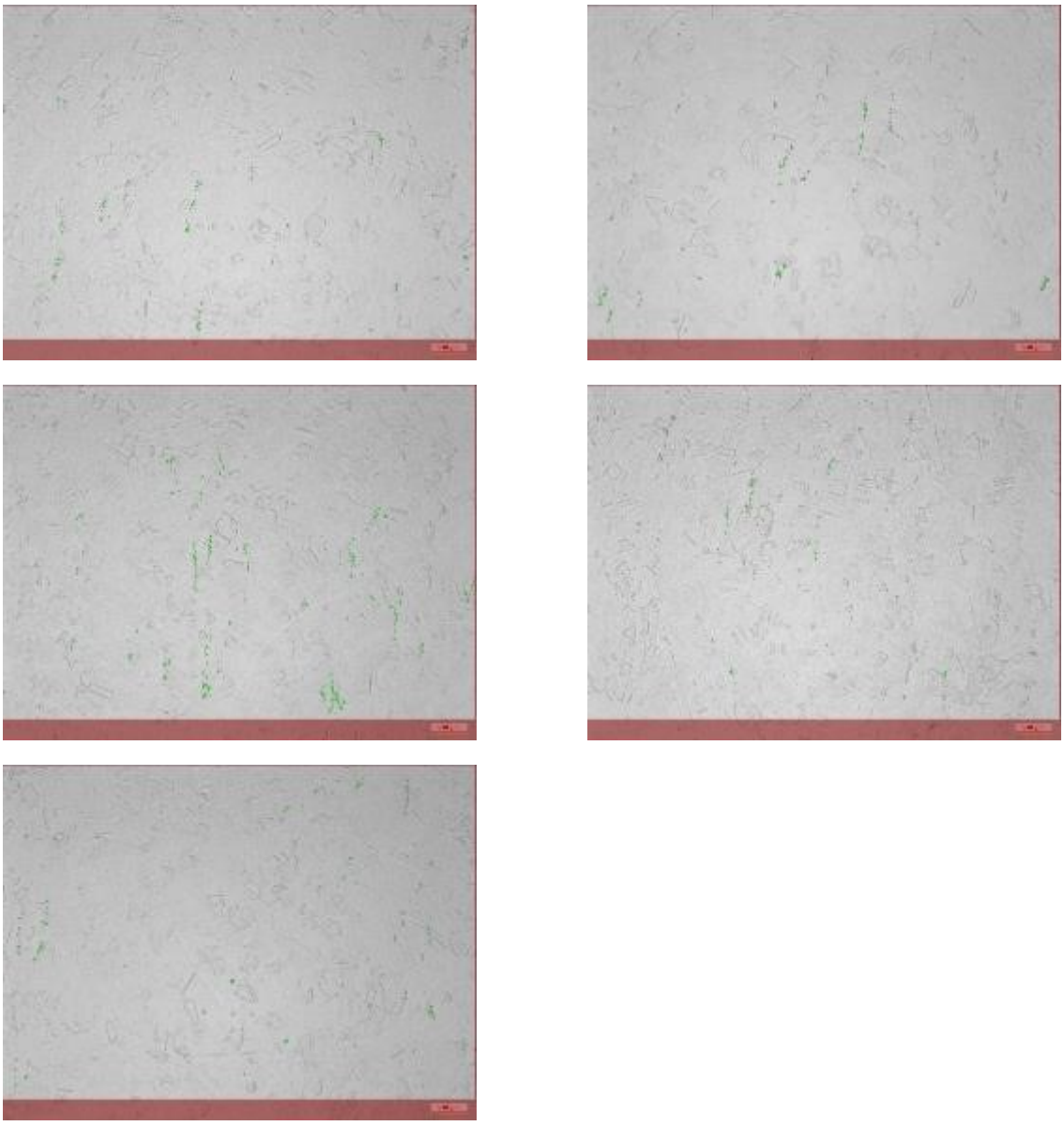

Figure 61: Light microscopy micrograph of the material variant 760. Carbonitrides Ti,Nb(C,N) are highlighted in green.

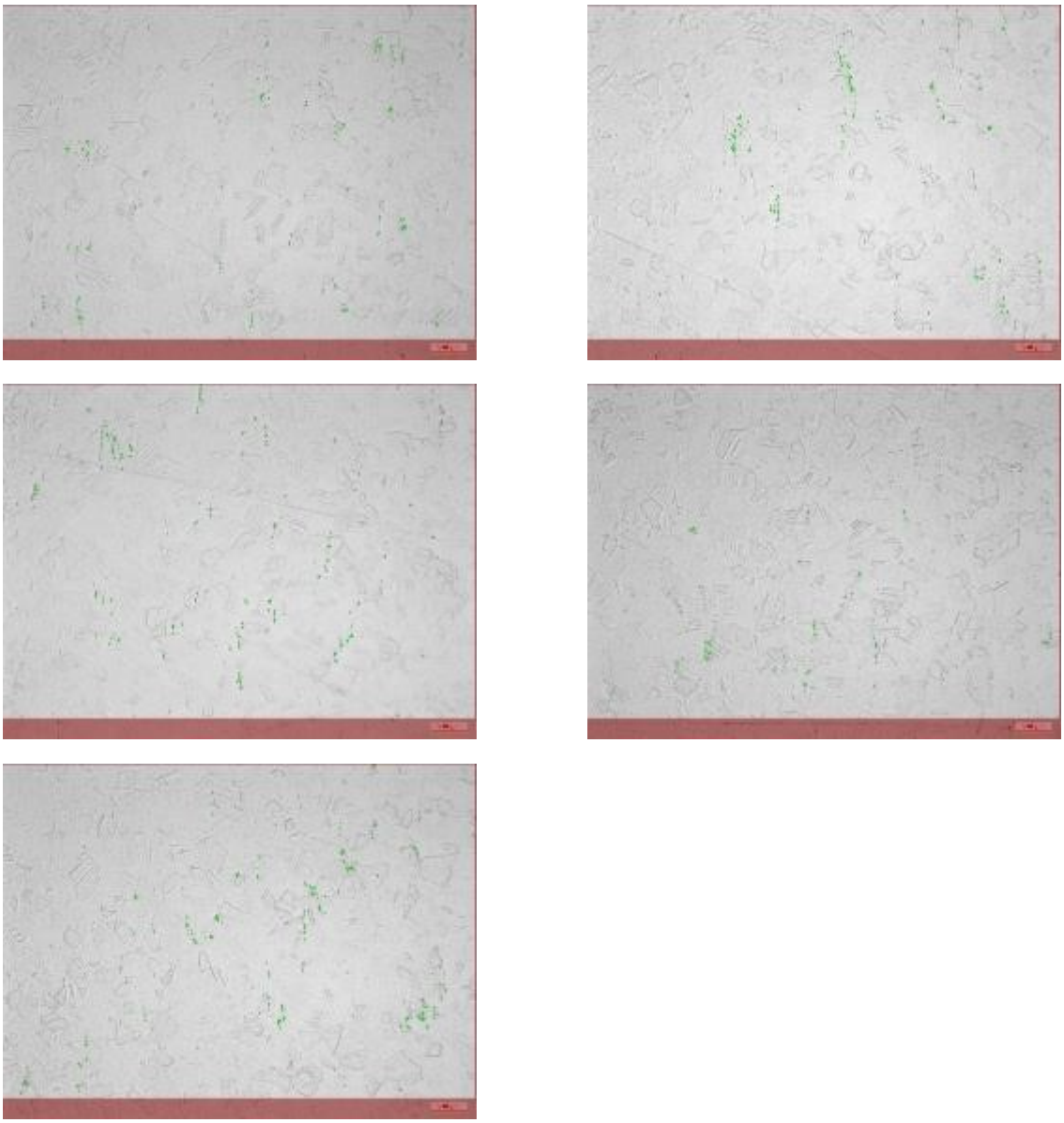

Figure 62: Light microscopy micrograph of the material variant 870. Carbonitrides Ti,Nb(C,N) are highlighted in green.

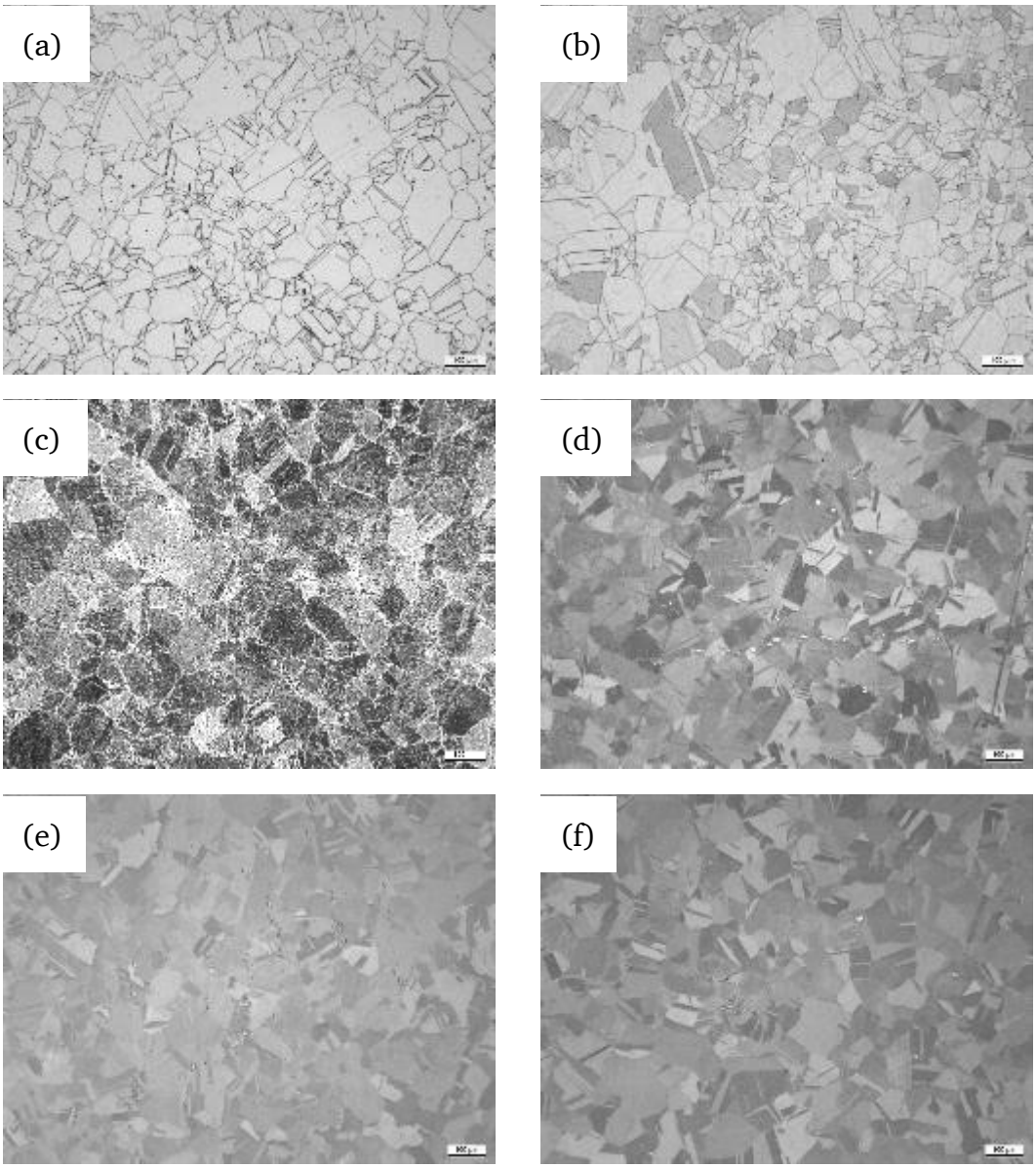

Figure 63: Optical microscopic micrographs of the aged alloy 718 – aging temperature has no influence on the grain size of the material: a) 1032; b) 760; c) 870; d) 800; e) 750; f) 720+620

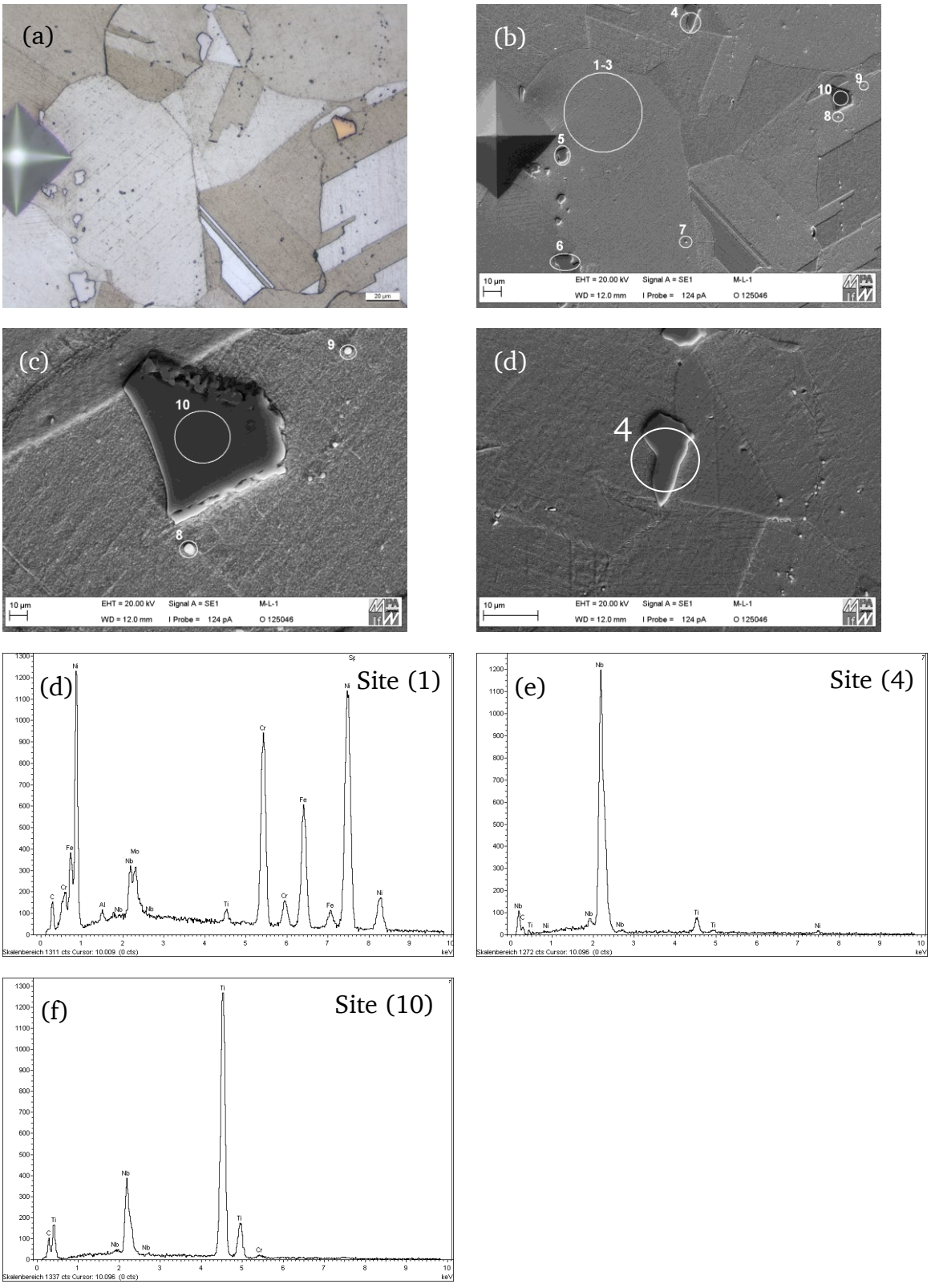

Figure 64: EDX-analysis of the microstructure peculiarities of aged alloy 718: exemplary measurements performed on the material variant 760

Table 11: Summary of the EDX-analysis measurements corresponding to the results presented in Figure 64

Site Nr.	C	Al	Ti	Cr	Fe	Ni	Nb	Mo	Sum
1	10.676	0.549	0.885	17.122	15.217	47.477	5.199	2.953	100.000
2	5.312	0.482	0.889	17.884	15.617	50.846	5.808	3.162	100.000
3	4.239	0.596	0.928	17.904	16.271	51.356	5.509	2.762	100.000
4	20.410	0.000	4.453	0.000	0.000	1.488	73.649	0.000	100.000
5	16.862	0.000	4.370	4.112	3.530	10.987	60.140	0.000	100.000
6	26.269	0.000	4.695	0.000	0.000	1.248	67.788	0.000	100.000
7	15.745	0.000	3.127	10.395	8.426	24.823	37.484	0.000	100.000
8	15.756	0.000	5.396	8.413	7.039	21.271	41.867	0.000	100.000
9	18.396	0.000	3.846	8.924	7.604	21.753	39.476	0.000	100.000
10	15.677	0.000	63.600	0.734	0.000	0.752	19.236	0.000	100.000

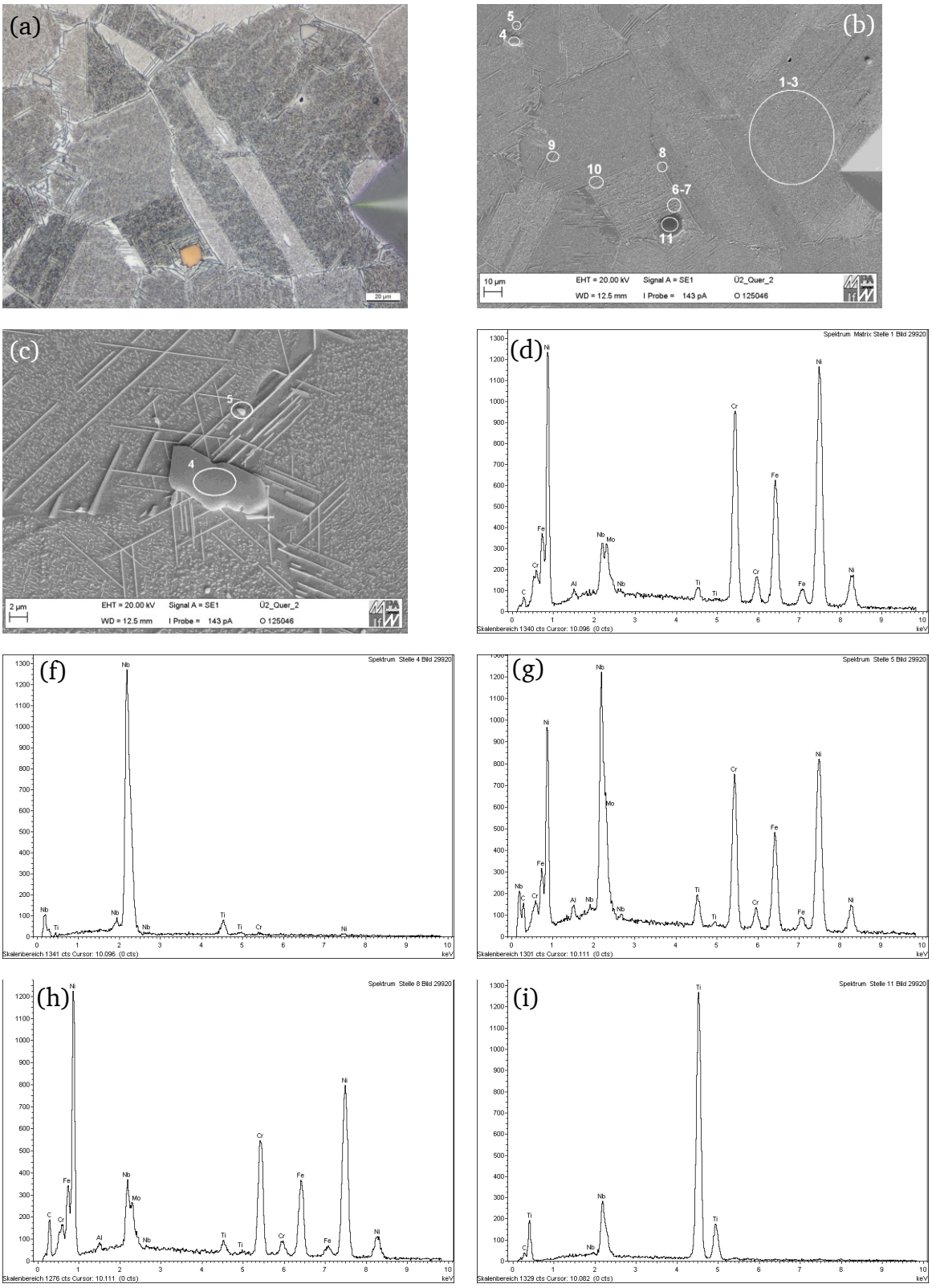

Figure 65: EDX-analysis of the microstructure peculiarities of aged alloy 718: exemplary measurements performed on the material variant 870

Table 12: Summary of the EDX-analysis measurements corresponding to the results presented in Figure 64

Site Nr.	C	Al	Ti	Cr	Fe	Ni	Nb	Mo	Sum
1	4.495	0.495	0.904	18.259	16.512	50.042	5.422	3.870	100.000
2	3.239	0.679	1.256	18.552	15.938	51.601	6.242	2.492	100.000
3	4.029	0.545	1.094	17.811	15.859	50.468	5.874	4.319	100.000
4	19.308	0.000	3.874	0.650	0.000	1.156	74.462	0.550	100.000
5	13.331	0.651	2.036	13.791	12.013	33.937	22.268	1.972	100.000
6	15.436	0.337	2.942	11.165	9.897	28.135	32.088	0.000	100.000
7	8.659	0.344	0.829	17.488	11.484	30.461	15.224	14.815	100.000
8	17.552	0.442	0.964	13.730	12.205	43.303	8.391	3.413	100.000
9	5.389	0.575	1.104	17.064	15.584	51.273	6.630	2.380	100.000
10	6.258	0.468	1.041	16.634	13.558	50.105	8.654	3.282	100.000
11	5.925	0.000	74.720	0.809	0.000	0.844	17.701	0.000	100.000

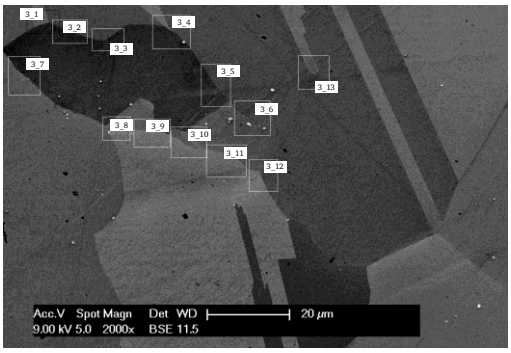

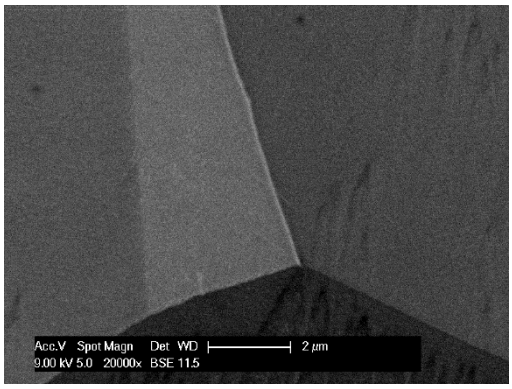

(3_1)

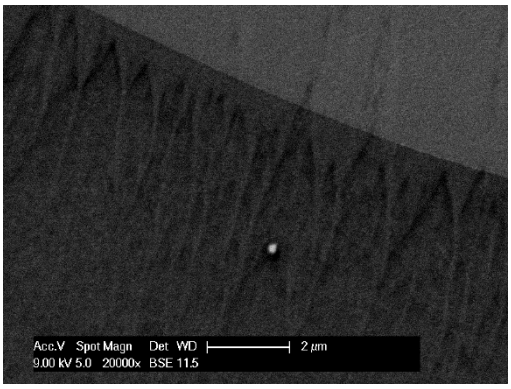

(3_2)

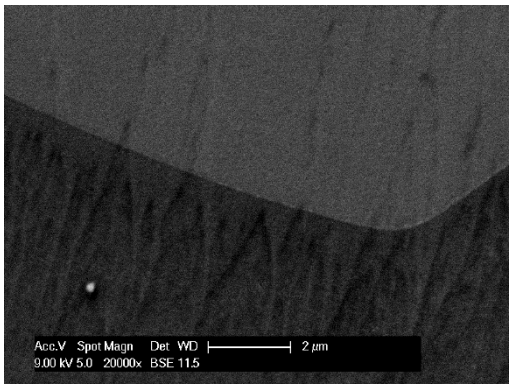

(3_3)

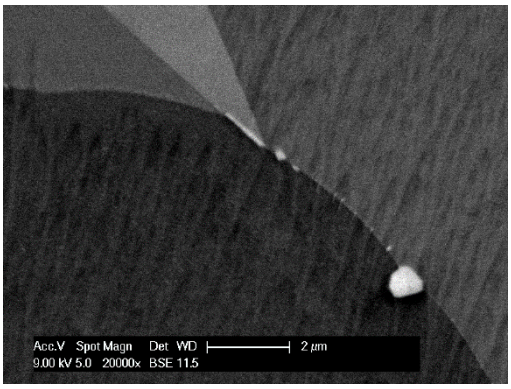

(3_4)

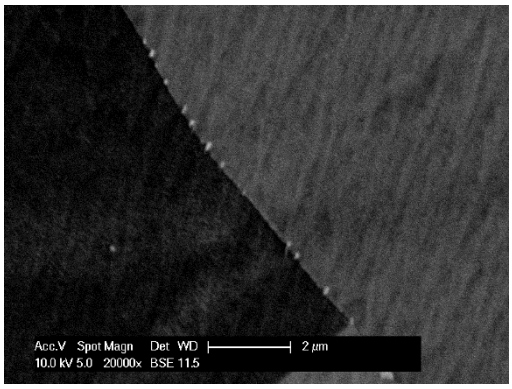

(3_5)

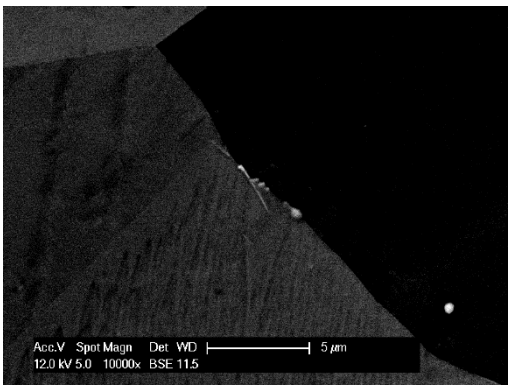

(3_7)

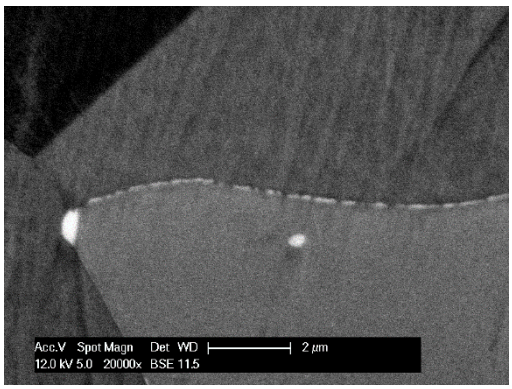

(3_8)

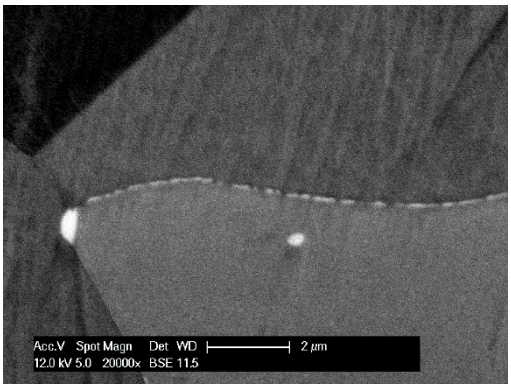

(3_9)

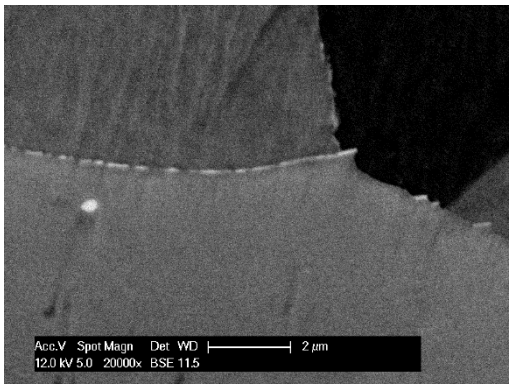

(3_10)

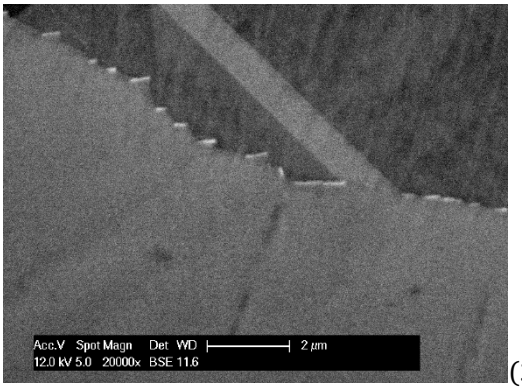

(3_11)

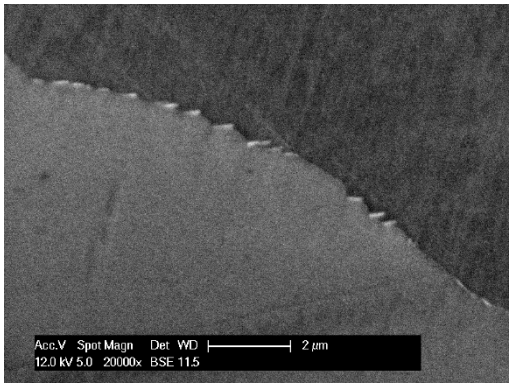

(3_12)

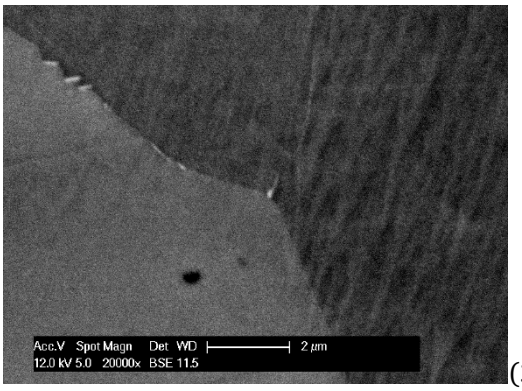

(3_13)

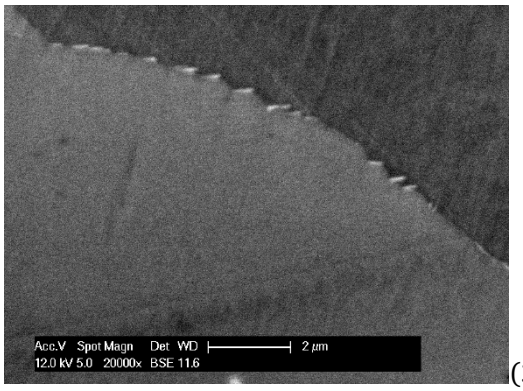

(3_14)

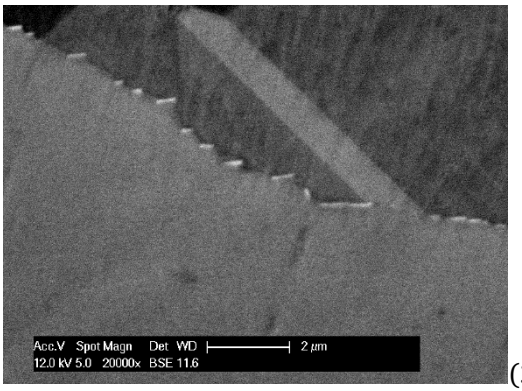

(3_15)

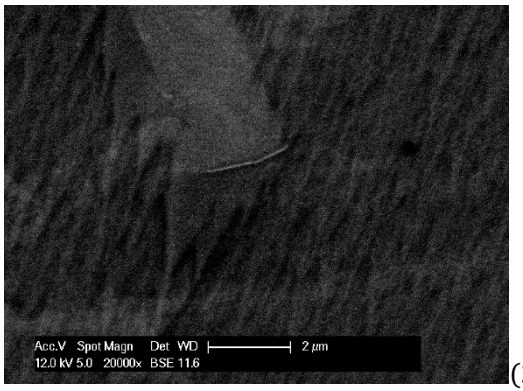

(3_16)

Figure 66: BSE micrographs of aged nickel base alloy 718 for the estimation of the δ phase content for the heat 800

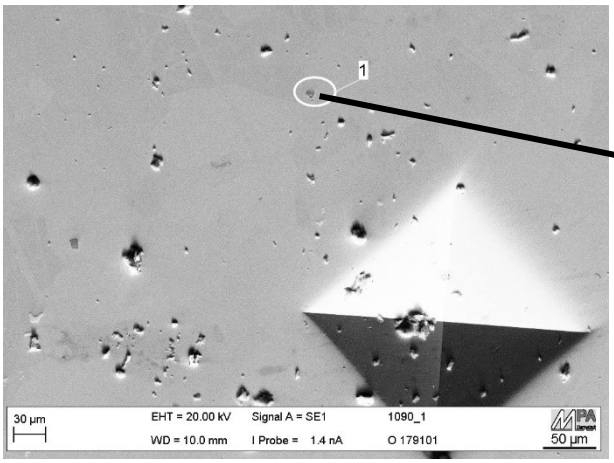
1
30 µm
EHT = 20.00 kV
WD = 10.0 mm
Signal A = SE1
I Probe = 1.4 nA
1090_1
O 179101
50 µm

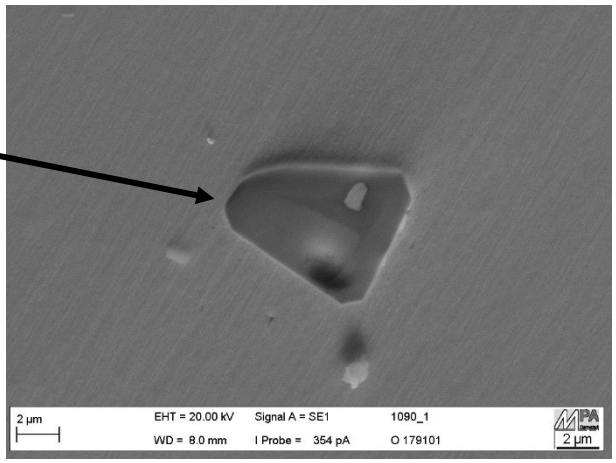
2 µm
EHT = 20.00 kV
WD = 8.0 mm
Signal A = SE1
I Probe = 354 pA
1090_1
O 179101
2 µm

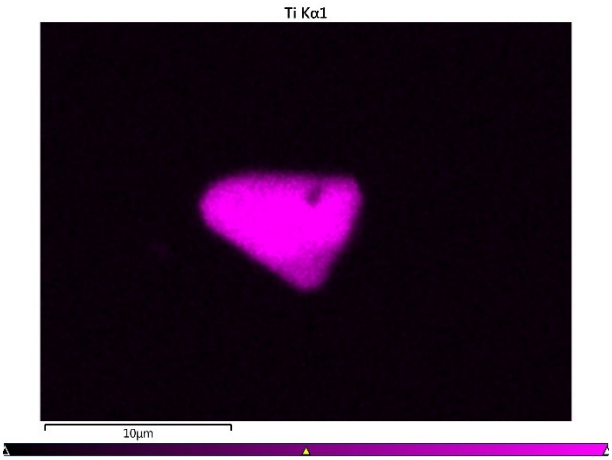
Ti Kα1
10µm

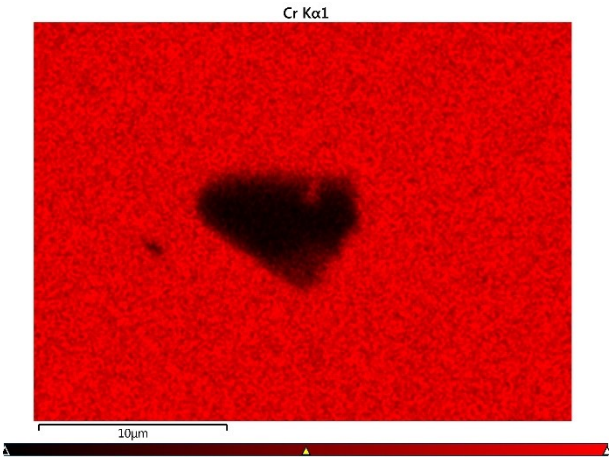
Cr Kα1
10µm

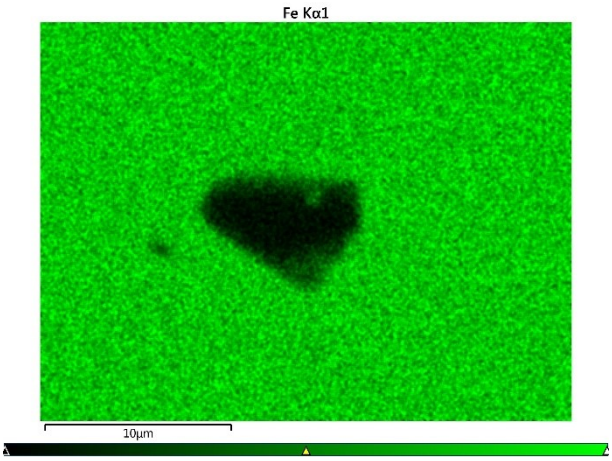
Fe Kα1
10µm

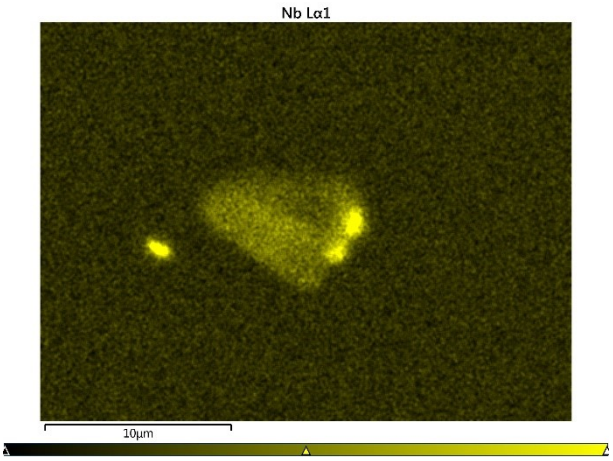
Nb Lα1
10µm

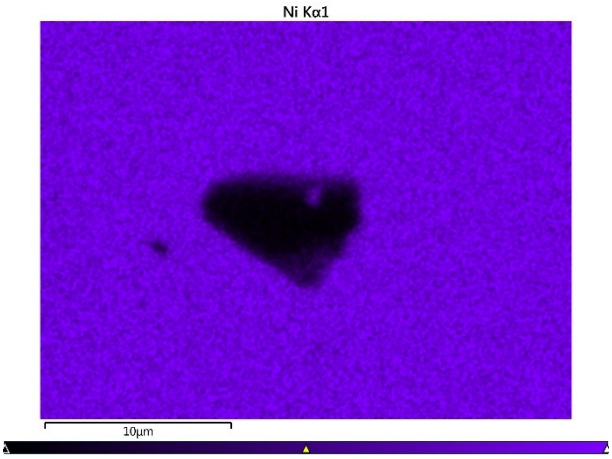

Figure 67: SEM and EDX documentation of the samples for the SKPFM-measurements

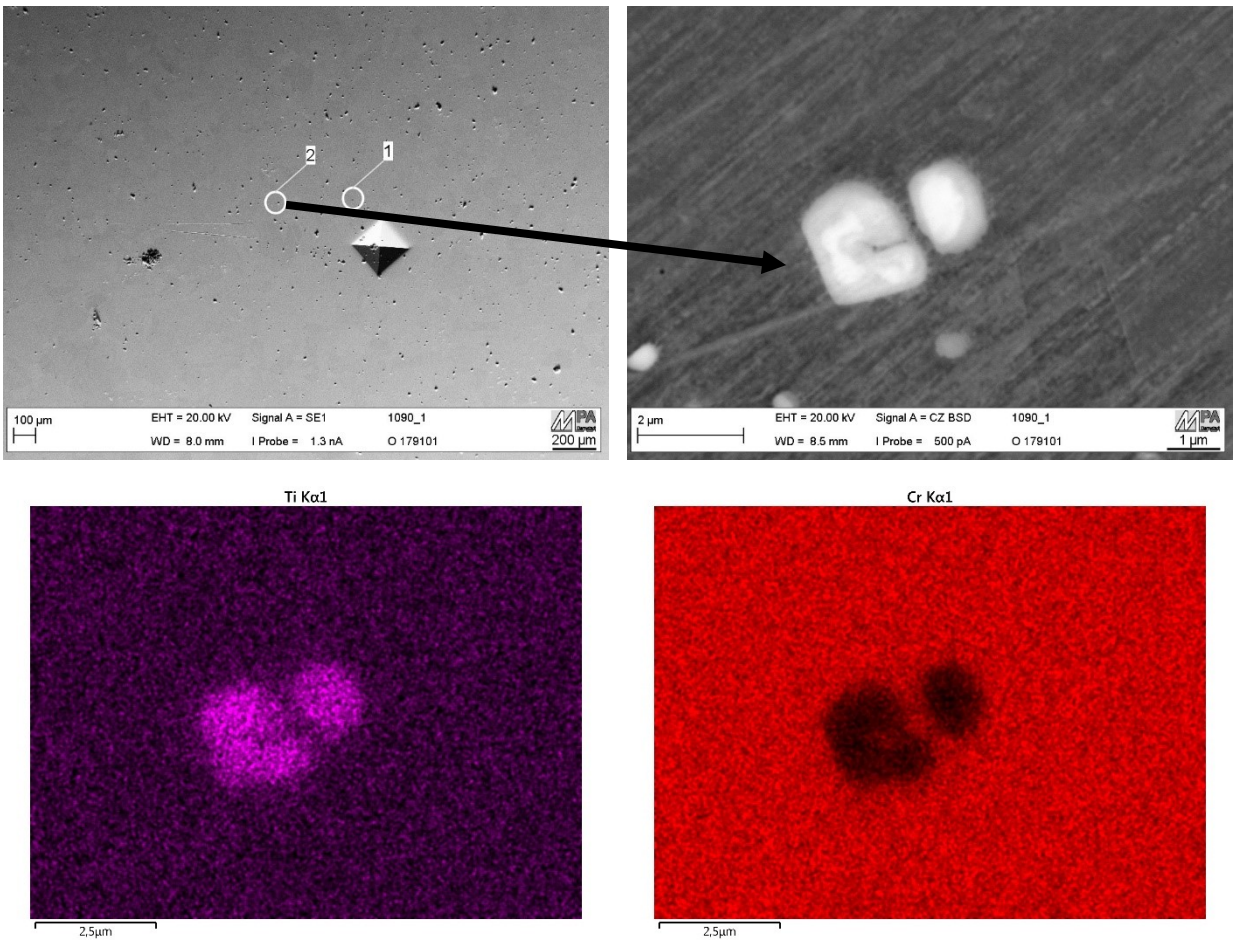

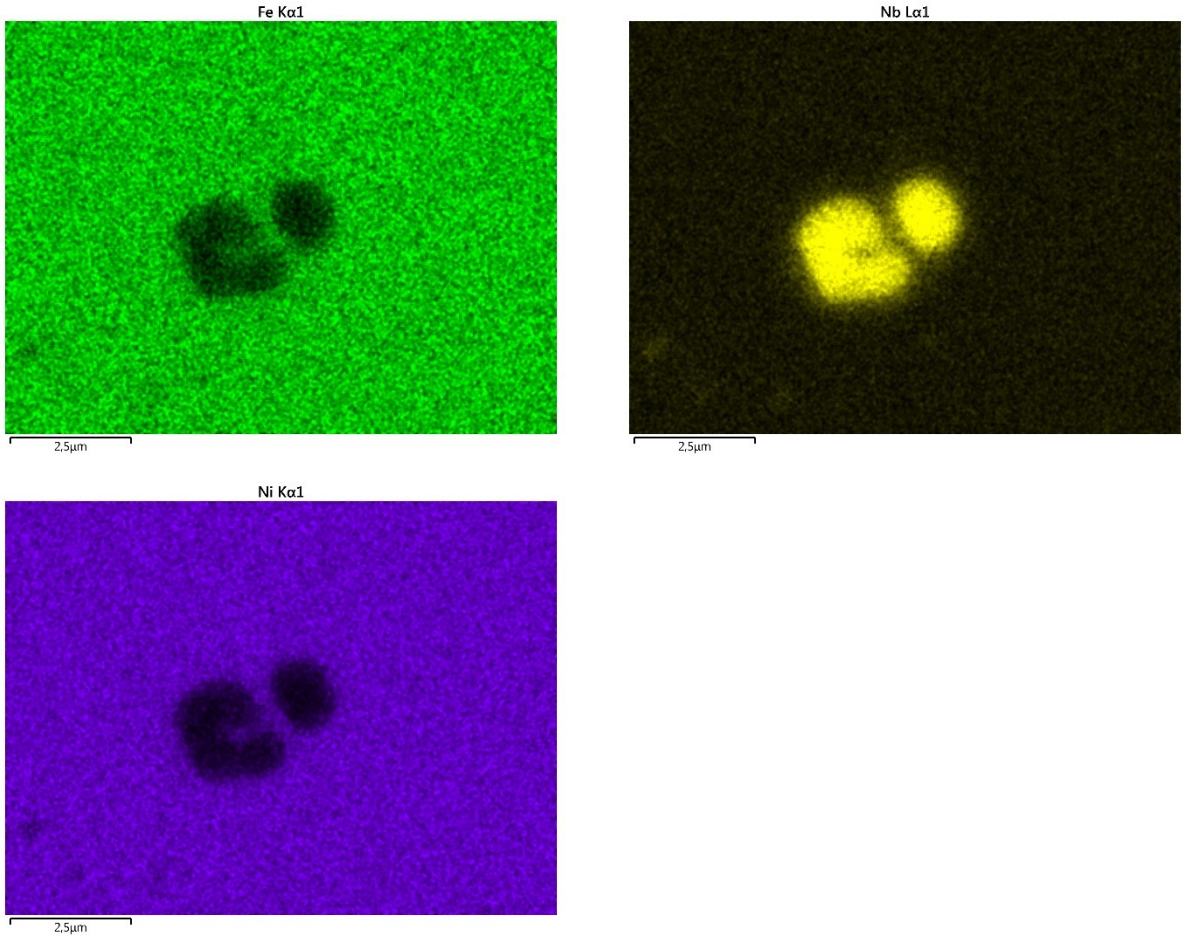

Figure 68: SEM and EDX documentation of the samples for the SKPFM-measurements

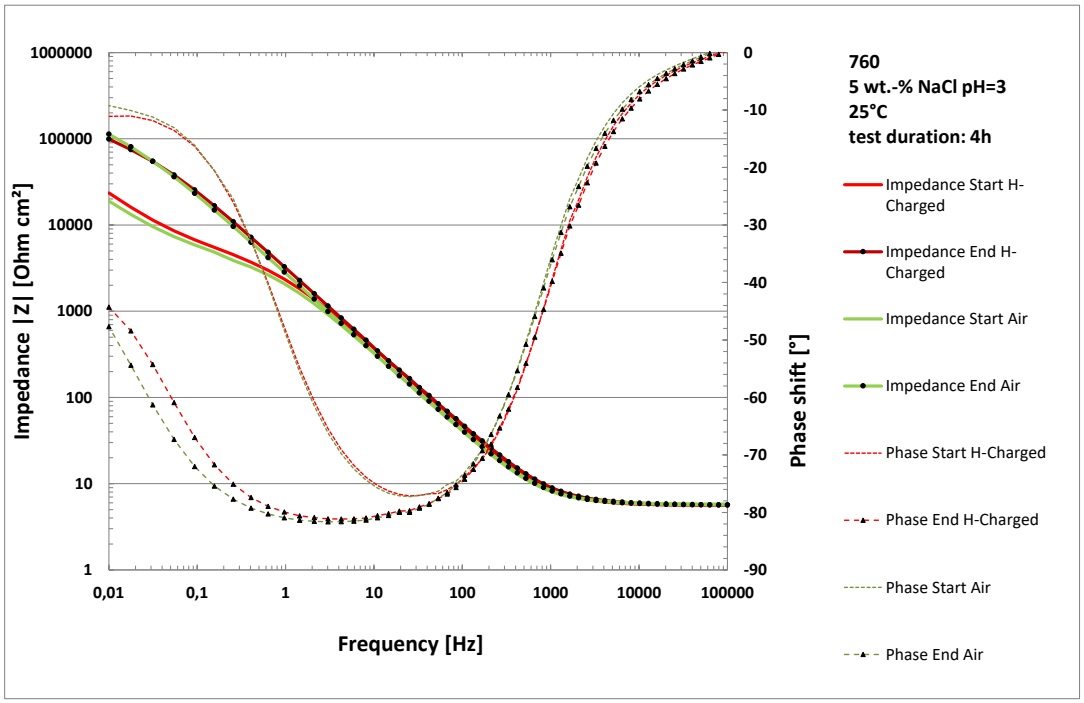

Figure 69: Comparison Bode plots of EIS measurements of material 760 in 5% NaCl pH 3

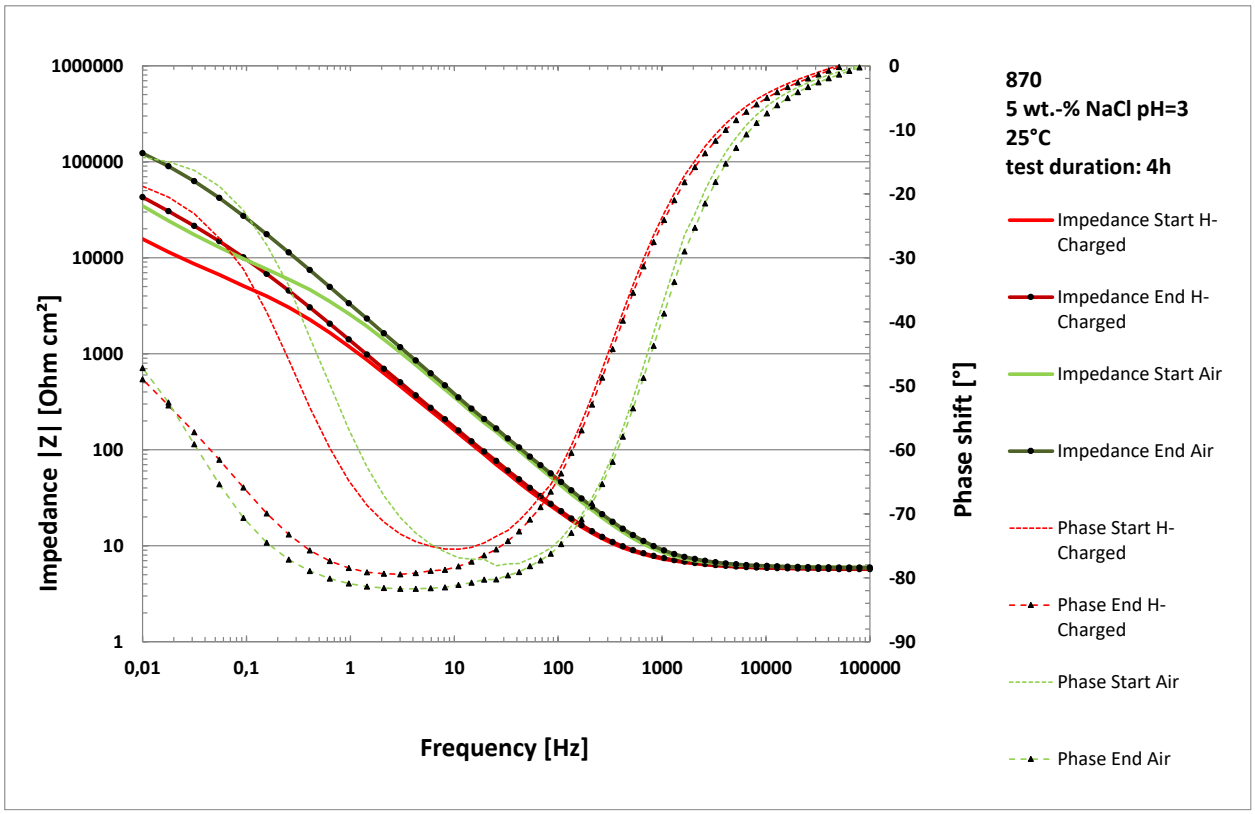

Figure 70: Comparison of Bode plots of EIS measurements of material 870 in 5% NaCl pH=3

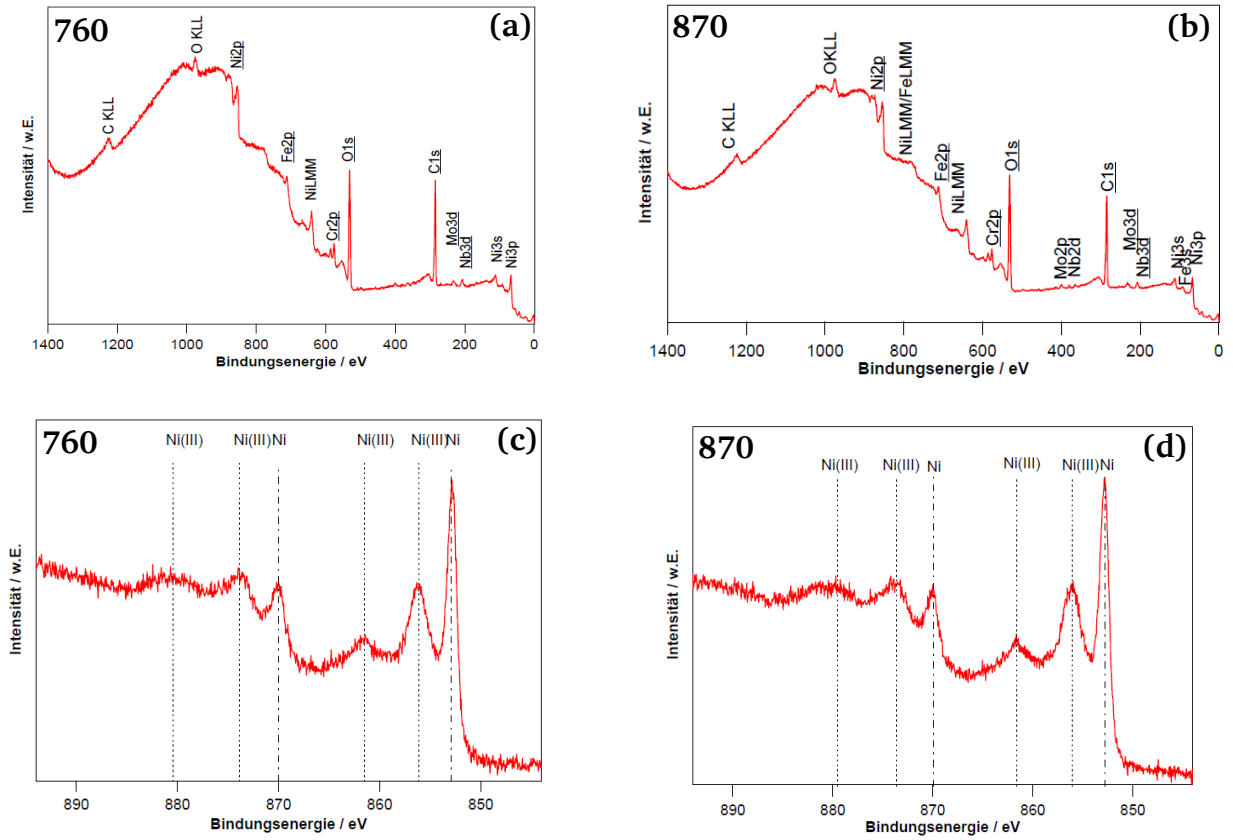

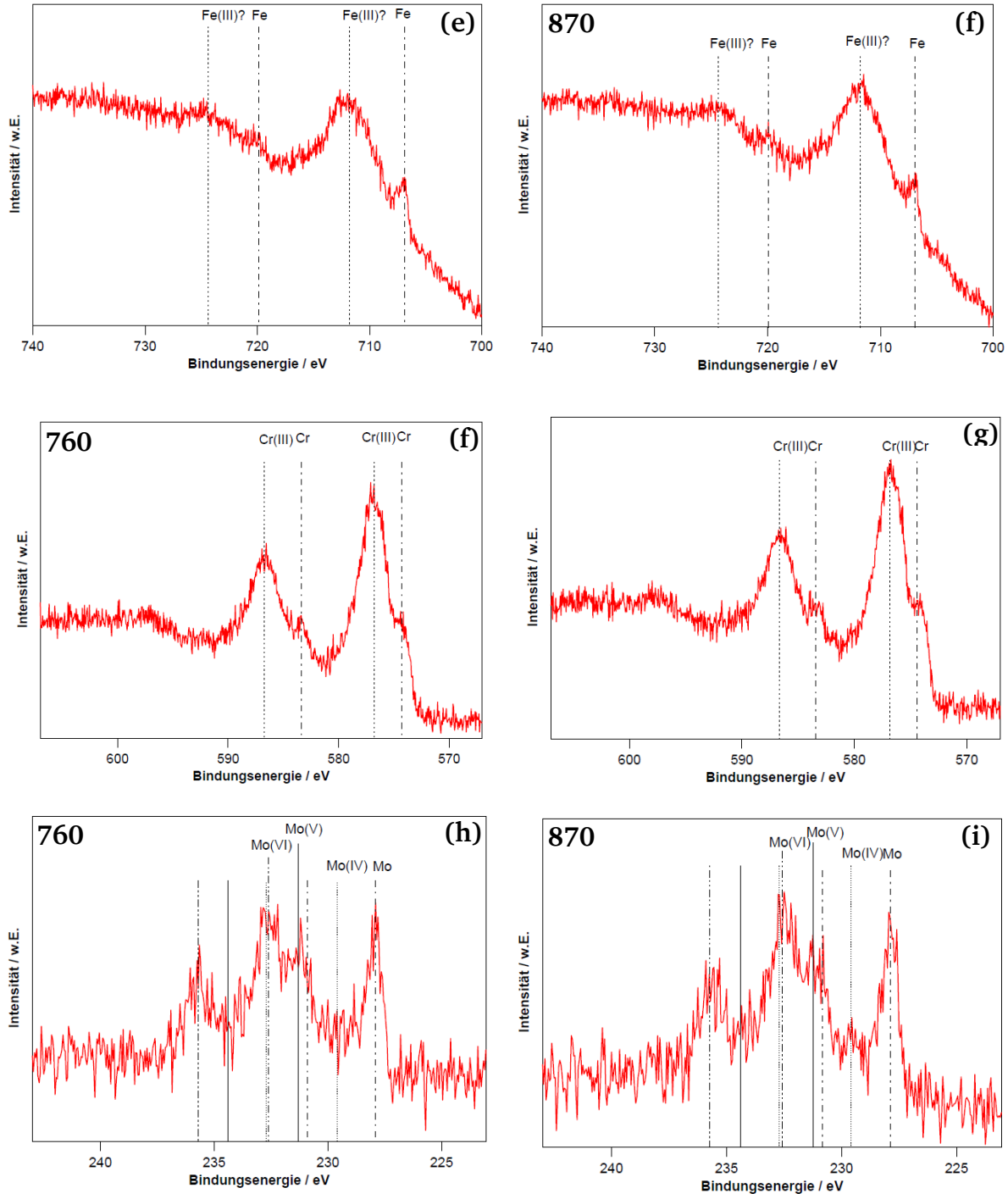
(e)
Fe(III)? Fe
Fe(III)? Fe
Intensität / w.E.
740
730
720
710
700
Bindungsenergie / eV
870
(f)
Fe(III)? Fe
Fe(III)? Fe
Intensität / w.E.
740
730
720
710
700
Bindungsenergie / eV
760
(f)
Cr(III) Cr
Cr(III)Cr
Intensität / w.E.
600
590
580
570
Bindungsenergie / eV
(g)
Cr(III)Cr
Cr(III)Cr
Intensität / w.E.
600
590
580
570
Bindungsenergie / eV
760
(h)
Mo(V)
Mo(VI)
Mo(IV) Mo
Intensität / w.E.
240
235
230
225
Bindungsenergie / eV
870
(i)
Mo(V)
Mo(VI)
Mo(IV)Mo
Intensität / w.E.
240
235
230
225
Bindungsenergie / eV

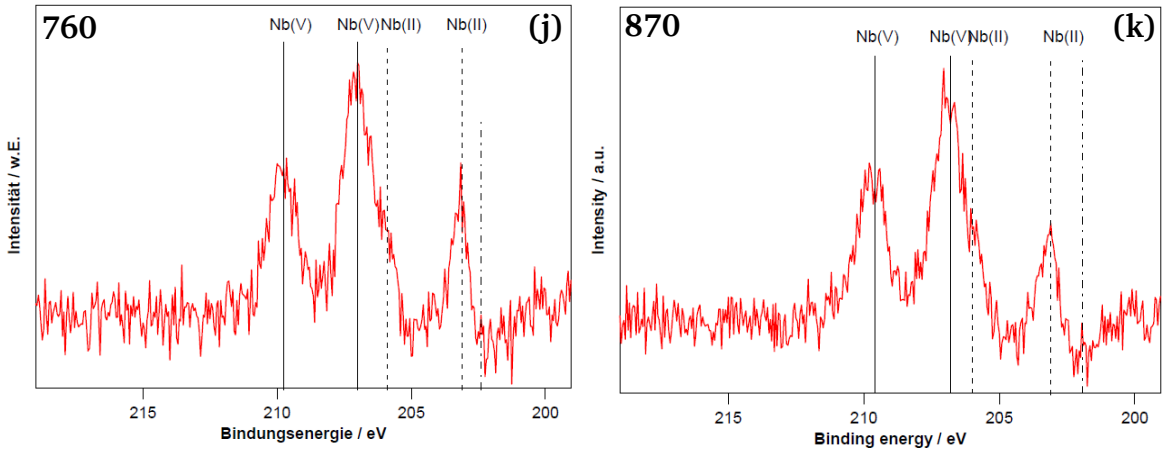

Figure 71: XPS-spectra of alloy 718

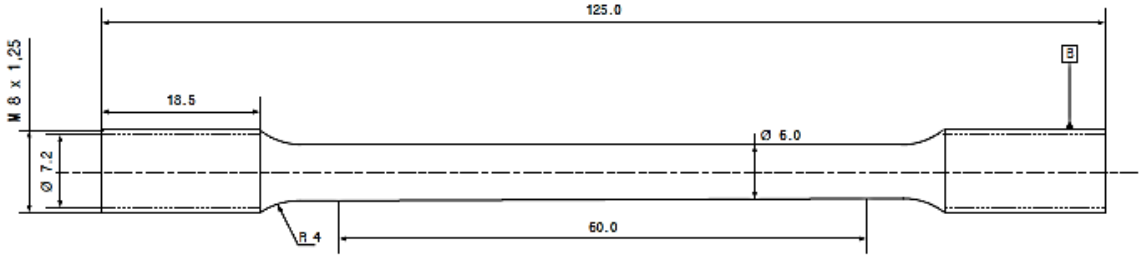

Figure 72: Sample geometry for the tensile tests

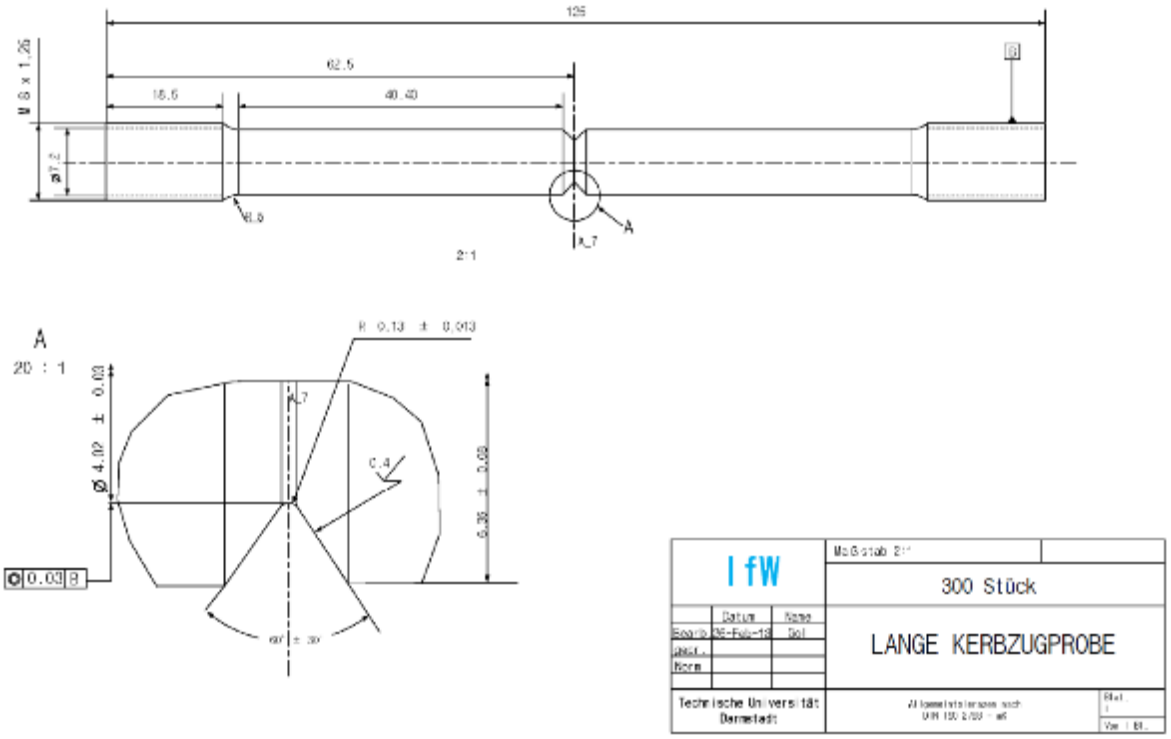

Figure 73: Notch tensile samples for hydrogen embrittlement tests

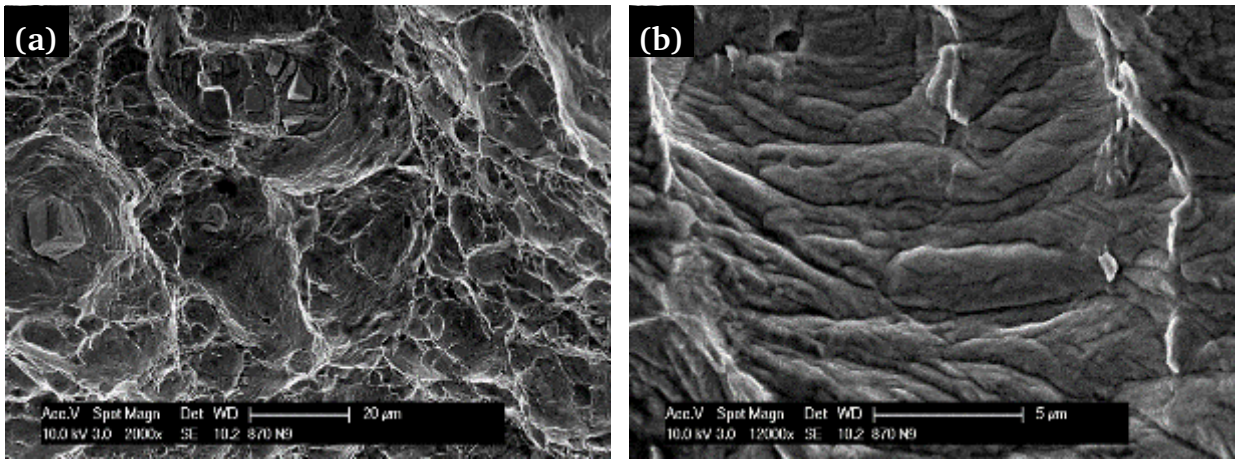

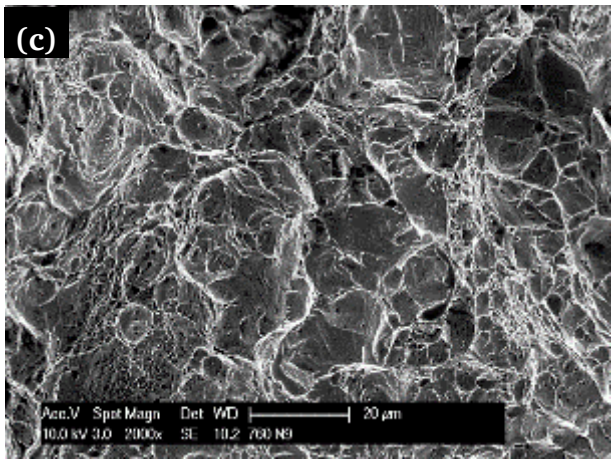
(c)
Acc.V Spot Magn Det WD 20 µm
10.0 kV 3.0 2000x SE 10.2 760 N9

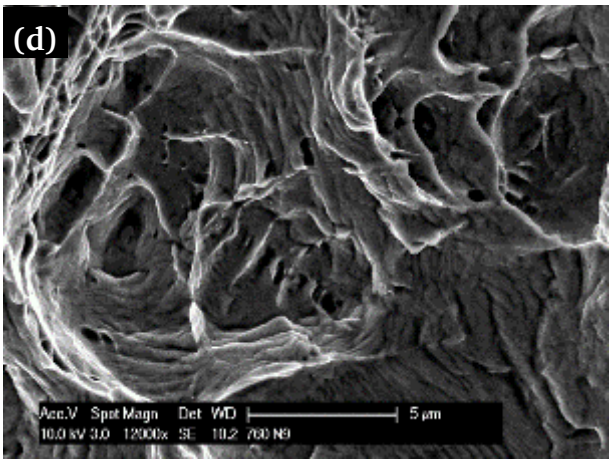
(d)
Acc.V Spot Magn Det WD 5 µm
10.0 kV 3.0 12000x SE 10.2 760 N9

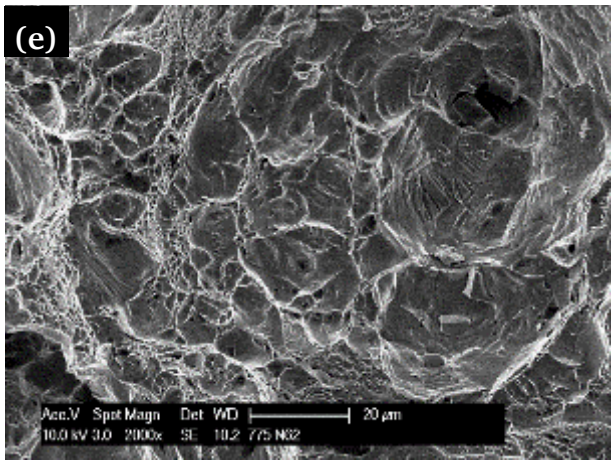
(e)
Acc.V Spot Magn Det WD 20 µm
10.0 kV 3.0 2000x SE 10.2 775 N32

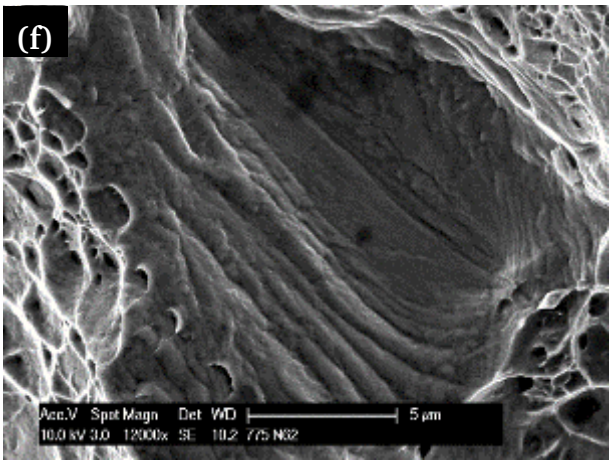
(f)
Acc.V Spot Magn Det WD 5 µm
10.0 kV 3.0 12000x SE 10.2 775 N32

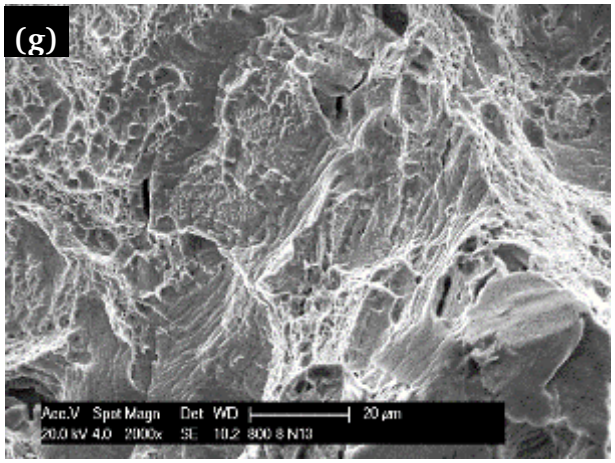
(g)
Acc.V Spot Magn Det WD 20 µm
20.0 kV 4.0 2000x SE 10.2 800 8 N13

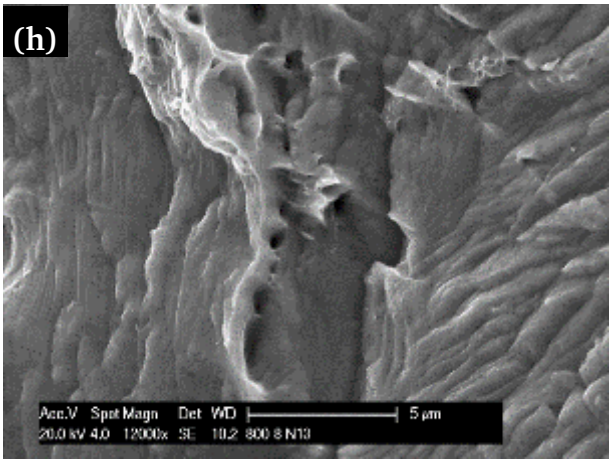
(h)
Acc.V Spot Magn Det WD 5 µm
20.0 kV 4.0 12000x SE 10.2 800 8 N13

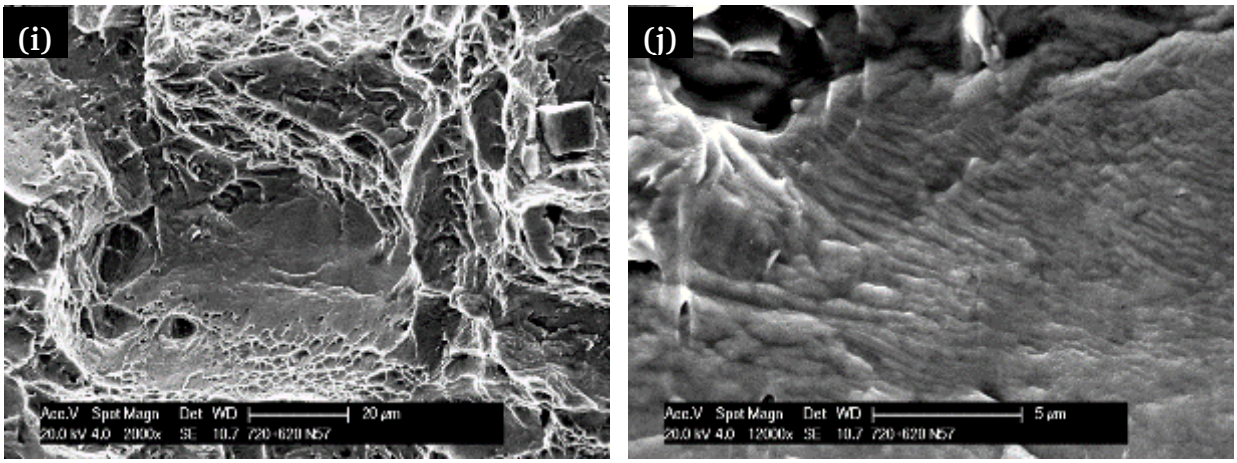

Figure 74: SEM micrographs of the alloy 718 samples after the tensile tests in air (0.02 mm/h): (a) and (b) – material 720+620; (c) and (d) – material 760; (e) and (f) – material 775; (g) and (h) – material 800; (i) and (j) – material 870

List of publications

Publication	Peer-Reviewed (y/n)
O. Golenishcheva, M. Oechsner, G. Andersohn, J. Kloewer, and A. Aghajani, Influence of Delta-phase Precipitation on the Pitting Performance of UNS (N07718), presented in *Corrosion 2014*, San Antonio, TX, 09-15 March, **2014**, paper No. 3895	yes
O. Golenishcheva, G. Andersohn, M. Oechsner, J. Klöwer, A. Aghajani, Hydrogen Diffusion Mechanism in Nickel Base Alloy 718, presented in Eurocorr **2014**	no
O.Golenishcheva, C. Krauß, G. Andersohn, M. Oechsner, Mechanisms of hydrogen-induced cracking in high-strength screws, *Material Science and Technology*, 46, **2015**, 190-196	yes
O. Gosheva, G. Andersohn, M. Oechsner, J. Klöwer, A. Aghajani, „Impact of microstructure on hydrogen solubility and diffusivity in UNS N07718“, presented in *Corrosion 2016*, Vancouver, Canada, 08-14 March, **2016**, paper No. 7267	yes
J. Klöwer, O. Gosheva, H. Sarmiento-Klapper, Z. Tarzimoghadam, Effect of Microstructural Particularities on the Corrosion Restistance of Nickel Alloy UNS N07718 – What really makes the Difference, presented in Corrosion 2017, New Orleans (LA), 26-30 March, **2017**, paper No. 9068	yes
H. Sarmiento Klapper, J. Klöwer, O. Gosheva, Hydrogen embrittlement – The game changing factor on the applicability of Nickel based alloys in oilfield technology, The Royal Society Scientific Disscussion Meeting, **2017**	yes
O. Gosheva, G. Andersohn, M. Oechsner, Comparative study of the testing approaches for environmental hydrogen embrittlement susceptibility on high strength fasteners, *Materials Testing*, 60, **2018**, 251-256	yes
J. Klöwer, O. Gosheva, H. S. Klapper, Z. Tarzimoghadam, Effect of heat treatment and microstructural particularities on the corrosion resistance of nickel alloy 718, presented in SteelyHydrogen2018, 29-31 May, **2018**	yes